THERMODYNAMIC BASED MODELING FOR NONLINEAR CONTROL OF COMBUSTION PHASING IN HCCI ENGINES

by

JOSHUA BRADLEY BETTIS

A THESIS

Presented to the Faculty of the Graduate School of the

MISSOURI UNIVERSITY OF SCIENCE AND TECHNOLOGY

In Partial Fulfillment of the Requirements for the Degree

MASTER OF SCIENCE IN MECHANICAL ENGINEERING

2010

Approved by

James A. Drallmeier, Advisor
Robert G. Landers
Jagannathan Sarangapani

ABSTRACT

Low temperature combustion modes, such as Homogeneous Charge Compression Ignition (HCCI), represent a promising means to increase the efficiency and significantly reduce the emissions of internal combustion engines. Implementation and control are difficult, however, due to the lack of an external combustion trigger. This thesis outlines a nonlinear control-oriented model of a single cylinder HCCI engine, which is physically based on a five state thermodynamic cycle. This model is aimed at capturing the behavior of an engine which utilizes fully vaporized gasoline-type fuels, exhaust gas recirculation and intake air heating in order to achieve HCCI operation. The onset of combustion, which is vital for control, is modeled using an Arrhenius Reaction Rate expression which relates the combustion timing to both charge dilution and temperature. To account for a finite HCCI combustion event, the point of constant volume combustion is shifted from SOC to a point of *high* energy release based on experimental heat release data. The model is validated against experimental data from a single cylinder CI engine operating under HCCI conditions at two different fueling rates. Parameters relevant to control such as combustion timing agree very well with the experiment at both operating conditions. The extension of the model to other fuels is also investigated via the Octane Index (OI) of several different gasoline-type fuels. Since this nonlinear model is developed from a controls perspective, both the output and state update equations are formulated such that they are functions of only the control inputs and state variables, therefore making them directly applicable to state space methods for control. The result is a discrete-time nonlinear control model which provides a platform for developing and validating various nonlinear control strategies.

ACKNOWLEDGEMENTS

First and foremost, I would like to thank my advisor, Dr. James Drallmeier, for all of his support. Without his encouragement, good teaching, sound advice and direction along the way, this thesis would not have been possible. I am also indebted to the rest of my graduate committee, Dr. Jagannathan Sarangpani and Dr. Robert Landers, for all of their guidance and support. I would also like to extend a special thanks to the National Science Foundation, whose financial support enabled this research to become a reality.

I also owe a great deal to many role models and friends that I met along the way: Jeff Massey, a PhD student at MS&T, who gathered the experimental HCCI engine data and whose insight into engines was invaluable during my graduate studies; Bruce Bunting of Oak Ridge National Laboratories, who allowed data collection from the Hatz research engine; Dr. Jeff Thomas, who provided me the opportunity to work as a graduate teaching assistant; Dave Barnard, my best friend as an undergraduate and who taught me how to appreciate a good rear-engine car; Dr. John Singler, who taught me the finer points of MatLab; and my colleagues in the engines lab, Cory Huck, Avinash Singh and Shawn Wildhaber, who provided a fun working environment.

Lastly, and most importantly, I would like to thank my family, especially my parents, Brad and Shirley Bettis. They have provided love and support throughout my entire life, and without them, nothing I have accomplished would have been possible.

TABLE OF CONTENTS

Page

APPENDICES

LIST OF ILLUSTRATIONS

Figure Page

Figure Page

LIST OF TABLES

NOMENCLATURE

Symbol	Description
A	Pre-exponential factor
a	Fuel reaction order
aTDC	After top dead center
b	Oxidizer reaction order
bTDC	Before top dead center
c_1	Averaged specific heats for fresh reactants
c_2	Averaged specific heat for re-inducted products
c_3	Chemical energy available from combustion
c_{egr}	Averaged specific heat for external EGR
CI	Compression ignition
E_a	Activation energy
EVC	Exhaust valve closing
EVO	Exhaust valve opening
F_{des}	Arrhenius rate threshold
HCCI	Homogeneous charge compression ignition
IVC	Intake valve closing
IVO	Intake valve opening
LHV	Lower heating value of fuel
MON	Motored octane number
$N_{2,k}$	Moles before combustion for cycle k
$N_{3,k}$	Moles after combustion for cycle k
OI	Octane index
$P_{i,k}$	In-cylinder pressure at state *i* for cycle k (*i* = 1-5)
P_{atm}	Atmospheric pressure
RON	Research octane number
SI	Spark ignition
SOC	Start of combustion

TDC	Top dead center
T_{egr}	Temperature of the external EGR
$T_{in,k}$	Intake temperature for cycle k
$T_{i,k}$	In-cylinder temperature at state *i* for cycle k (*i* = 1-5)
T_{ref}	Reference temperature corresponding to heat of formation
R_u	Universal gas constant
UTG96	Unleaded test gasoline with 96 RON
$V_{i,k}$	Cylinder volume at state *i* for cycle k (*i* = 1-4)
$V_{23,k}$	Cylinder volume at combustion for cycle k
V_{TDC}	Cylinder volume at top dead center
$\Delta\theta$	Crank angle between SOC and θ_{23}
θ_{IVC}	Crank angle at intake valve closing
θ_{offset}	Crank angle offset between original and simplified Arrhenius expressions
$\theta_{23,k}$	Crank angle where combustion occurs for cycle k
$\alpha_{i,k}$	Residual mole fraction for cycle k
$\alpha_{e,k}$	External EGR mole fraction for cycle k
β	Percentage of chemical energy lost to heat transfer during combustion
γ	Specific heat ratio
ω	Engine speed
ϕ	Equivalence ratio
ξ	Percentage change in temperature of trapped residual during induction

1. INTRODUCTION

1.1 HOMOGENEOUS CHARGE COMPRESSION IGNITION

Homogeneous Charge Compression Ignition (HCCI) engines have the potential to represent the next generation of technology with respect to internal combustion (IC) engines due to increased thermal efficiency, as well as ultra low NO_x and particulate matter (PM) emissions [1,2,3]. HCCI combustion is realized through the compression auto-ignition of a homogeneous fuel/air mixture which results in a nearly instantaneous ignition event with no discernable flame front [1], thus making it a “hybrid” between conventional spark (SI) and diesel (CI) ignition strategies. HCCI is therefore able to simultaneously achieve the high thermal efficiency of a diesel engine along with near zero NO_x and PM emissions [1]. In spite of these benefits, implementation is difficult due to the lack of an external combustion trigger such as a spark or the injection of fuel. Many different methods have been proposed for achieving HCCI, some of which utilize exhaust gas recirculation (EGR) in order to increase the sensible energy of the inducted mixture in a process called residual affected HCCI. One such residual affected strategy is to delay the closing of the exhaust valve in order to “re-induct” some of the exhaust from the previous cycle [4]. Another residual affected strategy utilizes an early closing of the exhaust valve, which acts to trap some of the exhaust in the cylinder and carry it through to the next cycle [1]. Another method for achieving HCCI utilizes variable boost pressure in order to effectively increase the energy of the inducted charge [3]. The inducted air can also be directly pre-heated upstream of the cylinder, in order to increase its energy [1].

1.2 CYCLIC COMMUNICATION

Since HCCI combustion is dependent upon chemical kinetics rather than an external trigger, there will therefore be some inherent cyclic coupling present due to the carryover of exhaust gas from one cycle to the next [1]. When HCCI is achieved by means of trapping or re-inducting residual gases from the previous cycle via residual affected strategies, successive engine cycles are therefore coupled through the residual temperature. Since the inducted reactants are heated by the retained residual gases, the exhaust temperature from the previous cycle therefore has a direct effect on the kinetics-dominated combustion phasing event of the subsequent cycle. If a large amount of hot residual is carried over, it will serve to heat up the reactant charge which will then result in a more advanced (earlier) combustion phasing.

While the exhaust temperature indeed plays a significant role in cycle to cycle coupling, the heat transfer, which serves to directly affect the temperature, also plays a crucial role. The temperatures experienced during an HCCI engine cycle are somewhat determined by the amount of heat that is transferred, or lost, to the surroundings. The higher the heat transfer, the lower the in-cylinder temperatures, and vice versa. In addition, there is some supplementary heat transfer associated with the mixing process involving the reactant charge and the re-inducted exhaust gases. Similar to the in-cylinder case, the amount of heat transfer during this process will again directly affect the final temperature of the reactant mixture. In general, the heat transfer, both in-cylinder and during the induction stroke, will have a direct impact on the temperature, which then has a significant impact on the combustion phasing.

In addition to the heat transfer effects, there is also a slight amount of cyclic communication which can be introduced through the charge composition. This occurs when the combustion event approaches the misfire limit, which is defined by large amounts of cyclic variation [5]. In this region, combustion becomes incomplete which then results in numerous incomplete products of combustion such as CO, H_2, etc. These extraneous products are then carried over to the next cycle via the residual gases, and serve to impact the combustion timing slightly through both heat capacity and chemical kinetic effects. These effects are typically overpowered by the temperature of the residual, however, due to its dominance of chemical kinetics [1]. Due to their dominance on chemical kinetics, these heat transfer and temperature effects must therefore be captured in the model in order to accurately predict the combustion timing on a cyclic basis.

1.3 HCCI MODELING

Despite the benefits of HCCI, implementation is difficult due to significant challenges in controlling the combustion event. In typical SI and CI engines, combustion is initiated via a spark and the injection of fuel, respectively. In HCCI engines, however, combustion is solely dependent upon chemical kinetics, which rely heavily on mixture properties such as reactant concentrations and mixture temperature [2,3]. HCCI engines therefore lack an external combustion trigger, making control more challenging. Therefore, in order to achieve and maintain HCCI operation, closed loop control strategies must be employed. In order to accomplish this, however, a model of the HCCI process must first be developed. Numerous modeling techniques have been employed to accomplish this, each with differing levels of complexity. The models developed vary widely from simple zero-dimensional models [6,7], to quasi-dimensional models with detailed chemical kinetics [8,9], to one-dimensional models with single zone detailed chemical kinetics [10,11], to multi-dimensional CFD models with multi-zone kinetics [12]. While CFD-based models provide accuracy, model-based controllers require the model to be as simplistic as possible while still capturing the key dynamics of the process. A model of this nature was developed in [13], which captured the behavior of a propane fueled HCCI engine with variable valve timing. While this model is relatively simple, it is only applicable to residual affected HCCI strategies with complex valve actuation systems. In order to achieve effective control, this model developed in [13] employed simplified expressions that ultimately allowed for linearization. The focus of the work presented in this paper is the development of a nonlinear model of the HCCI process, which is based on a five state ideal thermodynamic cycle and is useful for nonlinear controller development. The model presented here captures the behavior of a gasoline-type fueled engine which utilizes pre-heated intake air along with external EGR in order to achieve HCCI operation. Since the model focuses on gasoline-type fuels, the phenomenon of low temperature heat release, which is typically associated with diesel-type fuels, therefore does not need to be considered. This nonlinear model, which employs fewer simplifications than the linearized model in [13], is more representative of the actual HCCI process and will ultimately allow for nonlinear optimal control over a wider range of operating conditions. As HCCI combustion is very sensitive to mixture temperature and reactant concentrations [2], the amount of trapped residual (exhaust gases which are retained in the cylinder) from the previous cycle will therefore impact the next cycle. In order to capture these cycle to cycle dynamics, a residual mass fraction expression is abstracted from [14] for use in the model. Intake air temperature and external EGR rate were chosen as inputs to the model due to their direct influence on mixture temperature and dilution. Combustion timing is calculated using a simplified Arrhenius reaction rate expression, which is initialized using start of combustion data from a single cylinder CI engine operating in HCCI mode. In order to create a discrete-time control model, each cycle in the HCCI process is divided into 5 discrete thermodynamic states. The result is a discrete-time nonlinear model which can be used as a platform for controller development. This nonlinear control model is validated against experimental HCCI engine data from a single cylinder CI engine running on a 96 RON Unleaded Test Gasoline (UTG96), and is able to accurately track, among other engine output parameters, the start of combustion.

2. CONTROL MODEL DEVELOPMENT

2.1 THERMODYNAMIC BASED MODELING

2.1.1 Modeling Approach. An HCCI engine cycle utilizing intake air heating and external EGR is very similar to that of an SI engine, with the exception being the lack of a spark to initiate combustion. Prior to the induction stroke, fuel and external EGR are injected into a pre-heated stream of fresh intake air to form the reactant charge. The intake valve then opens in order to draw this mixture into the cylinder, which then mixes with the trapped residual from the previous cycle to form a homogeneous mixture at intake valve closing, somewhere around bottom dead center. Once the intake valve closes, the upward stroke of the piston acts to compress this newly formed mixture. This compression process results in a spontaneous auto-ignition of the mixture, typically occurring somewhere around top dead center, which is nearly instantaneous and shows no discernable flame front [1]. This combustion process initiates the expansion stroke, during which the piston is forced downwards and useful work is extracted via the crankshaft. The exhaust valve is then opened, typically slightly before bottom dead center, to allow for the spent exhaust gases to be pushed out of the cylinder during the upward stroke of the piston, i.e. the exhaust stroke. Due to engine geometry and valve timings, a fraction of these exhaust gases, known as the residual fraction, will remain trapped in the cylinder and carried through to the next cycle. Somewhere around top dead center, the intake valve is opened followed closely by the closing of the exhaust valve, which allows for the induction of another fresh reactant charge.

The model being discussed is based on a Hatz 1D50Z CI engine operating in HCCI mode, the experimental setup for which is presented in previous work done by Massey et al. [15]. The geometry and valve timings of this engine are fundamental to the aforementioned engine cycle, in that they determine both the behavior and the duration of the various processes throughout the cycle. These critical engine parameters, along with other engine operating conditions for the single cylinder CI engine being modeled, can be seen in Table 2.1.

Table 2.1: Engine Operating Conditions

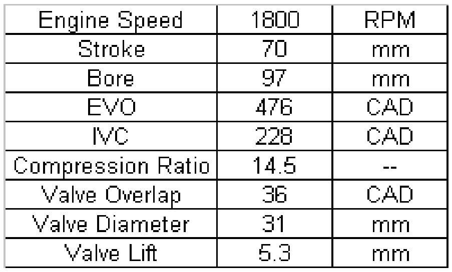

Engine Speed	1800	RPM
Stroke	70	mm
Bore	97	mm
EVO	476	CAD
IVC	228	CAD
Compression Ratio	14.5	--
Valve Overlap	36	CAD
Valve Diameter	31	mm
Valve Lift	5.3	mm

Based on the above description of the HCCI cycle, this continuous process can be modeled using an ideal thermodynamic cycle, and therefore divided up into 5 distinct states. Several assumptions must be made in order to accomplish this, all of which have some thermodynamic basis. The induction process is assumed to be adiabatic, and at a constant pressure. This is a reasonable assumption due to the engine being naturally aspirated along with the small time scale of the induction stroke. The compression stroke is assumed to be isentropic, which is typical of most thermodynamic cycles. The auto-ignition process is assumed to take place at a constant volume due to HCCI combustion occurring almost instantaneously. The expansion and blow down processes are both assumed to be isentropic, which is again a common thermodynamic assumption. Similar to induction, the exhaust process is also assumed to be adiabatic, and to take place at a constant pressure.

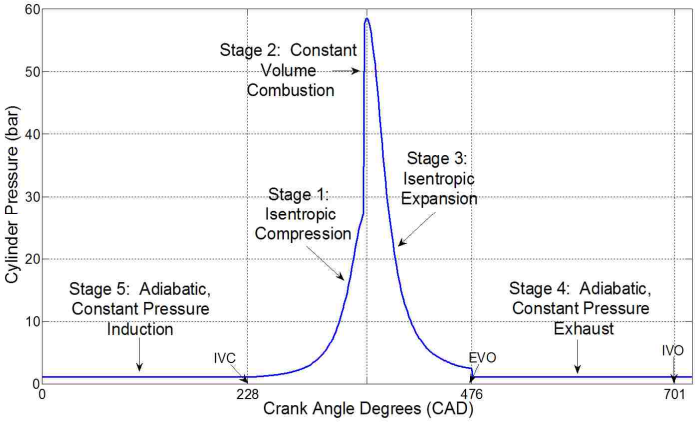

Figure 2.1: HCCI cycle modeled as five distinct thermodynamic states

Figure 2.1 shows these distinct states within the HCCI cycle, along with the evolution of the cylinder pressure throughout an entire engine cycle, for the engine being modeled. It is important to note that the engine cycle is defined to begin with compression rather than induction. This is done to accommodate for the fact that the model will ultimately be used for nonlinear control, which requires the future evolution of the system to be entirely determined by its present state [16]. Since the model inputs are introduced during the induction stroke, it will therefore be possible to define the current cycle based solely on information from the previous cycle. With the engine cycle now assumed to be a discrete process, we now have the basis to create a discrete-time control based model.

2.1.2 Inputs, Outputs and State Variables. Since the model being developed will ultimately be used to synthesize a nonlinear controller, it must therefore be constructed from a controls perspective. The model presented therefore includes three input variables, both of which directly affect the combustion process. These inputs are defined to be the following:

- the pre-heated intake temperature, $T_{in,k}$
- the fraction of external EGR, $\alpha_{e,k}$
- the mass flow rate of fuel, gpm_k

These inputs, with k representing the k^{th} engine cycle, were chosen due to their physical significance within the HCCI process. Since start of combustion is sensitive to changes in reactant concentrations and temperature, these inputs therefore directly affect combustion timing through temperature and dilution effects, respectively. The intake temperature is controlled using a resistance heater placed in the intake stream, while the external EGR and fueling rate are controlled using individual solenoids. In addition to inputs, the model must also include certain output variables which can be used for feedback to monitor and control the system. The first output chosen for this model was the combustion phasing. Due to the desire for an actual engine to operate at some optimal combustion timing, the model must therefore include an output variable which represents this phenomenon in order to have the ability to control it. Similar to operating at a desired combustion phasing, engines are also required to produce a desired amount of work. In light of this, the second output was chosen to be the peak pressure during each cycle, which then gives a basis for the work output from each engine cycle. This allows the control model to formulate the work being produced, and then optimize it to some desired value. In order to ensure that the engine remained within an acceptable operating range, another output was chosen to be the peak pressure rise rate during each cycle. Since the operating range is typically limited by the pressure rise rate [17], it must therefore be included as an output in order to properly control the engine. In addition, an efficiency term was also included as an output. This efficiency term monitored the work output from the engine based on the amount of fuel energy input, and therefore gave an indication of how "efficient" the engine was operating. These outputs are summarized below:

- crank angle where combustion occurs, $\theta_{23,k}$
- peak pressure, $P_{3,k}$
- pressure rise rate, PRR_k
- work output, $W_{g,k}$
- efficiency, η_k

where k again denotes the k^{th} engine cycle.

In order to utilize state-space control methodologies, the model must also define certain "states" which completely describe the dynamics of the system with respect to the output variables being controlled. From a modeling perspective, it is preferable if these "state" variables have some physical meaning so as to gain insight into their influence on the various outputs from the system. With control of combustion phasing central to the control effort, these "states" of the system should therefore be physically related to both the reactant concentrations and charge temperature within each cycle, which are the parameters central to combustion. One such parameter within the model is the residual mass fraction, which serves to pass information from one cycle to the next. This residual, or internal EGR, consists of burned gases at the exhaust temperature of the previous cycle, and acts to simultaneously increase the temperature and dilute the fresh reactant charge entering the cylinder. Another parameter related to combustion timing is the temperature in the cylinder at IVC. Intake valve closing is one of the discrete states within the model, and the corresponding temperature indicates the charge temperature at the start of compression. Another parameter of importance is the actual combustion phasing from the previous cycle. As timing is varied, the exhaust temperature and amount of trapped residual will also vary, thus having an impact on the phasing during the next cycle through the parameters mentioned previously. All of these state variables were chosen due to their apparent physical significance to the combustion process, and are summarized below:

- the amount of trapped residual, $\alpha_{i,k}$
- the initial mixture temperature at IVC, $T_{1,k}$
- the crank angle where peak pressure occurs, $\theta_{23,k}$

With the inputs, outputs and state variables of the system defined, the various stages of the HCCI engine cycle can now be investigated in order to relate each thermodynamic state back to the inputs and state variables of the system.

2.2 EQUATION DERIVATION

2.2.1 Adiabatic Induction at Atmospheric Pressure – Instantaneous Mixing. Prior to the start of the cycle, fresh reactants must first be inducted into the cylinder during the induction stroke. This process is assumed to be adiabatic and to take place at atmospheric pressure. Pre-heated intake air, fuel and external EGR (α_e) are all inducted into the cylinder when the intake valve opens, and are assumed to instantaneously mix with the trapped residual in the cylinder at the instant of IVC. In order to determine the thermodynamic state of the mixture at intake valve closing, the chemistry of the mixture must first be investigated. Since HCCI engines are capable of running on many different types of fuels, this chemistry will vary depending on the type of fuel being used. The current model focuses on gasoline-type fuels, and is later validated using data from an engine running on UTG96, which has a C/H ratio equal to 7.2/15.8. Although any gasoline-type fuel can be used, one with a C/H ratio equal to 7/16 is chosen as the fuel in this analysis due to its similarity to the aforementioned validation fuel. As a check, isooctane (C/H=8/18) was also investigated and it was determined that the model produced very similar results for both C/H ratios. In order to determine the state of the mixture, combustion of this gasoline-type fuel (C/H = 7/16) with atmospheric air is performed under stoichiometric conditions.

$$C_7H_{16} + 11(O_2 + 3.76N_2) \rightarrow 7CO_2 + 8H_2O + 41.36N_2 \tag{2.1}$$

Now assuming lean combustion (typical of HCCI engines [1]) with stoichiometric air and both internal and external EGR, the inducted reactant charge becomes:

$$\begin{aligned}&\phi C_7H_{16}+11(O_2+3.76N_2)+\alpha_e(\phi+52.36)N_2+\\&\alpha_i(7\phi CO_2+8\phi H_2O+41.36N_2+11(1-\phi)O_2)\end{aligned} \tag{2.2}$$

where ϕ is the equivalence ratio, defined as the ratio of moles of fuel to the stoichiometric amount, α_i is the fraction of internal EGR and α_e is the fraction of external EGR added. This external EGR fraction is defined as the molar ratio of external EGR to reactants, and is initially modeled using the inert gas N_2. With the chemistry of the intake charge now known, the First Law of Thermodynamics can be applied to the mixing process in order to determine the state of the mixture at IVC, where the reactants are assumed to instantaneously mix. Assuming the air and external EGR enter at constant temperatures of T_{in} and T_{egr}, respectively, the resulting expression for the First Law applied to the kth engine cycle becomes:

$$\sum_{\text{products}} N_{i,k}\bar{h}_{i,k}(T_{prod,k})+\sum_{\text{reactants}} N_{i,k}\bar{h}_{i,k}(T_{in,k})+\sum_{\text{EGR}} N_{i,k}\bar{h}_{i,k}(T_{egr,k})=\sum_{\text{mix}} N_{i,k}\bar{h}_{i,k}(T_{1,k}) \tag{2.3}$$

where $N_{i,k}$ is the number of moles of species i, $\bar{h}_{i,k}$ is the molar enthalpy of species i, $T_{prod,k}$ is the temperature of the trapped residual and $T_{1,k}$ is the temperature of the reactants and products after full mixing. Assuming constant specific heats, the molar enthalpy becomes:

$$\bar{h}_i(T)=\Delta\bar{h}_{f,i}+\bar{c}_{p,i}(T-T_{ref}) \tag{2.4}$$

where $\Delta\bar{h}_{f,i}$ is the molar heat of formation of species i and T_{ref} is the reference temperature corresponding to the heat of formation. Applying Equation 2.3 to Equation 2.2 yields the following in-cylinder mixture temperature at intake valve closing (IVC):

$$T_{1,k} = \frac{c_{1,k-1}T_{in,k-1} + c_{2,k-1}\alpha_{i,k}T_{prod,k} + c_{egr,k-1}\alpha_{e,k-1}T_{egr,k}}{c_{1,k-1} + c_{2,k-1}\alpha_{i,k} + c_{egr,k-1}\alpha_{e,k}} \tag{2.5}$$

where

$$c_{1,k} = \phi_k \bar{c}_{p\,C_7H_{16}} + 11\bar{c}_{p\,O_2} + 41.36\,\bar{c}_{p\,N_2} \tag{2.6}$$

$$c_{2,k} = 7\phi_{k-1}\bar{c}_{p\,CO_2} + 8\phi_{k-1}\bar{c}_{p\,H_2O} + 41.36\,\bar{c}_{p\,N_2} + 11\left(1-\phi_{k-1}\right)\bar{c}_{pO_2} \tag{2.7}$$

$$c_{egr,k} = \left(\phi_k + 52.36\right)\bar{c}_{p\,N_2} \tag{2.8}$$

represent averaged specific heats for the reactants, trapped residual and external EGR, respectively. In Equation 2.5, T_{prod} is the temperature of the residual, which can be directly related to the exhaust temperature of the previous cycle via the following linear relationship

$$T_{prod,k} = \xi T_{5,k-1} \tag{2.9}$$

where ξ represents heat loss during the valve overlap period. This parameter was determined by synchronizing the model temperatures at IVC with those extracted from the experimental data. Plugging Equation 2.9 into Equation 2.5 results in the following expression for the mixture temperature at intake valve closing:

$$T_{1,k} = \frac{c_1 T_{in,k-1} + c_2\alpha_{i,k}\xi T_{5,k-1} + c_{egr}\alpha_{e,k-1}T_{egr,k}}{c_1 + c_2\alpha_{i,k} + c_{egr}\alpha_{e,k-1}} \tag{2.10}$$

2.2.2 Isentropic Compression. The engine cycle is defined to start at the beginning of the compression process at IVC. This compression of the freshly inducted reactant charge made up of fuel, air and EGR is assumed to be isentropic, which implies the following relationships:

$$T_{2,k} = \left(\frac{V_1}{V_{23,k}} \right)^{\gamma - 1} T_{1,k} \tag{2.11}$$

$$P_{2,k} = \left(\frac{V_1}{V_{23,k}} \right)^{\gamma} P_{1,k} \tag{2.12}$$

State 2 is defined to be at the end of compression just before the onset of combustion. In these relations, V_1, T_1 and P_1 represent the volume, temperature and pressure at intake valve closing, respectively. The parameter γ represents the ratio of specific heats, and is set to 1.3 in this analysis, which is a reasonable approximation for the working fluid. Also, V_{23} signifies the volume at which the constant volume combustion event occurs. This volume can be determined using the simple slider-crank relations from [18], where $\theta_{23,k}$ represents the crank angle at which the constant volume combustion occurs.

$$V_{23,k} = V_c \left[1 + 0.5 (r_c - 1) \left(R + 1 - \cos(\theta_{23,k}) - \sqrt{R^2 - \sin^2(\theta_{23,k})} \right) \right] \tag{2.13}$$

2.2.3 Constant Volume Combustion. The auto-ignition process in HCCI engines occurs almost instantaneously throughout the cylinder, and is therefore assumed to take place at a constant volume. It is also assumed that all heat transfer occurs during the combustion event. A model which utilizes an Integrated Arrhenius Rate to predict the location of this combustion event is discussed later. Using the chemistry of the lean intake charge in Equation 2.2, along with the assumption of complete combustion, the overall combustion reaction becomes:

$$\begin{gathered}\phi_k C_7 H_{16} + 11\left(\alpha_{i,k+1}\left(1-\phi_{k-1}\right)+1\right)O_2 + \left(41.36\left(1+\alpha_{i,k+1}\right)+\alpha_{e,k}\left(\phi_k + 52.36\right)\right)N_2 + \\ 7\phi_{k-1}\alpha_{i,k+1}CO_2 + 8\phi_{k-1}\alpha_{i,k+1}H_2O \rightarrow \\ 7\left(\phi_k + \phi_{k-1}\alpha_{i,k+1}\right)CO_2 + 8\left(\phi_k + \phi_{k-1}\alpha_{i,k+1}\right)H_2O + \left(41.36\left(1+\alpha_{i,k+1}\right)+\alpha_{e,k}\left(\phi_k + 52.36\right)\right)N_2 + \\ 11\left(1+\alpha_{i,k+1} - \phi_k - \phi_{k-1}\alpha_{i,k+1}\right)O_2 \end{gathered} \tag{2.14}$$

In order to determine the thermodynamic state of the system after combustion, the First Law is again applied. Since both the intake and exhaust valves are closed during the compression stroke, the cylinder is therefore modeled as a closed system and the First Law takes the form

$$\Delta U = Q - W \tag{2.15}$$

Since combustion occurs instantaneously, the cylinder volume does not change and therefore no work is produced. The heat transfer term in Equation 2.15 can be approximated to be a certain percentage of the chemical energy available before combustion. Applying these assumptions to the expression in Equation 2.15, the First Law now becomes:

$$U_{2,k} = U_{3,k} + LHV_{C7H16} N_{C7H16,k} \beta \tag{2.16}$$

where LHV_{C7H16} and N_{C7H16} represent the lower heating value and moles of fuel, respectively. In Equation 2.16, the parameter β represents the percentage of chemical energy that is lost to heat transfer during combustion. This parameter was set to 0.1, which represents the approximate energy loss due to heat transfer as given in [18]. Utilizing the definition of internal energy in [18], along with the ideal gas law, the expression in Equation 2.16 can be rewritten in terms of enthalpy

$$\sum\nolimits_2 N_{i,k}\overline{h_{i,k}} - N_{i,k}R_uT_{2,k} = \sum\nolimits_3 N_{i,k}\overline{h_{i,k}} - N_{i,k}R_uT_{3,k} + LHV_{C7H16}N_{C7H16}\beta \tag{2.17}$$

Substitution of the combustion reaction parameters from Equation 2.14 into the expression in Equation 2.17 yields the following expression for the temperature inside the cylinder immediately after combustion, defined as State 3.

$$T_{3,k} = \frac{c_{3,k-1} + \left(c_{1,k-1} + c_{2,k-1}\alpha_{i,k} + c_{egr,k-1}\alpha_{e,k-1} - R_uN_{2,k}\right)T_{2,k} - \left(c_{1,k-1} - c_{4,k-1}\right)T_{ref}}{c_{2,k-1}\alpha_{i,k} + c_{egr,k-1}\alpha_{e,k-1} + c_{4,k-1} - R_uN_{3,k}} \tag{2.18}$$

where

$$\begin{aligned}
c_{3,k} &= \phi_{k-1}\, LHV_{C7H16}\left(1-\beta\right) \\
c_{4,k} &= 7\phi_{k-1}\bar{c}_{p\,CO_2} + 8\phi_{k-1}\bar{c}_{pH_2O} + 41.36\bar{c}_{p\,N_2} + 11\left(1-\phi_{k-1}\right)\bar{c}_{pO_2} \\
N_{2,k} &= \alpha_{i,k}\left(4\phi_{k-2} + 52.36\right) + \alpha_{e,k-1}\left(\phi_{k-1} + 52.36\right) + \left(\phi_{k-1} + 52.36\right) \\
N_{3,k} &= 4\left(\phi_{k-1} + \phi_{k-1}\alpha_{i,k}\right) + 52.36\left(1 + \alpha_{i,k}\right) + \alpha_{e,k-1}\left(\phi_{k-1} + 52.36\right)
\end{aligned} \tag{2.19}$$

The parameters N_2 and N_3 here represent the number of moles in the cylinder before and after combustion, respectively. In addition, T_{ref} represents the reference temperature of 298 K corresponding to the heat of formation.

Applying the ideal gas law before and after combustion, and recalling that combustion occurs at a constant volume, results in the following expression.

$$P_{3,k} = \frac{N_{3,k}}{N_{2,k}}P_{2,k}\frac{T_{3,k}}{T_{2,k}} \tag{2.20}$$

In an effort to define P_3 solely in terms of temperature, the expression in Equation 2.18 can be rearranged to yield:

$$T_{2,k} = \frac{\left(c_{2,k-1}\alpha_{i,k} + c_{egr,k-1}\alpha_{e,k-1} + c_{4,k-1} - R_u N_{3,k}\right)T_{3,k} + \left(c_{1,k-1} - c_{4,k-1}\right)T_{ref} - c_{3,k-1}}{c_{1,k-1} + c_{2,k-1}\alpha_{i,k} + c_{egr,k-1}\alpha_{e,k-1} - R_u N_{2,k}} \qquad (2.21)$$

Substituting Equations 2.12 and 2.21 into Equation 2.20 results in an expression for the pressure immediately after combustion which represents the peak pressure seen during the engine cycle.

$$P_{3,k} = \frac{N_{3,k}}{N_{2,k}}\left(\frac{V_1}{V_{23,k}}\right)^{\gamma} \frac{c_{1,k-1} + c_{2,k-1}\alpha_{i,k} + c_{egr,k-1}\alpha_{e,k-1} - R_u N_{2,k}}{\left(c_{2,k-1}\alpha_{i,k} + c_{egr,k-1}\alpha_{e,k-1} + c_{4,k-1} - R_u N_{3,k}\right)T_{3,k} + \left(c_{1,k-1} - c_{4,k-1}\right)T_{ref} - c_{3,k-1}} P_{atm} T_{3,k} \qquad (2.22)$$

2.2.4 Isentropic Expansion. Following combustion, the piston travels downwards during the expansion stroke, which produces useful work from the engine. This expansion process, which takes place until the opening of the exhaust valve, is assumed to be isentropic, which implies the following relationships:

$$T_{4,k} = \left(\frac{V_{23,k}}{V_4}\right)^{\gamma-1} T_{3,k} \qquad (2.23)$$

$$P_{4,k} = \left(\frac{V_{23,k}}{V_4}\right)^{\gamma} P_{3,k} \qquad (2.24)$$

Here, State 4 is defined as the end of the expansion stroke at the instant of exhaust valve opening. In these relations, T_3 and P_3 represent the temperature and pressure immediately after combustion, respectively. The parameters V_4 and V_{23} represent the cylinder volumes at EVO and at which the constant volume combustion event occurs, respectively. Both of these cylinder volumes can be calculated using the simple slider-crank relation in Equation 2.13 along with the appropriate crank angle.

2.2.5 Isentropic Blowdown to Constant Pressure Exhaust. The exhaust stroke, which is defined from exhaust valve opening to intake valve opening, is also assumed to take place at constant pressure. An instantaneous blowdown to atmospheric pressure is assumed to occur at EVO, which then allows this adiabatic exhaust process to take place at atmospheric pressure. Under these assumptions, a relation for the temperature at State 5 (intake valve opening) can be written.

$$T_{5,k} = \left(\frac{P_{atm}}{P_{4,k}} \right)^{\gamma-1/\gamma} T_{4,k} \tag{2.25}$$

2.3 RESIDUAL GAS FRACTION MODEL

The amount of residual gas in HCCI engines has a profound effect on emissions, combustion stability and volumetric efficiency. Residual gas affects the combustion process in HCCI engines through its influence on both the dilution and temperature of the overall charge mixture. This becomes particularly important when dealing with HCCI engines. Since HCCI combustion depends entirely on chemical kinetics in order to occur, both the dilution and the temperature of the charge mixture will directly affect the combustion phasing of the engine. According to chemical kinetics models, HCCI combustion is governed by two main parameters: the concentrations of fuel and oxygen, and the temperature. This means that changing the concentration and/or the temperature of the intake charge will cause the combustion phasing to change. The fact that the residual gas fraction directly affects both the reactant concentrations and the temperature, makes it an important parameter when trying to model combustion timing in an HCCI engine. Therefore, a practical and accurate model for predicting the residual gas fraction x_r is needed in order to accurately predict the combustion timing.

The predictive model used was taken from [14], which was based on the widely accepted model developed in [19]. This model predicted the overall residual gas fraction as a combination of two components: the contribution of back-flow from the exhaust to the cylinder during valve overlap, and the trapped gas in the cylinder at exhaust valve closing. The amount of residual trapped in the cylinder at EVC can be estimated fairly accurately with knowledge of the compression ratio. The flow processes during the valve overlap period, however, are very complex and are therefore difficult to model correctly. For most engine speeds, the cylinder contents equilibrate with the exhaust system during the exhaust stroke and are roughly at atmospheric pressure. The intake port, on the other hand, is generally below atmospheric pressure, which results in a net flow of burned gas into the cylinder from the exhaust manifold [19]. This back-flow contributes significantly to the residual gas fraction for each engine cycle. The parameter often used to describe this back-flow is the valve overlap factor (OF). An empirical expression for OF is given in [19] when the valve overlap duration is known, and can be seen in Equation 2.26 below.

$$OF = \frac{1.45}{B}\left(107 + 7.8\Delta\theta_{ov} + \Delta\theta_{ov}^{\ 2}\right)\frac{L_{v,\max}D_v}{B^2} \qquad (2.26)$$

In Equation 2.26, OF is the valve overlap factor in degrees/meter, $\Delta\theta_{ov}$ is the valve overlap in crank angle degrees, B is the engine bore in mm, $L_{v,max}$ is the maximum valve lift in mm, and D_v is the valve inner seat diameter in mm. This expression gives a good estimate of OF for most typical engine geometries.

Once the overlap factor, OF, is known, an expression for the overall residual gas fraction can be determined. The empirical expression from [14] is given below in Equation 2.27.

$$x_r = 0.401\frac{OF}{N}\left[1-\exp\left(-4.78\left(1-\frac{P_i}{P_e}\right)^{0.7}-153.8\left(1-\frac{P_i}{P_e}\right)^{4.5}\right)\right]\frac{P_e}{P_i}\frac{T_i}{T_e}+\frac{1}{r_c}\frac{P_e}{P_i}\frac{T_i}{T_e} \qquad (2.27)$$

In Equation 2.27, x_r is the residual gas fraction, OF is the valve overlap factor in degrees/meter, N is the engine speed in rev/sec, P_e and P_i are the exhaust and intake pressures, respectively, in bar, T_e and T_i are the exhaust and intake temperatures, respectively, in Kelvin, and r_c is the compression ratio. This resulting model relates the residual gas fraction to six independent parameters: engine speed (N), inlet and exhaust pressures (P_i and P_e), the valve overlap factor (OF), inlet temperature (T_i), and the compression ratio (r_c). The first part of the expression gives the contribution from the valve overlap period, while the second part relates to the amount of gas trapped in the cylinder at exhaust valve closing. The sum of these two components gives the total predicted residual.

This model for predicting the residual gas fraction was abstracted from [14]. This model explicitly accounts for the contributions from both the back-flow of exhaust gas into the cylinder during the valve overlap period and the gas trapped in the cylinder at exhaust valve closing. The model correlated well with experiment over a wide range of intake pressures and engine speeds [14], which means that it should provide an accurate prediction of the residual gas fraction. It is important to note that the residual fraction will be a small number for most operating conditions. When no external EGR is implemented on the engine, the residual gas fraction will have a noticeable effect on the combustion phasing due to the fact that it will dilute and increase the temperature of the reactant mixture. On the other hand, if there is some external EGR, then the effect of the residual gas fraction will be minimal. In this case, the amount of EGR will typically be far greater than that of the residual gases, which will result in the external EGR having a dominant effect on both the dilution and temperature of the reactant charge.

2.4 DENSITY AND EGR DISPLACEMENT EFFECTS

When intake temperature is used as an input in order to achieve HCCI, a side effect is that the density of the intake air also changes as the temperature is varied. This allows for different amounts of air to be inducted at different intake temperatures, which will ultimately have a slight effect on the equivalence ratio. Using the ideal gas law, the moles of air inducted per cycle can be represented by:

$$N_A = \frac{P_{in} V_d}{R_u T_{in}} \tag{2.28}$$

This relationship assumes that induction occurs at atmospheric pressure, and therefore allows the moles of air to be calculated based on a given intake temperature. The displacement volume is used in this case due to the clearance volume being occupied by residual from the previous cycle. For a given fueling rate then, the moles of fuel inducted per cycle can be determined by

$$N_F = \frac{2\dot{m}_f}{N \cdot MW_f} \tag{2.29}$$

where $\dot{m}_f$ is given in grams/min. and N is given in RPM. Once the relative amounts of fuel and air are known, the next parameter of interest is the amount of fuel required to achieve stoichiometric conditions within the cylinder. Using the relationship for the stoichiometric F/A ratio, along with the moles of air calculated using Equation 2.28, the stoichiometric moles of fuel are given by

$$N_{Fs} = \frac{N_A MW_a \left({}^{F}\!/_{A} \right)_{stoic}}{MW_f} \tag{2.30}$$

Equations 2.28-2.30 allow the amount of air inducted into the cylinder to vary based on the given intake temperature. This allows the equivalence ratio to vary slightly as temperature is varied, which is what is observed in the experimental data.

When EGR is introduced into the cylinder during induction, it acts to displace some of the fresh reactant charge that would otherwise get inducted into the cylinder. In order to account for this displacement effect, the amount of air inducted into the cylinder must therefore be reduced as the amount of EGR is increased. In order to determine the amount of air displaced by this EGR, the total capacity of the overall cylinder must be determined first. This cylinder capacity can be determined using the ideal gas law along with the total volume of the cylinder.

$$N_T = \frac{P_{in}\left(V_d + V_c\right)}{R_u T_{in}} \tag{2.31}$$

The expression in Equation 2.31 allows the total amount of moles inducted to change as the intake temperature is varied, which is necessary in order to capture the density effects described previously. Due to valve timings and engine geometry, a small portion of this total volume is made up of trapped residual gas that is carried over from the previous cycle. The amount of this residual that is present in the cylinder can be determined using the residual fraction, α_i, along with the expression in Equation 2.31.

$$N_{iEGR} = \alpha_i N_T \tag{2.32}$$

Since we are introducing EGR into the cylinder in this case, another portion of the total cylinder volume will also be occupied by external EGR. In order to determine the number of moles inducted into the cylinder, the mole fraction of external EGR must first be calculated. Using the expression in Equation 2.2

$$X_{EGR} = \frac{\alpha_e(\phi + 59.5)}{(\phi + 59.5)(1 + \alpha_e) + \alpha_i\left(17\phi + 47 + 12.5(1 - \phi)\right)} \tag{2.33}$$

where ϕ and α_e are the equivalence ratio and external EGR fraction which were defined previously. The expression in Equation 2.33 can then be used to calculate the number of moles of EGR inducted into the cylinder.

$$N_{EGR} = X_{EGR} N_T \tag{2.34}$$

Now that the residual and EGR have been accounted for, the remainder of the cylinder volume can be filled with fresh air. In order to capture the displacement effect of the EGR, however, the amount of air inducted must be calculated using partial pressures. Based on the contents of the cylinder, this partial pressure expression becomes

$$P = X_{EGR}P + X_{iEGR}P + X_{A}P \tag{2.35}$$

Plugging Equations 2.31, 2.32 and 2.34 into Equation 2.35 results in a partial pressure expression in terms of moles rather than mole fractions.

$$P_{in} = \frac{N_{EGR}}{N_T}P_{in} + \frac{N_{iEGR}}{N_T}P_{in} + \frac{N_A}{N_T}P_{in} \tag{2.36}$$

Rearranging the expression in Equation 2.36 yields:

$$N_A = N_T - N_{EGR} - N_{iEGR} \tag{2.37}$$

This expression accounts for the displacement effect by allowing the moles of air inducted to vary based on the amount of external EGR being introduced. With the moles of air now known, the moles of fuel required for a stoichiometric mixture can now be calculated using the expression in Equation 2.30. The density and displacement effects present for the case of external EGR have been accounted for in Equations 2.31 and 2.37, respectively, which allow the model to accurately predict the amounts of fuel and air being inducted into the cylinder for each cycle.

2.5 MODELING THE ONSET OF COMBUSTION

Unlike conventional spark and compression ignition engines, HCCI engines have no specific combustion initiator. Instead of being initiated by a spark or the injection of fuel, HCCI ignition depends entirely on the chemical kinetics [1,2,3]. If the reactant concentrations and temperature reach sufficient levels during compression, then an auto-ignition process will occur. Combustion timing is therefore directly linked to the in-cylinder concentrations of reactants, their temperature and their pressure [1,2,3]. Due to this dependence on chemical kinetics, ensuring that combustion occurs with acceptable timing, or even at all, is much more complicated than in the case of either spark or compression ignition engines. Since the combustion timing plays such a vital role in the HCCI process, choosing an appropriate model to represent it is therefore crucial.

Since the goal is to create a control-oriented model, the combustion timing model chosen must predict both the pressure evolution in the cylinder and, more importantly, the combustion timing. The pressure evolution directly correlates to the work output from the engine, while the combustion timing acts to govern this pressure evolution from cycle to cycle. Therefore, if the combustion timing model can accurately predict the ignition timing, then it should also be able to predict the pressure evolution in the cylinder. Since the combustion timing directly controls how the engine will perform, then choosing a combustion timing model that accurately predicts how the timing will change from engine cycle to engine cycle is imperative to ensure the validity of the overall model. Therefore, a great deal of time was spent on choosing an acceptable combustion timing model that would accurately predict the changes in ignition timing as input conditions were varied. A number of different models were considered [20-25] throughout the selection process before narrowing the possible models down to the five most promising. The following sections present these five different models that were investigated for predicting the onset of combustion. These models include a modified knock integral [26], three different ignition delay models [27-29] and an integrated Arrhenius rate model [13]. In each of the five different models, a lean reaction of air and a gasoline-type fuel is considered. The focus is restricted to gasoline-type fuels in order to eliminate the complexities of low temperature heat release that are typically associated with diesel-type fuels. A lean reaction requires that the equivalence ratio, ϕ, be less than one. The stoichiometric (ϕ=1) and rich (ϕ>1) cases need not be investigated due to the fact that HCCI is a purely lean strategy by nature. For the lean case then, with the assumption of complete combustion and no exhaust gas recirculation, the global combustion reaction used in each model is given by:

$$\phi C_7H_{16} + 11O_2 + 41.36N_2 \quad \Rightarrow \quad 7\phi CO_2 + 8\phi H_2O + 41.36N_2 + 11(1-\phi)O_2 \qquad (2.38)$$

In order to verify whether or not the combustion timing models were correctly predicting the ignition timing, the simulation was compared with actual engine data from a Hatz HCCI engine. The geometry and other engine parameters for the Hatz engine can be found in Table 2.2.

Table 2.2: Hatz engine parameters

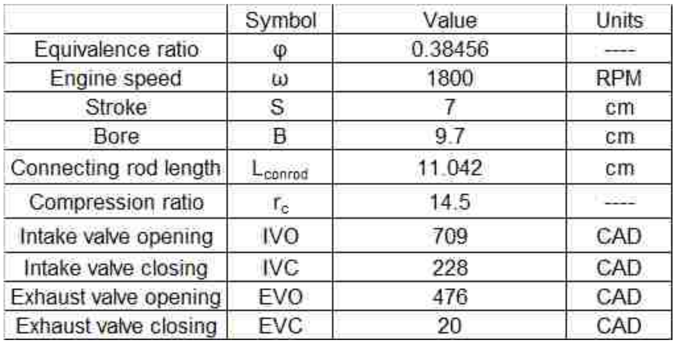

	Symbol	Value	Units
Equivalence ratio	φ	0.38456	----
Engine speed	ω	1800	RPM
Stroke	S	7	cm
Bore	B	9.7	cm
Connecting rod length	L_{conrod}	11.042	cm
Compression ratio	r_c	14.5	----
Intake valve opening	IVO	709	CAD
Intake valve closing	IVC	228	CAD
Exhaust valve opening	EVO	476	CAD
Exhaust valve closing	EVC	20	CAD

In the experiment, the temperature of the incoming air was varied, with the equivalence ratio being held constant, in order to effectively change the ignition timing from cycle to cycle. The same thing could then be done in the model by simply changing the intake temperature. This was done for several different intake temperatures, and the model results were then compared to the experimental results in order to determine which model predicted the onset of combustion the best.

2.5.1 Modified Knock Integral Method. The first of the four combustion timing models investigated was that of a modified knock integral. This was a reasonable model to look at first, due to its similarities to the original knock integral [30]. In order to understand why a modified knock integral method is necessary, the original knock integral must be investigated first. The knock integral method was originally developed in order to investigate the premature ignition of the fuel and air mixture prior to the spark, called knock, in spark ignition engines. Since HCCI combustion depends on the auto-ignition of a fuel and air mixture, the knock integral method would seem to be a very good way to model it. Livengood and Wu [30] developed the first correlation to predict the auto-ignition of a homogeneous fuel and air mixture, which was later called the Knock Integral Method. This method is based upon the ignition delay time of the fuel under consideration, and the resulting empirical relationship is given by:

$$\tau = Ae^{(b/T)P^n} \tag{2.39}$$

where τ is the ignition delay time, T is the mixture temperature as a function of crank angle, P is the mixture pressure as a function of crank angle, and A, b and n are empirical constants that are determined experimentally for each fuel.

Livengood and Wu discovered that there is a functional relationship between the concentrations of the significant species in the reaction and the time it takes to complete the reaction. When time is replaced by crank angle via the engine speed, the ignition correlation for the knock integral becomes:

$$\int_{IVC}^{\theta_{knock}} \frac{1}{\omega\tau} d\theta = \int_{IVC}^{\theta_{knock}} \frac{1}{\omega Ae^{(b/T)P^n}} d\theta = 1 \tag{2.40}$$

where θ_{knock} is the crank angle at which knock occurs and IVC is the crank angle of intake valve closing. The engine speed, denoted as ω, has units of RPM, the pressure has units of KPa and the temperature has units of degrees Kelvin. The integration is started at intake valve closing due to the fact that compression, and therefore any type of appreciable reaction, begins at this point. The value of the integrand continues to increase as the auto-ignition point is reached, which is shown in Figure 2.2 below.

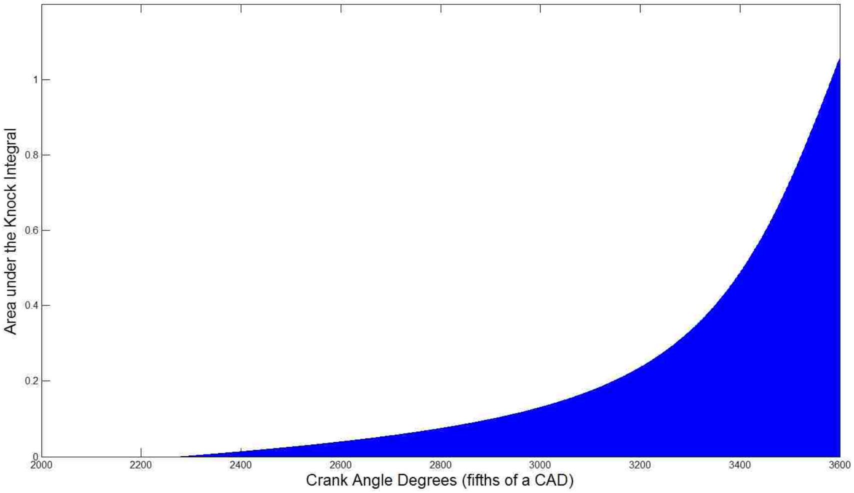

Figure 2.2: Graphical integration of the knock integral from intake valve closing

Once the integral becomes equal to one, the upper limit is said to be the crank angle at which auto-ignition, or knock, occurs. The integral seen in Equation 2.40, then, is ultimately able to predict at what crank angle knock, or auto-ignition will occur. This ability to predict the auto-ignition point of a fuel-air mixture makes the knock integral a very appealing approach to try and predict the start of combustion in HCCI applications. In order to make the transition from spark ignition to HCCI, however, the knock integral must first be modified in order to account for a greater dependence upon chemical kinetics.

The modified knock integral combustion model that was investigated was abstracted from previous work done by [26]. In this model, Swan took the original knock integral and simply added a few terms in order to make it applicable to HCCI combustion. Since HCCI combustion depends so heavily upon chemical kinetics, terms were added to the integral in order to account for things such as fuel and oxygen concentrations, and varying EGR rates. The compression process was considered to be polytropic (PV^{γ}=constant) due to the fact that temperature and pressure as a function of crank angle are usually unknown on an actual engine. At this point, Swan had developed a modified knock integral that included species concentrations as well as simplified temperature and pressure relationships. In order to simplify the model even further, the concentration terms were replaced by the equivalence ratio since concentrations as a function of crank angle are also unknown on a real engine. With these simplifications, the working equation for the Modified Knock Integral Method [26] becomes:

$$\int_{IVC}^{SOC} \frac{1}{A\omega \exp\left(\frac{b\left(P_{IVC} v_c^{\gamma}\right)^n}{T_{IVC} v_c^{\gamma-1}}\right)} \phi^x \, d\theta = 1$$

$$where \quad v_c = \frac{V(\theta_{IVC})}{V(\theta)} \tag{2.41}$$

In Equation 2.41, P_{IVC} is the pressure at intake valve closing and T_{IVC} is the temperature at intake valve closing. It is evident from Equation 2.41 that the modified knock integral is very similar to the knock integral, with the exception of a few terms. For the modified knock integral, the remaining parameters A, b, n, x are constants that must be determined experimentally for each fuel. These constants were determined for C_7H_{16} using an engine geometry similar to that of the Hatz engine [Swan], and can be seen below in Table 2.3. The value for A in Table 2 contains an EGR term, which is the amount of exhaust gas recirculation being used on the engine. In this model, the EGR must be entered in as a percentage of the total intake charge. With these parameters known, the modified knock integral can now be plugged directly into the control model in order to approximate the onset of combustion.

Table 2.3: Combustion Parameters for the Modified Knock Integral Method

Parameter	Symbol	Value	Units
Modified Knock Integral Method Parameters	A	$(4.8EGR + 8.15) \times 10^{-7}$	sec
	EGR	2.99	%
	b	16909	K/KPa
	n	-0.1121	----
	x	-0.688	----
	γ	1.3	----

In order for the modified knock integral to be able to predict the combustion timing at various inlet conditions, it must first be initialized at some experimental data point. To accomplish this, the experimental data point corresponding to a combustion timing of 354.1 crank angle degrees was used since it was the most advanced. In order to initialize the modified knock integral then, this experimental timing value was plugged in as the upper limit of integration. With the integration limits now known, the engine and combustion parameters from Tables 2.1 and 2.2 were used in Matlab to numerically integrate the expression in Equation 2.41. This resulted in an integrated value for the modified knock integral that correlated with the experiment at one operating point. This integrated value could now be interpreted as a threshold value for the modified knock integral, that when held constant at various inlet conditions, would allow for the combustion timing to be tracked by the combustion model. The threshold value which was calculated for the modified knock integral method can be seen in Equation 2.42.

$$K_{th,\ MKIM} = 0.3624 \tag{2.42}$$

With the threshold now established, the next step was to simply vary the inlet conditions in the control model by changing the intake temperature from 170°C to 190°C in 5 degree increments, and see how well it tracked the combustion phasing as compared to the experiment. The results of this comparison can be seen below in Figure 2.3.

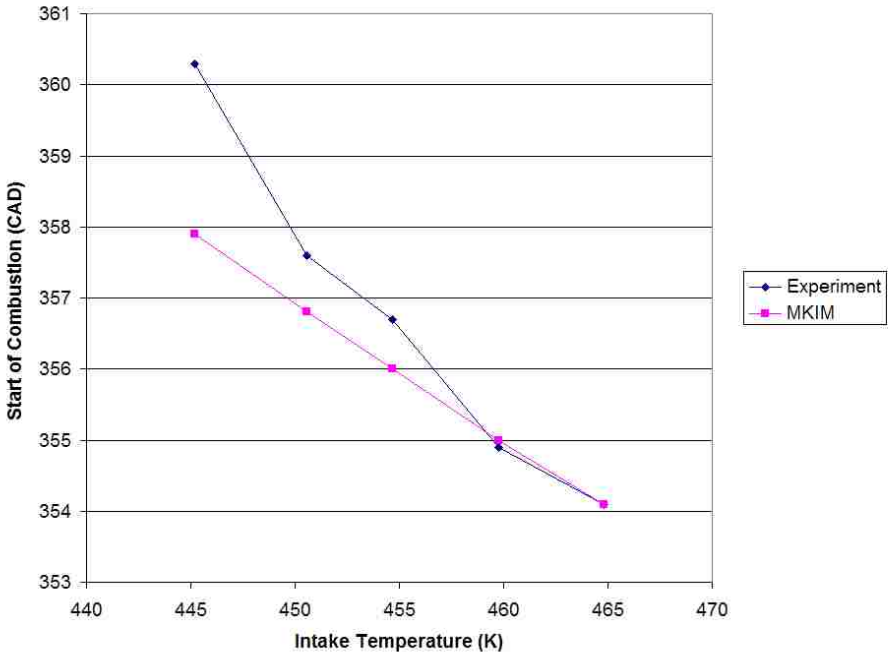

Figure 2.3: Modified Knock Integral Method combustion tracking

Figure 2.3 shows that the modified knock integral fails to capture the combustion phasing at different operating conditions. This is evident due to the fact that the slopes of the two lines are different. The experimental timing values vary about

6 crank angle degrees, while the values predicted by the modified knock integral only vary approximately 4 crank angle degrees. The modified knock integral and experiment both predict the same start of combustion value for the intake temperature of 445^{o}C, which is due to the fact that this is the experimental data point which was used for initialization. As the intake temperatures vary from the initialization point, the modified knock integral becomes less and less accurate. This method accurately predicts the correct trend for the onset of combustion, but the overall magnitudes differ significantly from those in the experiment. Even though the modified knock integral accounted for changes in reactant concentrations, it was still unable to accurately predict the combustion timing for different inlet conditions. Since accurate prediction of the combustion phasing is vital to the operation of the overall control model, the Modified Knock Integral Method was therefore dismissed as a possible combustion timing model.

2.5.2 Ignition Delay 1. The next combustion timing model to be investigated was that of Ignition Delay 1, which was incorporated from previous work by [27]. Similar to the Modified Knock Integral Method, this method also attempts to utilize the original knock integral in order to predict the onset of combustion in HCCI applications. The starting point for this model is the same knock integral introduced above in Equation 2.40. The limits of integration for this integral remain the same, with the upper limit being the crank angle at which combustion occurs and the lower limit being the crank angle of intake valve closing. From the initial integral, it can be seen that the combustion timing is directly related to both the engine speed and the ignition delay of the fuel being used. While the Modified Knock Integral Method attempted to add terms to this integral in order to account for reactant concentrations, the Ignition Delay 1 model [27] focuses on formulating a more detailed expression for the ignition delay of the fuel. Since the ignition delay in compression ignition engines governs when the fuel will ignite, then the ignition delay in HCCI applications would seem to govern when the mixture will auto-ignite. Therefore, if a detailed expression for the ignition delay can be generated, it should be able to track the onset of combustion. How accurately it predicts the combustion phasing then, will depend solely on the accuracy of the ignition delay expression itself. To this end, [27] strove to derive an expression for the ignition delay that would correlate with experimental data that he had collected. In order to derive this expression, [27] started with a physics based correlation for the ignition delay that assumed it was a function of temperature and pressure only. This correlation can be seen below in Equation 2.43:

$$\tau = C_1 P^{C_2} \exp\left(\frac{C_3}{T}\right) \tag{2.43}$$

where C_1, C_2, and C_3 are constants that must be experimentally determined. In order to make the expression more detailed, various terms were added in order to account for changes in the air/fuel ratio, the exhaust gas recirculation (EGR) rate and the engine speed [27]. The addition of these terms is important due to the fact that they will all directly affect the ignition delay time. The air/fuel ratio is a measure of how much fuel is injected each cycle, which will have an obvious impact on the ignition delay. The amount of EGR will also have an impact due to the fact that it effectively dilutes the reactant charge. Therefore, a high EGR rate should correspond to a longer ignition delay. With the addition of these terms, the new expression for the ignition delay in [27] becomes:

$$\tau = C_{1c} C_{2c} \lambda^{C_{3c}} \left(C_{4c}\, EGR^2 + C_{5c}\, EGR + C_{6c} \right) P^{C_{7c}} \exp\left(\frac{C_{8c}}{T} \right) \tag{2.44}$$

In Equation 2.44, λ is the air/fuel ratio, P is the cylinder pressure in (atm) as a function of crank angle, T is the cylinder temperature in (K) as a function of crank angle and the remaining values are constants that must be determined experimentally for each fuel. This ignition delay expression was calibrated using a 97-RON fuel on an engine with similar geometry to the Hatz [27], and the resulting constants can be seen below in Table 2.4.

Table 2.4: Combustion Parameters for Ignition Delay 1

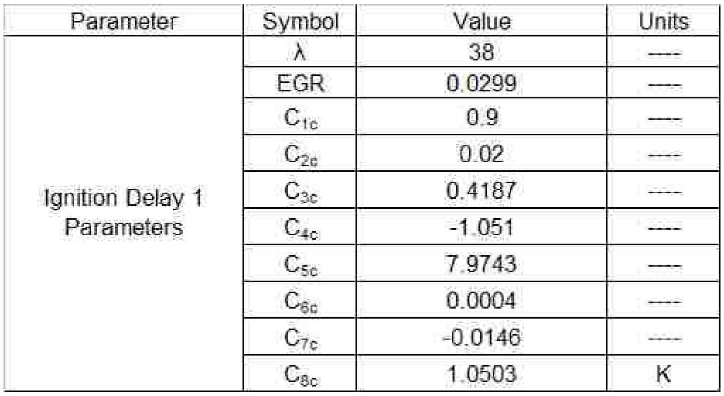

Parameter	Symbol	Value	Units
Ignition Delay 1 Parameters	λ	38	----
	EGR	0.0299	----
	C_{1c}	0.9	----
	C_{2c}	0.02	----
	C_{3c}	0.4187	----
	C_{4c}	-1.051	----
	C_{5c}	7.9743	----
	C_{6c}	0.0004	----
	C_{7c}	-0.0146	----
	C_{8c}	1.0503	K

The value for the air/fuel ratio in this model was determined from the equivalence ratio in Table 2.4. Also, the value for the EGR rate in this model is now a fraction rather than a percentage [27]. With these combustion parameters now known, the detailed expression for the ignition delay can now be plugged directly into the original knock integral in order to develop the working expression for the Ignition Delay 1 combustion timing model. This expression can be seen below in Equation 2.45.

$$\int_{IVC}^{SOC} \frac{1}{\omega\left(C_{1c}\, C_{2c}\, \lambda^{C_{3c}} \left(C_{4c}\, EGR^2 + C_{5c}\, EGR + C_{6c} \right) P^{C_{7c}} \exp\left(\frac{C_{8c}}{T} \right) \right)} \quad (2.45)$$

The expression seen in Equation 2.45 is the final result of [27], and is what will be plugged into the control model in order to approximate the onset of combustion.

In order to allow the ignition delay expression to predict the combustion timing at various inlet conditions, it must first be initialized at some experimental data point. To accomplish this, the experimental data point corresponding to a combustion timing of 354.1 crank angle degrees was used since it was the most advanced. In order to initialize the ignition delay expression in Equation 2.45 then, this experimental phasing value was plugged in as the upper limit of integration. With the integration limits now known, the engine and combustion parameters from Tables 2.2 and 2.4 could be plugged into Matlab in order to numerically integrate the expression in Equation 2.45. This resulted in an integrated value for the knock integral that correlated with the experiment at one operating point. This integrated value was again interpreted as a threshold value, that when held constant at various inlet conditions, would allow for the combustion timing to be tracked by the combustion model. The threshold value which was calculated for the Ignition Delay 1 model can be seen below in Equation 2.46.

$$K_{th,\ IgDel1} = 0.8567 \quad (2.46)$$

With the threshold now established, the inlet conditions in the control model could again be varied by changing the intake temperature in the same manner as stated previously. The resulting values of combustion phasing could then be compared directly to the experimental values in order to see how well they correlated. The results of this comparison can be seen below in Figure 2.4.

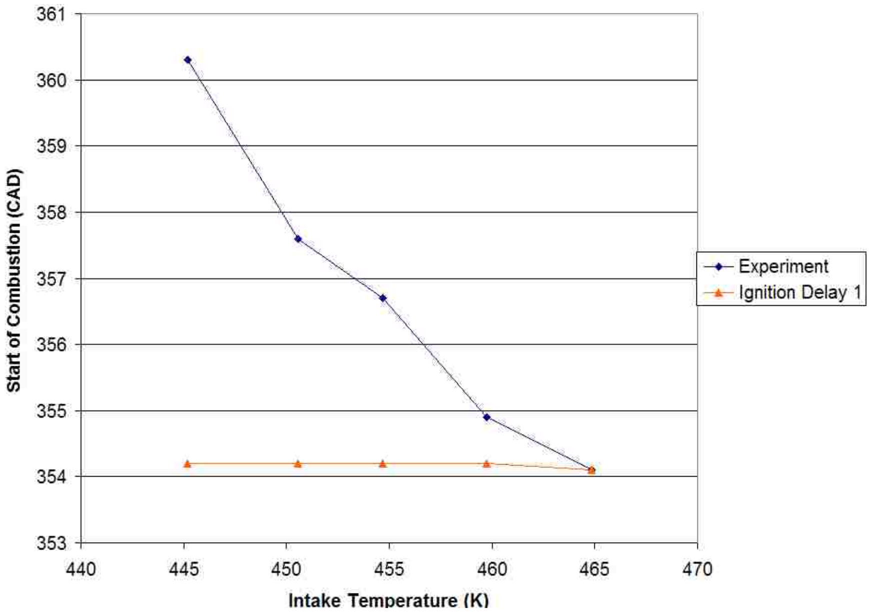

Figure 2.4: Ignition Delay 1 combustion tracking

Figure 2.4 shows that Ignition Delay 1 also fails to capture the combustion phasing at different operating conditions. This is evident due to the fact that the slopes of the two lines are again significantly different. The experimental timing values vary about 6 crank angle degrees, while the values predicted by the ignition delay model don't show any advance in the phasing whatsoever. The ignition delay and experiment both predict the same start of combustion value for the intake temperature of 170^{o}C, which is due to the fact that this is where they were initialized. As the intake temperatures vary from the initialization point, the experimental data shows that the combustion phasing advances. The Ignition Delay 1 combustion model, however, predicts constant combustion timing throughout the entire range of input temperatures. This method does not predict the correct trend for the onset of combustion, which results in values for the start of combustion that are drastically different than those in the experiment. The reason that this ignition delay model seems to predict constant combustion phasing may be due to the fact that the expression for the ignition delay failed to account for the reactant concentrations explicitly. Since HCCI combustion depends so heavily on the chemical kinetics, not properly accounting for the varying concentrations can lead to inaccurate results. Even though the Ignition Delay 1 model accounted for changes in the air/fuel ratio, it was still unable to accurately predict the combustion timing for different inlet conditions. Once again, since accurate prediction of the combustion phasing is vital to the operation of the overall control model, the Ignition Delay 1 model was also dismissed as a possible combustion timing model.

2.5.3 Ignition Delay 2. Following along with the idea of the knock integral, the next combustion timing model to be investigated was that of Ignition Delay 2, which was incorporated from previous work by [28]. Identical to the Ignition Delay 1 model, this method again attempts to utilize the original knock integral in order to predict the onset of combustion in HCCI applications. The starting point for this model is again the same knock integral introduced in Equation 2.40. The limits of integration for this integral remain the same, with the upper limit being the crank angle at which combustion occurs and the lower limit being the crank angle of intake valve closing. From the initial integral, it can be seen that the combustion timing is directly related to both the engine speed and the ignition delay of the fuel being used. Again identical to Ignition Delay 1 [27], the Ignition Delay 2 [28] model focuses on formulating a detailed expression for the ignition delay that can then be used with the knock integral. If a detailed expression for the ignition delay can be generated, it should theoretically be able to track the onset of combustion. How accurately it predicts the combustion phasing, however, will again depend solely on the accuracy of the ignition delay expression itself. To this end, an expression for the ignition delay that would correlate well with experimental data was formulated [28]. In order to derive this expression, [28] started with the same physics based correlation for the ignition delay that assumed it was a function of temperature and pressure only. This correlation can be seen again in Equation 2.47 below:

$$\tau = C_1 P^{C_2} \exp\left(\frac{C_3}{T}\right) \tag{2.47}$$

where C_1, C_2, and C_3 are constants that must be experimentally determined. In order to make the expression more detailed, various terms were added in order to account for changes in both the equivalence ratio and the oxygen mole percentage [28]. The addition of these terms is important due to the fact that they will both directly affect the ignition delay time. The equivalence ratio is a measure of how much fuel is injected each cycle, which will have an obvious impact on the ignition delay. The oxygen mole percentage accounts for the varying reactant concentrations that the previous ignition delay model left out. With the reactant concentrations now accounted for, this ignition delay model has the potential to track the onset of combustion more accurately. With the addition of these terms, the new expression for the ignition delay in [28] becomes:

$$\tau = C_{1c}\, P^{n}\, \phi^{m}\, {\chi_{o_2}}^{k} \exp\left(\frac{E_a}{R_u T}\right) \tag{2.48}$$

In Equation 2.48, P is the cylinder pressure in (atm) as a function of crank angle, T is the cylinder temperature in (K) as a function of crank angle, ϕ is the equivalence ratio, χ is the oxygen mole percentage and the remaining values are constants that must be determined experimentally for each fuel. This ignition delay expression was calibrated using isooctane on an engine with similar geometry to the Hatz [28], and the resulting constants can be seen below in Table 2.5.

Table 2.5: Combustion Parameters for Ignition Delay 2

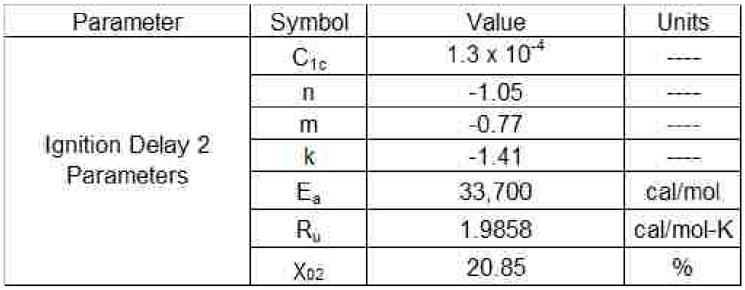

Parameter	Symbol	Value	Units
Ignition Delay 2 Parameters	C_{1c}	1.3×10^{-4}	----
	n	-1.05	----
	m	-0.77	----
	k	-1.41	----
	E_a	33,700	cal/mol
	R_u	1.9858	cal/mol-K
	X_{02}	20.85	%

With these combustion parameters now known, the detailed expression for the ignition delay can now be plugged directly into the original knock integral in order to develop the working expression for the Ignition Delay 2 combustion timing model. This expression can be seen below in Equation 2.49.

$$\int_{IVC}^{SOC} \frac{1}{\omega\left(C_{1c}\ P^{n}\ \phi^{m}\ \chi_{o_2}{}^{k}\ \exp\left(\frac{E_a}{R_u T}\right)\right)} \tag{2.49}$$

The expression seen in Equation 2.49 is the final result of [28], and is what will be plugged into the control model in order to approximate the onset of combustion.

In order to allow the ignition delay expression to predict the combustion timing at various inlet conditions, it must first be initialized at some experimental data point. To accomplish this, the same experimental data point as the previous two combustion models was used. In order to initialize the ignition delay expression in Equation 2.49, the experimental start of combustion was plugged in as the upper limit of integration. With the integration limits and combustion parameters now known, Matlab was used to numerically integrate the expression in Equation 2.49. This resulted in an integrated value for the knock integral that correlated with the experiment at one operating point. This integrated value was again interpreted as the threshold value, that when held constant at various inlet conditions, would allow for the combustion timing to be tracked by the combustion model. The threshold value which was calculated for the Ignition Delay 2 model can be seen below in Equation 2.50.

$$K_{th,\ IgDel2} = 0.3475 \tag{2.50}$$

With the threshold now established, the inlet conditions in the control model could again be varied by changing the intake temperature. The resulting values of combustion phasing could then be compared directly to the experimental values in order to see how well they correlated. The results of this comparison can be seen below in Figure 2.5.

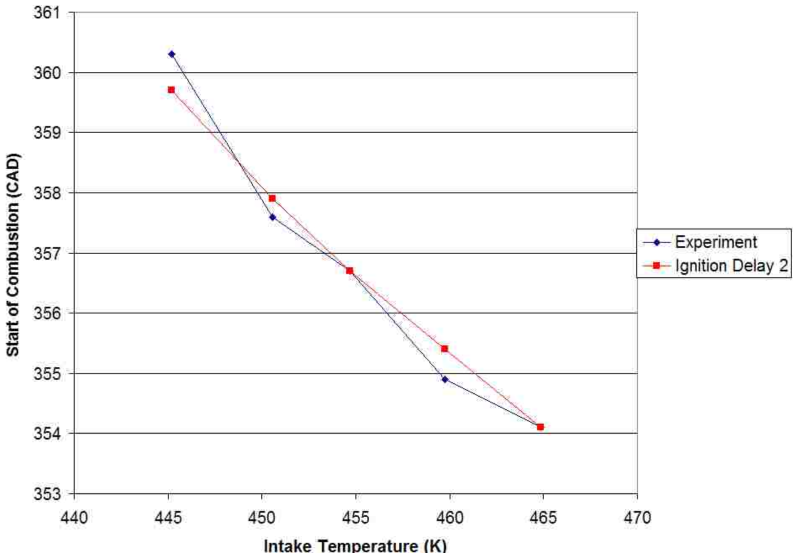

Figure 2.5: Ignition Delay 2 combustion tracking

Figure 2.5 shows that Ignition Delay 2 does a good job of predicting the onset of combustion. Unlike the previous two combustion timing models, the Ignition Delay 2 model produces a line with slope that is very similar to that of the experiment. This shows that Ignition Delay 2 is accurately predicting both the correct trend in the combustion phasing as well as the magnitudes. Where as the previous combustion timing models seemed to be somewhat unaffected by changes in the intake temperature, this model displays the appropriate sensitivity to changes in the inlet conditions. While the Ignition Delay 2 model does a very good job of predicting the start of combustion, there is another aspect of the model that is not very attractive when it comes to implementation. The Ignition Delay 2 combustion parameters in Table 2.5 were experimentally determined in [28] using isooctane. Therefore, the expression for the ignition delay in [28] is parameterized specifically for isooctane. This means that if a different operating fuel is chosen, then this combustion model will fail to accurately predict the start of combustion due to the fact the parameters are no longer valid. Since the long term goal of the control model is to be able to apply it to different engines operating on various fuels, this combustion model could lead to obvious problems in the future. Therefore, due to the fact that the combustion parameters are only valid for isooctane, the Ignition Delay 2 model was also dismissed as a possible combustion timing model.

2.5.4 Ignition Delay 3. Continuing on with the concept of the knock integral, the next combustion timing model to be investigated was that of Ignition Delay 3, which was previously developed by [29]. This model once again tries to utilize the original knock integral in order to predict combustion timing for HCCI, and is once again based on the original knock integral shown in Equation 2.40. Similar to the previous two cases, the lower and upper limits of integration are once again the crank angle at which combustion occurs and intake valve closing, respectively. From the initial integral, it can once again be seen that the combustion timing is directly related to both the engine speed and the ignition delay of the fuel being used. Also similar to the previous two cases, the Ignition Delay 3 [29] model tries to utilize a more accurate ignition delay term within the knock integral in order to accurately predict the onset of combustion. How accurately it predicts the combustion phasing, however, will again depend solely on the accuracy of the ignition delay expression itself. Rather than using an experimentally determined ignition delay, this model utilizes an ideal Arrhenius expression which can be seen in Equation 2.51.

$$\tau = A\, P^{-a} \exp\left(\frac{E_a}{R_u T}\right) \tag{2.51}$$

where A, E_a, and a are empirical parameters that are determined from combustion kinetics experiments. Since the experimental data available uses a fuel chemically similar to C_7H_{16}, the corresponding Arrhenius rate parameters [29] can be used and can be seen in Table 2.6 below.

Table 2.6: Combustion Parameters for Ignition Delay 3

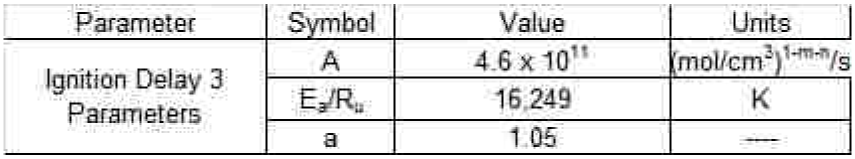

Parameter	Symbol	Value	Units
Ignition Delay 3 Parameters	A	4.6×10^{11}	$(mol/cm^3)^{1-m-n}/s$
	E_a/R_u	16,249	K
	a	1.05	----

With these parameters known, the ideal Arrhenius ignition delay expression could now be plugged directly into the knock integral in order to develop the working expression for the Ignition Delay 3 combustion timing model. Due to the fact that this model relied on the fact that combustion must occur close to TDC, the knock integral is therefore evaluated at TDC conditions, which is evident in Equation 2.52 below.

$$\frac{1}{\omega}\frac{1}{\tau_{TDC}}\int_{IVC}^{SOC}\frac{\tau_{TDC}}{\tau}\,d\theta = \frac{1}{\omega}\frac{1}{\tau_{TDC}}\int_{IVC}^{SOC}\left(\frac{P}{P_{TDC}}\right)^{a}\exp\left(\frac{E_a}{R_u T_{TDC}}\left(1-\frac{1}{T/T_{TDC}}\right)\right)d\theta \tag{2.52}$$

In order to allow the knock integral expression in Equation 2.52 to predict combustion timing values, it was initialized using the same experimental data point as in the previous three models. With the start of combustion (354 CAD) and IVC (228 CAD) known from experiment, the expression in Equation 2.52 was numerically integrated using Matlab's quadl function. This resulted in an integrated value for the knock integral that correlated with the experiment at one operating point. This integrated value was again interpreted as the threshold value, that when held constant at various inlet conditions, would allow for the combustion timing to be tracked by the combustion model. The threshold value which was calculated for the Ignition Delay 3 model can be seen below in Equation 2.53.

$$K_{th,\ IgDel3} = 0.00742 \tag{2.53}$$

With the threshold now established, the intake temperature within the model could again be varied in order to vary the combustion timing. These values could then be directly compared to the experimental values in order to see how well they matched. The results of this comparison can be seen below in Figure 2.6.

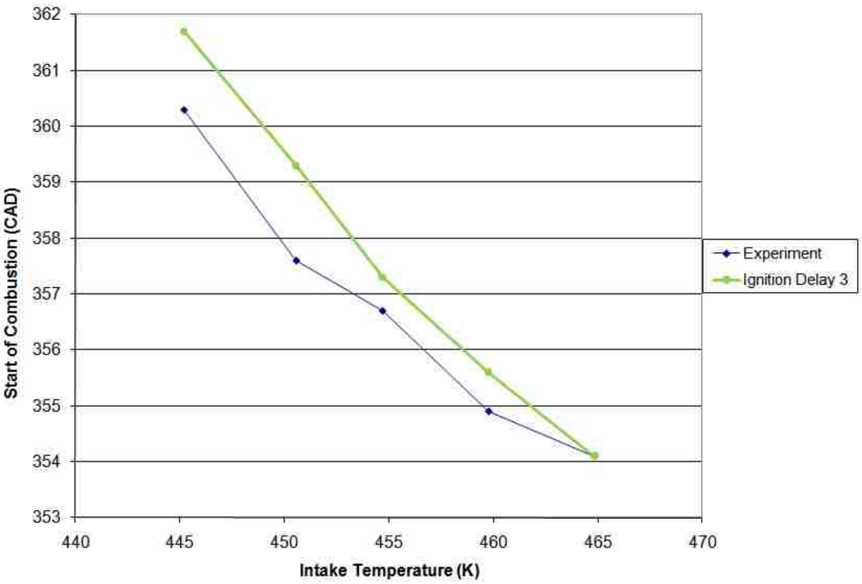

Figure 2.6: Ignition Delay 3 combustion tracking

Figure 2.6 shows that Ignition Delay 3 does a fairly reasonable job of predicting combustion timing. Unlike the previous models, however, the Ignition Delay 3 model produces a line with a slightly greater slope than that of the experiment and therefore over-predicts the onset of combustion for a given intake temperature. Despite this slight over-prediction, the Ignition Delay 3 model displays an appropriate sensitivity to changes in the inlet temperature, which make it a reasonable candidate for use in the overall model. Another advantage over the previous models lay in the utilization of an Arrhenius type ignition delay. While previous models have required experimentally determined parameters specific to a given fuel, the Arrhenius expression of Ignition Delay 3 uses Arrhenius parameters [31] which have been well documented for a number of different fuels. This suggests that this particular model would be significantly more robust to changes in fuel type due to the fact that the Arrhenius ignition delay parameters have been previously calculated. Despite these apparent advantages, however, the Ignition Delay 3 model stipulates that combustion must occur very close to TDC. As the ignition timing moves away from TDC, the ignition delay expression in Equation 2.52 becomes less and less accurate. Therefore, due to the fact that the ignition delay expression is only valid at or near TDC, the Ignition Delay 3 model was also dismissed as a possible combustion timing model.

2.5.5 Integrated Arrhenius Rate. The final combustion timing model to be investigated was called the Integrated Arrhenius Rate model [13]. Rather than trying to optimize the knock integral, the Arrhenius rate model takes a different approach which focuses more heavily on the conclusion that both the temperature and the reactant concentrations have the largest effect on HCCI combustion. This fact is again due to the dependence of HCCI combustion on chemical kinetics. In reality, the combustion process is made up of numerous sub-reactions that transform the reactants into products. Due to the fact that these sub-reactions may contain hundreds of different steps, they are very complex and difficult to model. Due to these complexities, utilizing these sub-reactions to model combustion in a control oriented model is unrealistic due to the fact that a control model must remain simple. In an attempt to simplify things then, the overall combustion reaction is instead modeled by a single global reaction rate. The reaction rate chosen to represent the overall combustion reaction is that of a single Arrhenius reaction rate [13]. The Arrhenius rate is a physics based reaction rate that is used for individual reactions in complex models with detailed chemistry. In the case of the control model, however, it will act to relate the combustion reaction to both the temperature and the reactant concentrations in the cylinder. Since these are the two parameters that most greatly affect HCCI combustion, this single Arrhenius reaction rate also has the potential of tracking the onset of combustion with a high level of fidelity. Mathematically, this model involves the integration of a single Arrhenius reaction rate expression [13]. Similar to the integration of the knock integral, the limits of integration in this case will again be from the crank angle of intake valve closing to the crank angle at which combustion occurs. These limits are again chosen due to the fact that any appreciable reactions will begin with the compression stroke and continue until the onset of combustion. This Integrated Arrhenius Reaction Rate [13] can be seen below in Equation 2.54.

$$\int_{IVC}^{SOC}\left(\frac{A\exp\left(-E_a/_{R_uT}\right)[fuel]^a[O_2]^b}{\omega}\right)d\theta \tag{2.54}$$

The expression in Equation 2.54 contains concentration terms for both the fuel and oxygen in the reactants, along with the engine speed, ω, in (rad/sec). The reactant concentrations can be determined using the combustion reaction in Equation 2.38, along with the cylinder volume. The remaining constants A, E_a/R_u, m and n are empirical parameters that are determined from combustion kinetics experiments [31] for various types of fuels. As described previously, the current study focuses on gasoline-type fuels in order to eliminate the complexities associated with low temperature heat release. Since the experimental data available uses UTG96 as a fuel, which is chemically similar to C_7H_{16}, the corresponding Arrhenius rate parameters [31] can be used and can be seen in Table 2.7 below. With the combustion parameters known for C_7H_{16}, the Arrhenius Rate model can now be plugged directly into the control model in order to approximate the onset of combustion.

Table 2.7: Combustion Parameters for the Integrated Arrhenius Rate

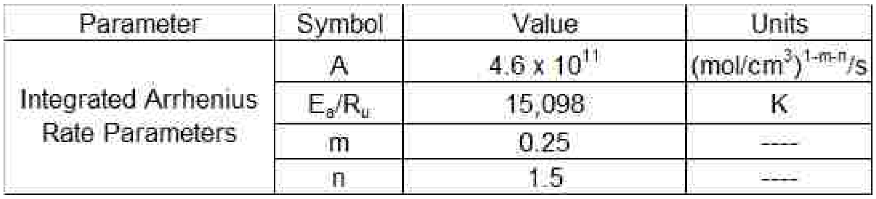

Parameter	Symbol	Value	Units
Integrated Arrhenius Rate Parameters	A	4.6×10^{11}	$(mol/cm^3)^{1-m-n}/s$
	E_a/R_u	15,098	K
	m	0.25	----
	n	1.5	----

In order to allow the Arrhenius rate expression to predict the combustion timing at various inlet conditions, it must first be initialized at some experimental data point. This data point was chosen to be the same as in the previous combustion models investigated. In order to initialize the ignition delay expression in Equation 2.54, the experimental start of combustion was again plugged in as the upper limit of integration. With the integration limits and combustion parameters now known, Matlab was again used to numerically integrate the expression in Equation 2.54. This resulted in an integrated value for the Arrhenius rate that correlated with the experimental start of combustion point of 354.1 CAD. This integrated value was again the threshold value, that when held constant at various inlet conditions, would allow for the combustion timing to be tracked by the combustion model. In other words, the threshold value was calculated at one operating point and held constant at all others. This threshold value which was calculated for the Integrated Arrhenius Rate model can be seen below in Equation 2.55.

$$K_{th,\ Arrhen} = 1.4625\ x\ 10^{-6} \tag{2.55}$$

With the threshold established, the model can now be run at various inlet temperatures in order to verify whether or not the combustion phasing is being tracked accurately. The inlet temperatures are again varied from 170^{o}C to 190^{o}C in 5 degree increments in order to be consistent with the temperature change in the experiment. The combustion tracking results for the Arrhenius rate can be found below in Figure 2.7.

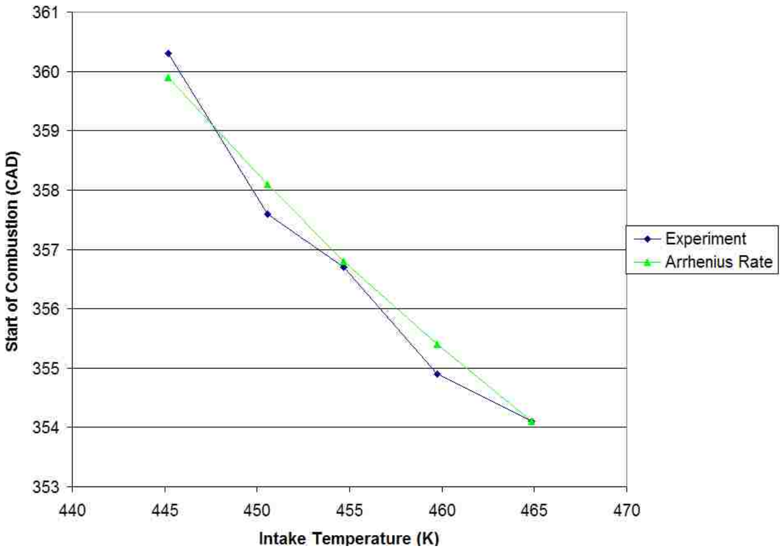

Figure 2.7: Integrated Arrhenius Rate combustion tracking

Figure 2.7 shows that the Integrated Arrhenius Rate model does an even better job of predicting the onset of combustion. Just like the Ignition Delay 2 model, this model also produces a line with a slope very similar to that of the experiment. This shows that the Arrhenius rate is accurately predicting both the correct trend in the combustion phasing as well as the magnitudes. Also similar to Ignition Delay 2, the Arrhenius model also displays the appropriate sensitivity to changes in the inlet conditions. Unlike the Ignition Delay 2 model, however, the Integrated Arrhenius Rate model does not contain any shortcomings with respect to the combustion parameters. Since the Arrhenius rate is a well known expression, there is a collection of combustion parameters for many different types of fuels. This means that the Integrated Arrhenius Rate [Shaver] model can be much more robust than the Ignition Delay 2 [28] model when it comes time to switch fuels. Therefore, the Arrhenius rate model seems to be an accurate and robust method for predicting the onset of combustion. Since accurate prediction of the combustion phasing is central to the operation of the control model, the Integrated Arrhenius Rate [13] model seems to be the best choice for the combustion timing model due to both its simplicity and accuracy.

2.5.5.1 Prediction of Pressure Evolution. One more thing that must be investigated before choosing the Integrated Arrhenius Rate as the combustion timing model is whether or not it allows for accurate prediction of the pressure evolution in the cylinder. As mentioned previously, while the combustion phasing is the most important aspect of the combustion timing model, it must also be able to predict accurate trends in the pressure evolution. This will allow the model to accurately predict the work output from the engine. In order to verify whether the pressure is being tracked, the same Arrhenius rate expression and parameters used to track the combustion timing can be utilized. The only difference being that this time the pressure predicted by the model will be compared to the experiment rather than the combustion phasing values. These pressure trace comparisons for several different inlet temperatures can be seen below in Figures 2.8-2.10.

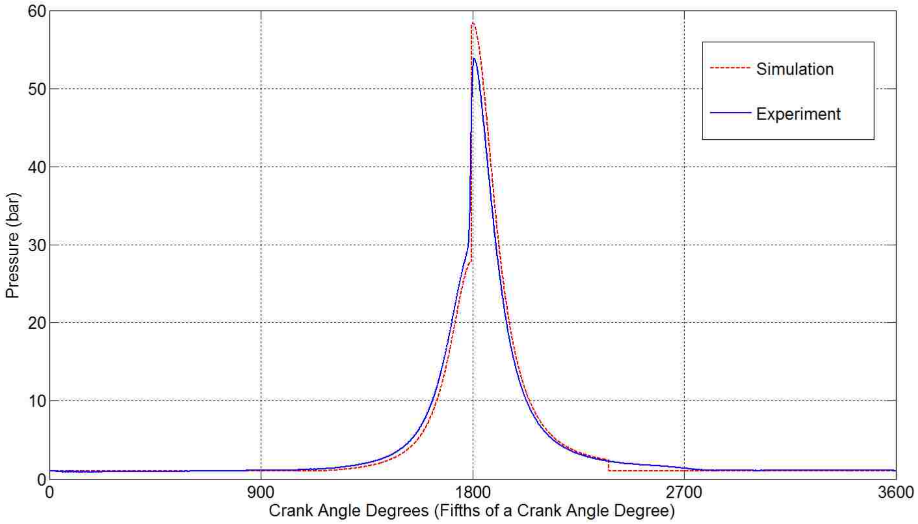

Figure 2.8: Integrated Arrhenius Rate pressure comparison for an intake temperature of 190^{o}C

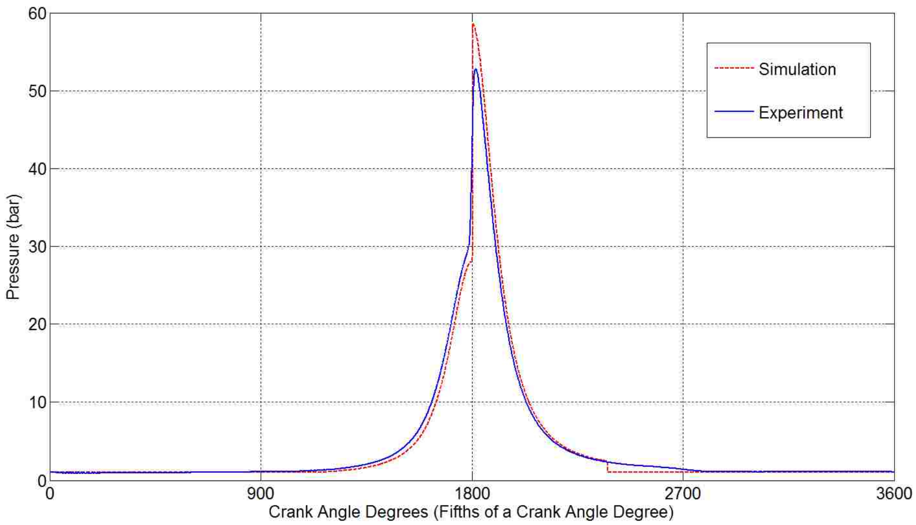

Figure 2.9: Integrated Arrhenius Rate pressure comparison for an intake temperature of 185°C

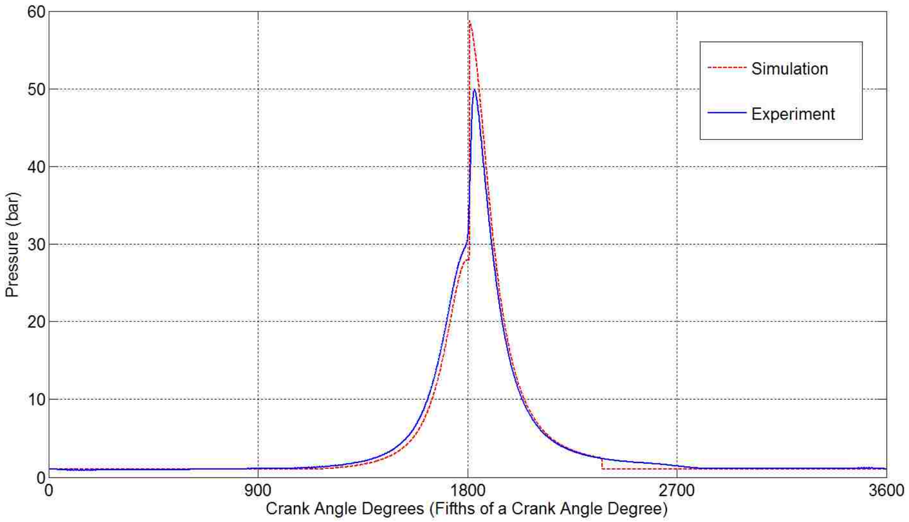

Figure 2.10: Integrated Arrhenius Rate pressure comparison for an intake temperature of 180°C

These figures show that the Integrated Arrhenius Rate [13] model does in fact trace the pressure evolution fairly accurately. As can be seen in the figures above, the pressure traces basically lie on top of one another at every point throughout the entire cycle. The only exception to this occurs at the crank angle of peak pressure, where the model seems to slightly over-predict the value for the peak pressure. Even with this slight over-prediction of the peak pressure, the values predicted by the model are still within ten percent of the experimental values. Recognizing that the Arrhenius rate is a somewhat simplified combustion timing model, these percent errors are therefore within an acceptable tolerance and are surprisingly good. The ability of the Arrhenius rate to accurately track the pressure evolution in the cylinder for varying inlet temperatures suggests that it will also be able to track the work output from the engine. Although this Integrated Arrhenius Rate [13] model is greatly simplified, it manages to track both the combustion phasing and the pressure evolution with a high level of accuracy, which can again be seen in Figures 2.7-2.10. With its credibility now verified, the Integrated Arrhenius Rate model can now be confidently chosen to be the working combustion timing model for the overall control model.

2.5.5.2 Arrhenius Rate Sensitivity. With the Integrated Arrhenius Rate model now chosen to be the combustion timing model, a closer inspection is required in order to fully understand its operation. The first aspect of the model that needs to be investigated has to do with its sensitivity to the parameters that define it. The three parameters of interest in this case are the exhaust gas recirculation term, α, the heat transfer term, χ, and the activation energy term, E_a. The exhaust gas recirculation term enters the Arrhenius expression in Equation 2.54 through the concentration terms via the combustion reaction. If EGR is used on the engine, the combustion reaction in Equation 2.38 will contain additional terms to represent it. These α terms will then contribute to the species concentrations. The heat transfer term enters into the

Arrhenius expression through the ever present residual gas that is trapped in the cylinder after each cycle. These trapped product gases act to increase the temperature of the inlet air, which is what the heat transfer term, χ, is meant to represent. The activation energy term is slightly different in that it is a part of the original Arrhenius expression itself. This term is meant to represent the energy required for the combustion reaction to initiate. Since both the EGR and heat transfer terms can change from cycle to cycle, and the activation energy is an experimentally determined value, it is important to investigate the effect these changes will have on the ability of the Arrhenius rate to predict combustion timing.

In order to examine the sensitivity to the EGR rate, the values for α are varied in the control model with all other parameters being held constant. Since α is the only parameter changing from case to case, any changes in the combustion timing can then be attributed directly to the changing internal EGR rate. In order to run the simulation, the same approach was taken as mentioned previously. The integral was again initialized at the same experimental data point in order to come up with an integrated value for the Arrhenius rate expression. This integrated value was again the threshold value, which was held constant at all inlet conditions in order to predict the onset of combustion in the control model. Due to the fact that the Arrhenius integral in Equation 2.54 contains an α term, the integrated threshold value will therefore change slightly with changes in α. These threshold values were calculated for various internal EGR rates, and the corresponding phasing values were recorded for each case. The results of this analysis can be seen below in Figure 2.11.

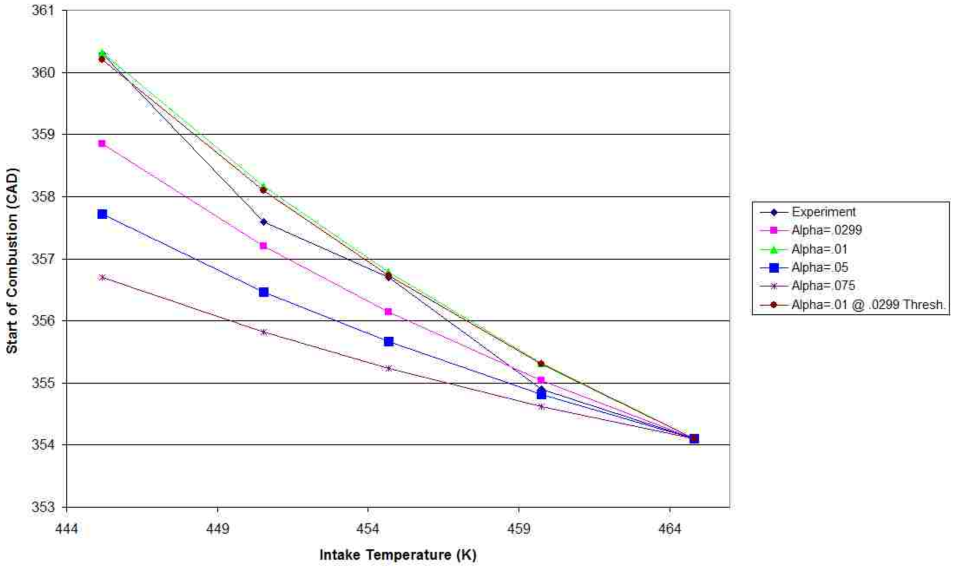

Figure 2.11: Integrated Arrhenius Rate sensitivity to α

From Figure 2.11 it is evident that the EGR rate, α, does in fact have an impact on the ability of the control model to predict the combustion timing. As the value of α is increased, the Arrhenius rate model seems to get increasingly less sensitive to changes in the inlet temperature. Even though this trend causes the model to digress slightly from the experiment, the model can still be used due to the fact that the sensitivity is fairly low. This does suggest, however, that moderate care need be taken in determining the EGR fraction, as it will have a slight impact on the overall performance of the model. Also included in Figure 2.11 is a case for which the threshold value is calculated at one value of α, and the simulation is run at a different value. This is represented by the brown line on the plot. The conclusion that can be drawn from this case is that once a threshold is determined, varying α in the model will have a very minimal effect on the ability to predict the phasing.

The next parameter of interest is the heat transfer term. In order to determine the sensitivity of the Arrhenius rate expression to this term, the same procedure that was just carried out for the EGR rate can be repeated. The χ term will now be varied in the model, while all other parameters are held constant. This will allow for any changes in the combustion timing to now be directly attributed to changes in the heat transfer term. The simulation was again run by initializing the Arrhenius integral in Equation 2.54 at the same experimental data point. This resulted in another threshold value, this time related to the heat transfer term. Since the Arrhenius integral also includes the heat transfer term, χ, the threshold value will once again change slightly as the parameter is varied. These threshold values were calculated for several different values of χ, and were plugged into the control model in order to track the corresponding onset of combustion. These results are summarized in Figure 2.12 below.

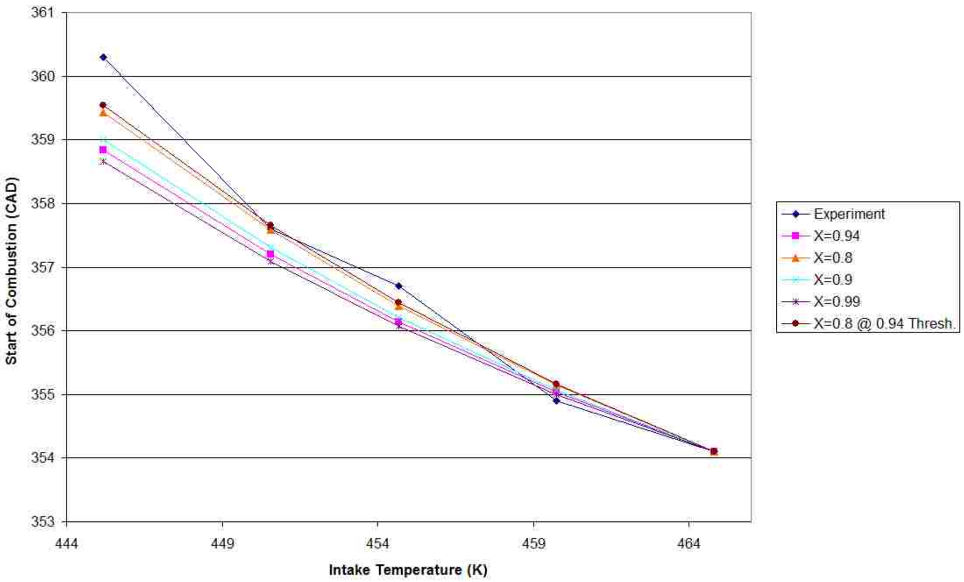

Figure 2.12: Integrated Arrhenius Rate sensitivity to χ

From Figure 2.12 it is evident that the heat transfer term has only a slight effect on the ability of the model to predict the phasing. Even though the Arrhenius rate seems to get less sensitive to changes in the inlet temperature as the value of χ increases, the change is very minimal. This proves that the Arrhenius rate expression has a very low sensitivity to changes in the heat transfer term. Also present in Figure 2.12 is a case for which the threshold is calculated at one value of χ, and the simulation is run at a different value. Similar to the previous case, it is evident that varying the χ term in the model will again have a very minimal effect on its ability to predict the combustion timing.

The final parameter of interest is the activation energy term. In order to determine the sensitivity for this case, the E_a terms will be varied while the other parameters are again held constant. This will allow any changes in the combustion timing to now be attributed directly to changes in the activation energy. The simulation was once again run by initializing the Arrhenius integral in Equation 2.54 at the same experimental data point. This resulted in yet another threshold value, this time related to the activation energy term. Since the activation energy is a part of the original Arrhenius expression, the threshold value will change slightly as this parameter is varied. These threshold values were calculated for several different values of E_a, and were again plugged into the control model in order to track the corresponding combustion timing. These results can be seen in Figure 2.13 below.

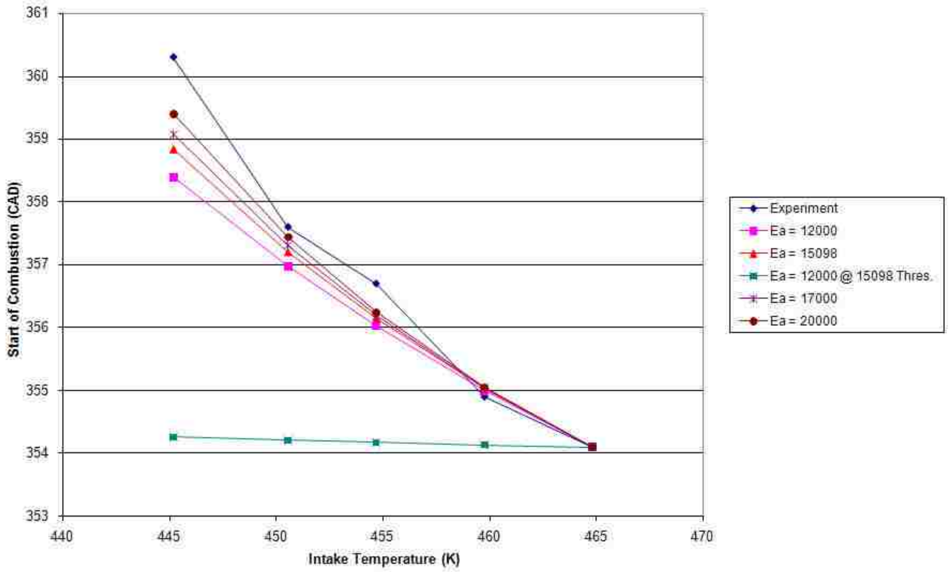

Figure 2.13: Integrated Arrhenius Rate sensitivity to E_a

From Figure 2.13 it is evident that the activation energy also slightly affects the ability of the model to predict the phasing. It appears as though the Arrhenius rate gets more sensitive to changes in the inlet temperature as the activation energy, $E_{a,}$ increases. Even though the sensitivity does increase with inlet temperature, the change is very small when compared with the overall magnitudes. This now verifies that the Arrhenius rate expression has a low sensitivity to changes in the activation energy term. Similar to the previous cases, Figure 2.13 also contains a case for which the threshold value is calculated at one value of E_a, and the simulation is run at another. Unlike the previous two cases, Figure 2.13 shows that the simulation must use the activation energy that corresponds to the threshold value being used. If the activation energy is varied within the simulation and the threshold value is not, the models' ability to track the combustion timing is severely altered. This fact is not detrimental to the model, however, due to the fact that the activation energy is representative of the fuel being used. Since the type of fuel will remain constant for a given application, the activation energy used to calculate the threshold value will also be the one used within the model. It can be concluded then, that the Arrhenius rate model has a low sensitivity to changes in the activation energy. As long as the same activation energy is used to both calculate the threshold value and predict the onset of combustion, the particular value chosen will not drastically affect the overall performance of the model. As a result of this sensitivity investigation, it was shown that the Arrhenius rate expression has a low sensitivity to the exhaust gas recirculation term, the heat transfer term and the activation energy term. The fact that the sensitivity is low, suggests that the exact determination of these parameters is not crucial to the operation of the overall control model.

2.5.5.3 Integrated Arrhenius Rate Simplifications. Despite the fact that the Arrhenius rate combustion timing model is already simplified with respect to the chemical kinetics, there are still a few aspects which prevent it from being directly implemented in a control based model. One of these obstacles has to do with the concentration terms within the Arrhenius integral. As can be seen in Equation 2.54, these concentrations of fuel and oxygen are functions of crank angle. This means that the Arrhenius integral must calculate the concentrations of both fuel and oxygen at every crank angle in order to operate. This requires calculating the moles of reactant and the volume at each and every crank angle. Therefore, calculating these concentrations on the fly gives rise to several concerns regarding the performance of the control model. Firstly, these calculations will effectively increase the computational time of the model due to the fact that they must be made at every crank angle. Since a control model generally requires that the computational time be kept to a minimum, these concentration calculations must be simplified in order for the model to operate efficiently. It is also necessary to simplify these calculations due to the fact that reactant concentrations as a function of crank angle are unknown on actual engines. A straightforward approach to simplifying these concentrations is to evaluate them at some constant crank angle throughout the entire integration. This would eliminate the need to calculate the concentrations at every single crank angle, which would help to decrease the computational time and also make the model more applicable to real engines. While evaluating the concentrations at a constant crank angle acts to simplify the Arrhenius integral, the actual angle at which to evaluate them must still be chosen. The most logical crank angle in this respect seems to be top dead center. This choice seems to make sense due to the fact that combustion is generally going to occur somewhere around top dead center, which represents the end of the compression stroke. With this assumption applied, the Integrated Arrhenius Rate integral becomes:

$$\int_{IVC}^{SOC} \left(\frac{A \exp\left(-E_a / R_u T \right) [fuel]^a{}_{TDC} [O_2]^b{}_{TDC}}{\omega} \right) d\theta \qquad (2.56)$$

In order to verify whether or not this simplification is reasonable, the integrands from Equations 2.54 and 2.56 can be plotted and compared. The integrands were plotted and can be seen below in Figure 2.14.

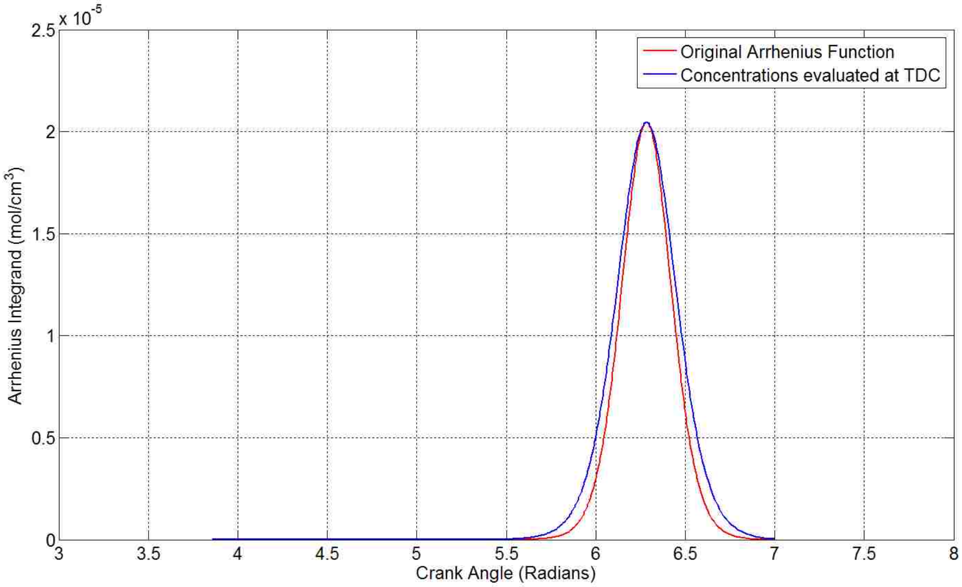

Figure 2.14: Arrhenius integrand plots

From Figure 2.14 it can be seen that evaluating the concentrations at top dead center produces almost identical behavior from the Arrhenius expression. Based on this plot, it was decided that evaluating the concentrations at top dead center was therefore an acceptable simplification due to the fact that it greatly simplified the combustion timing model, while still preserving its accuracy.

With the Arrhenius expression concentrations now simplified, the next step is to verify whether or not it is still capable of predicting the onset of combustion. In order to accomplish this, the same basic procedure of setting a threshold at one operating point can be used. In this case, the newly simplified Arrhenius expression in Equation 2.56 was initialized at the same experimental data point corresponding to an intake temperature of 190^{o}C. This variable temperature Arrhenius expression was integrated using Matlab in order to establish the new threshold value below.

$$K_{th} = 2.3072\,x\,10^{-6} \tag{2.57}$$

At this point, another simplification to the Arrhenius integral must be made in order to proceed. Similar to the reactant concentrations above, the temperature relationship within the integral is also a function of crank angle. Since this calculation will also work to increase the computational time of the model, it would seem appropriate to simplify it as well. For the same reasons as the concentration terms, this temperature relationship was simplified by evaluating it at top dead center. This resulted in an even further simplified Arrhenius expression which can be seen below.

$$\int_{IVC}^{SOC} \left(\frac{A\exp\left(-E_a \big/ R_u T_{TDC}\right) [fuel]^a{}_{TDC} [O_2]^b{}_{TDC}}{\omega} \right) d\theta \tag{2.58}$$

The threshold value in Equation 2.57 can now be applied to this newly simplified Arrhenius expression in order to track the combustion timing. First, however, it is important to recognize how the threshold value was calculated in this instance. The only reason for the further simplification seen in Equation 2.58 has to do with the computational time and physical applicability of the combustion timing model. Without this further simplification, the model would not be physically realizable due to the inherent complexities of calculating cylinder temperature as a function of crank angle. The threshold value, on the other hand, is calculated using the variable temperature Arrhenius expression in Equation 2.56. Since this expression contains fewer simplifications, the resulting threshold value will be more accurate than if it was calculated using Equation 2.58. This integration is possible due to the fact that the threshold value need only be determined at one operating point, and is then held constant at all others. In summary, the threshold value is calculated using the variable temperature relationship of Equation 2.56, while the simplified expression in Equation 2.58 is used to predict the combustion phasing within the model. The simulation was run under these conditions, and the results can be seen below.

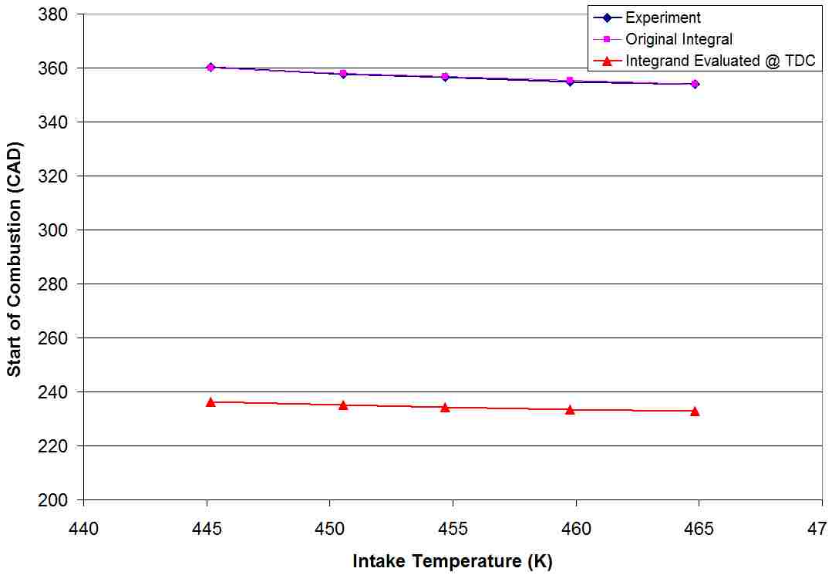

Figure 2.15: Integrated Arrhenius Rate combustion tracking with threshold value calculated using variable temperatures

Figure 2.15 shows the Arrhenius expression predicting phasing values that are offset from those of the experiment. This was expected, however, due to the fact that the threshold value was calculated using a different expression than the one used in the model, as described previously. Since the threshold calculation is what correlates the model with the experiment, the link that was constraining the two is now gone. Despite this offset, the slope of the line with the integrand evaluated at top dead center appears to be very similar to that of the experiment. In order to utilize the threshold calculated using variable temperatures in the integral then, some type of offset must be applied to the start of combustion values predicted by the integrand evaluated at top dead center. In order to be consistent, the same experimental data point corresponding to an intake temperature of 190°C is used to determine this offset value. In other words, the offset value is merely the difference between the model and experiment for the inlet temperature of 190°C.

$$\theta_{offset} = 121.748 \tag{2.59}$$

This offset value was applied to the phasing values from the model, and the results can be seen below.

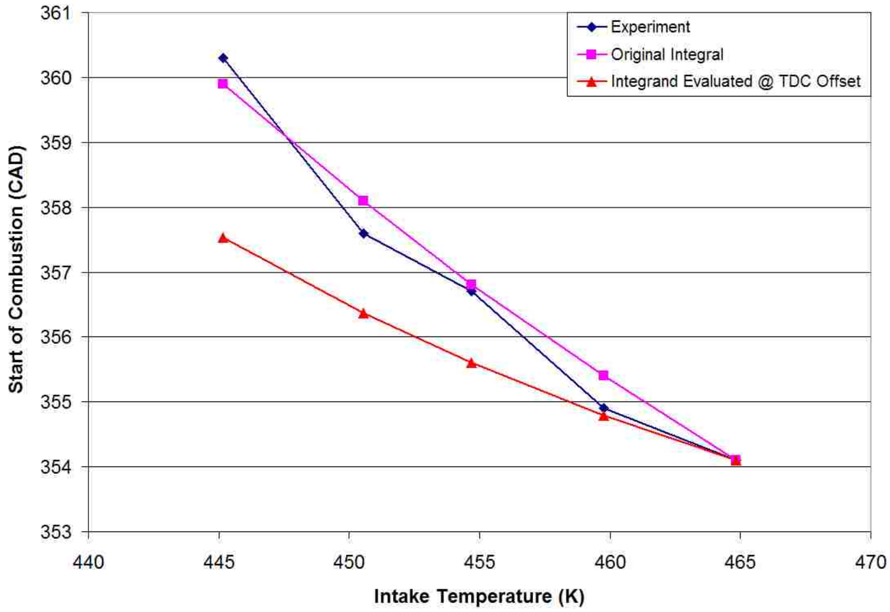

Figure 2.16: Integrated Arrhenius Rate combustion tracking with variable temperature threshold value and offset

The plot in Figure 2.16 displays good agreement between the experiment and the offset predictions from the model. This suggests that a variable temperature threshold value can be utilized along with evaluating the Arrhenius expression at top dead center in the combustion timing model. As long as an offset value is applied, the constant Arrhenius rate expression seems to still do a reasonable job of tracking the combustion timing. Also shown in Figure 2.16 are the values from the original Arrhenius integral without any simplifications. The plot shows that some accuracy is indeed lost in making all of these assumptions within the integral. However, the simplified Arrhenius expression still tracks the combustion phasing well enough for the needs of the control model. The fact that this simplified Arrhenius expression still tracks the onset of combustion so well leads to the conclusion that it can be implemented in the control model. This will greatly simplify the combustion timing model, and also act to significantly decrease its computational time.

Throughout the entire process of making simplifications to the Arrhenius expression, the lower limit of integration has been held constant at the crank angle of intake valve closing. This was done due to the fact that significant reactions will not take place until after the compression stroke has begun [1]. Even though this seems to be a very reasonable place to start the integration, it would be interesting to observe the effects of changing this lower limit. Once again using the simplified integral in Equation 2.58, along with the variable temperature threshold value and the corresponding offset, this scenario can now be investigated. The only thing necessary in order to accomplish this is to simply change the value for the lower limit of integration.

According to the Arrhenius integrand plot in Figure 2.14, the integrated threshold value should remain relatively unchanged until a crank angle of approximately 320 degrees. With this in mind, the lower limit of integration was varied between intake valve closing and 320 degrees in order to observe the effects on the model's ability to track the combustion timing. The results of this analysis can be seen below.

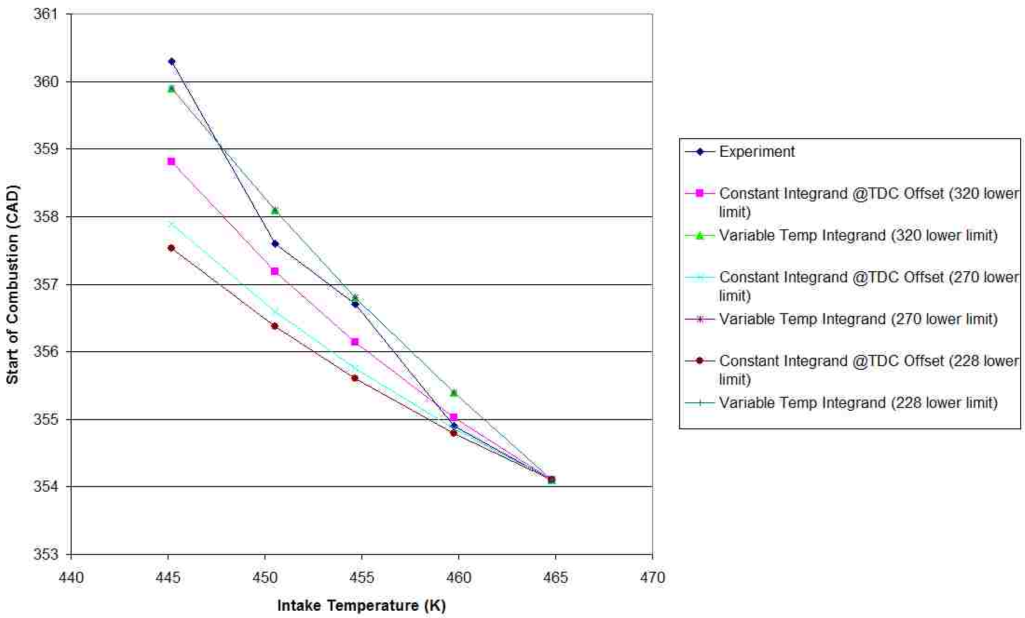

Figure 2.17: Integrated Arrhenius Rate combustion tracking with variable temperature threshold value and offset (varying lower limit of integration)

The plot in Figure 2.17 shows trends very similar to those in Figure 2.16. The combustion phasing values from the un-simplified Arrhenius expression are shown for each lower limit of integration. These lines all lie on top of one another, which suggests that the original integral is not at all sensitive to changes in the lower limit of integration. The original integral will track the combustion timing regardless of the integration limit chosen, provided that the appropriate threshold value is used. The simplified Arrhenius expression evaluated at top dead center, however, is affected by changes in the lower limit of integration. Although not very much, as the lower limit moves farther away from top dead center the slope of the line decreases. Even with this slight decrease in the slope, however, changing the lower limit of integration does not seem to drastically affect the combustion phasing. For this reason, the lower limit was therefore returned to its initial crank angle value of intake valve closing. This is also the most logical place to start the integration due to the fact that most reactions will begin with compression, as described previously.

2.6 VARIABLE Δθ CORRELATION

Due to the discrete nature of the model being used, a constant volume combustion event is assumed. This implies that there is an instantaneous energy release when combustion occurs within the model. Despite the fact that HCCI combustion is indeed fast, it is not perfectly instantaneous, and therefore requires some finite amount of time to occur. To account for this phenomenon within the model, a Δθ term has been added which shifts the point of instantaneous combustion from SOC to a point of very *high* energy release based on experimental heat release data. This Δθ is essentially the crank angle degrees between start of combustion and experimental CA50. Previous models for HCCI have also included a similar term to account for the fact that combustion is not actually instantaneous [4,13], and the general method seems to be to hold this term constant at every engine set point. Experimental combustion data from the Hatz engine, however, suggests that this Δθ term actually varies with engine set point. The experiment shows a strong correlation to the location of SOC, which can be seen in Figures 2.18 and 2.19 for the fueling rates of 9 grams/minute and 6 grams/minute, respectively.

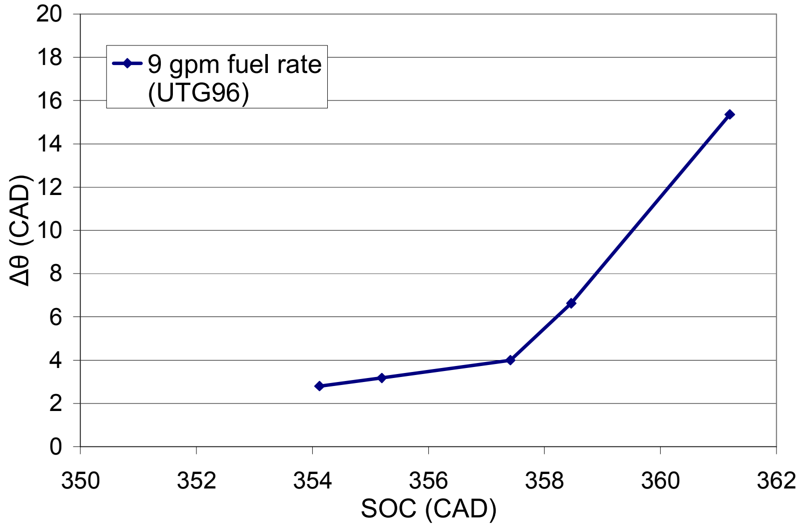

Figure 2.18: Δθ versus SOC for the fueling rate of 9 grams/minute

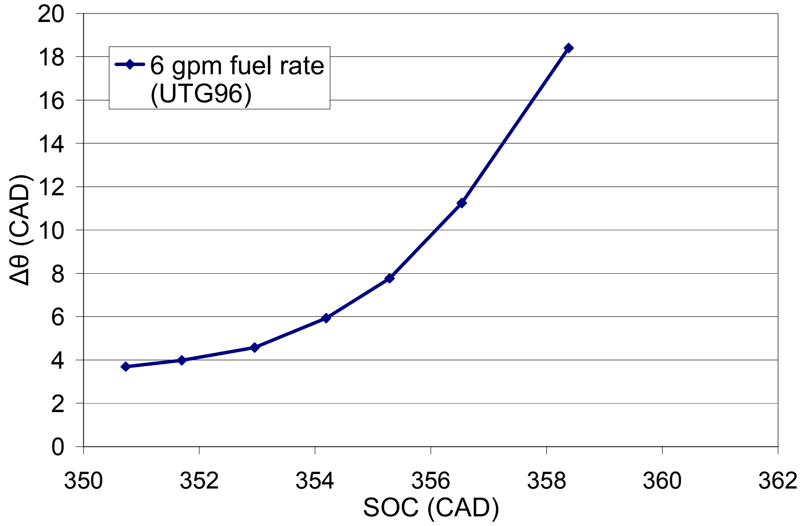

Figure 2.19: Δθ versus SOC for the fueling rate of 6 grams/minute

Based on this experimental data, it was decided that the inclusion of a variable Δθ was necessary in order to improve the accuracy of the model. Using the experimental data above for UTG96, a multivariable correlation for Δθ was developed based on a similar model previously developed in the literature [32], which related Δθ to chemical kinetics through reactant concentrations, SOC and the temperature at SOC. This correlation was developed using the same parameters, and can be seen in Equation 2.60.

$$\Delta\theta_{k+1} = \left\lfloor 2.0677\times10^{-18}\left(0.0000351555\right)^{\phi_k}\left(0.992961373\right)^{\left(V_1/V_{SOC,k+1}\right)^{\gamma-1}T_{1,k+1}}\left(1.16093521\right)^{\theta_{SOC,k+1}}\right\rfloor \qquad (2.60)$$

In order to verify the accuracy of this Δθ correlation, experimental values for the equivalence ratio, SOC and the temperature at SOC at various operating points were plugged into the expression in Equation 2.60, and the results were compared against the experimental Δθ values seen in Figures 2.18 and 2.19. The results of this analysis using UTG96 as the fuel can be seen in Figures 2.20 and 2.21.

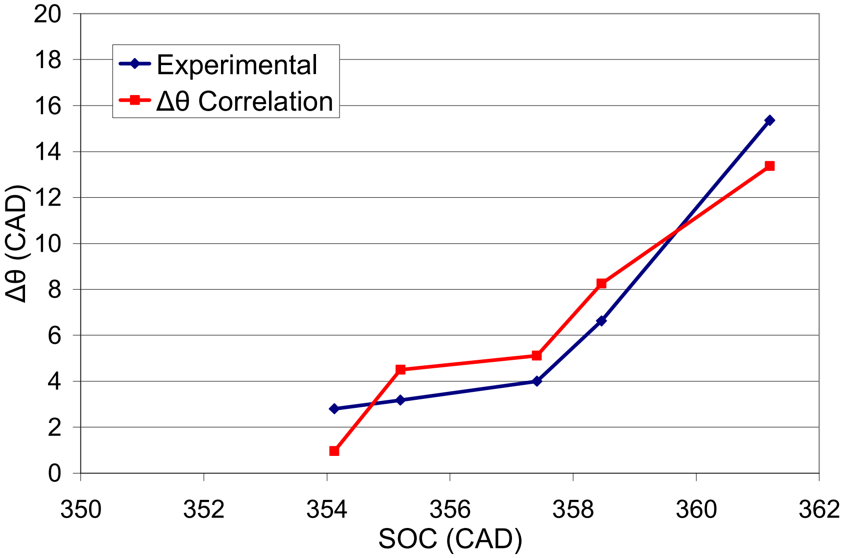

Figure 2.20: Comparison of Δθ between experiment and correlation using UTG96 at 9 grams/minute.

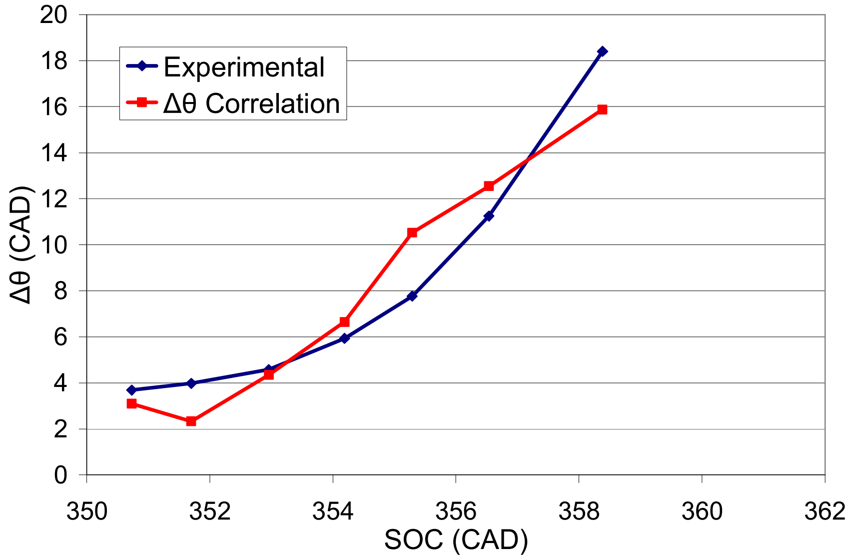

Figure 2.21: Comparison of Δθ between experiment and correlation using UTG96 at 6 grams/minute.

Figures 2.20 and 2.21 reveal that the single correlation in Equation 2.60 does a good job of predicting Δθ as the intake temperature and/or fueling rate is changed. This variable Δθ expression is therefore a significant addition to the control model in that it will allow for more accurate prediction of peak pressure and CA50, which are dependant upon both the combustion timing and duration.

In order to further validate the use of this variable Δθ correlation, it was included in the model and compared against the case where Δθ was held constant. The simulation was therefore run separately using a constant and variable Δθ in order to observe the effects on the model's performance. The model outputs were compared against experimental CA50 values, and the results can be seen below in Figures 2.22 and 2.23.

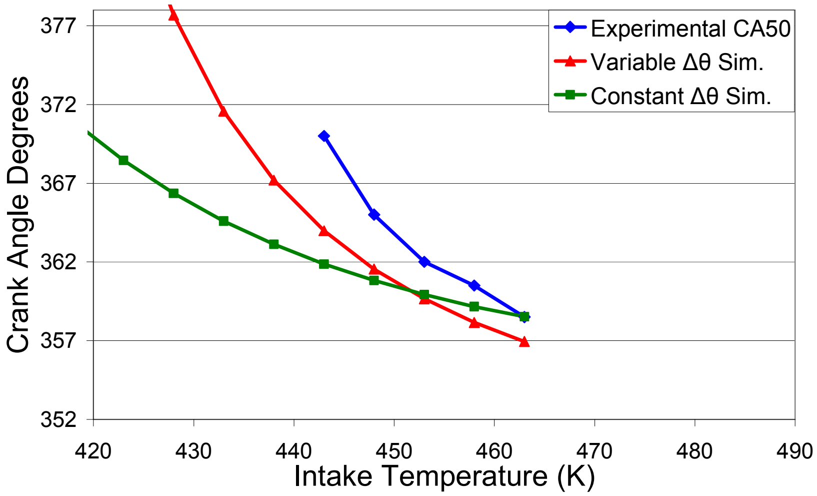

Figure 2.22: Simulation run with variable and constant Δθ for the fueling rate of 9 grams/minute

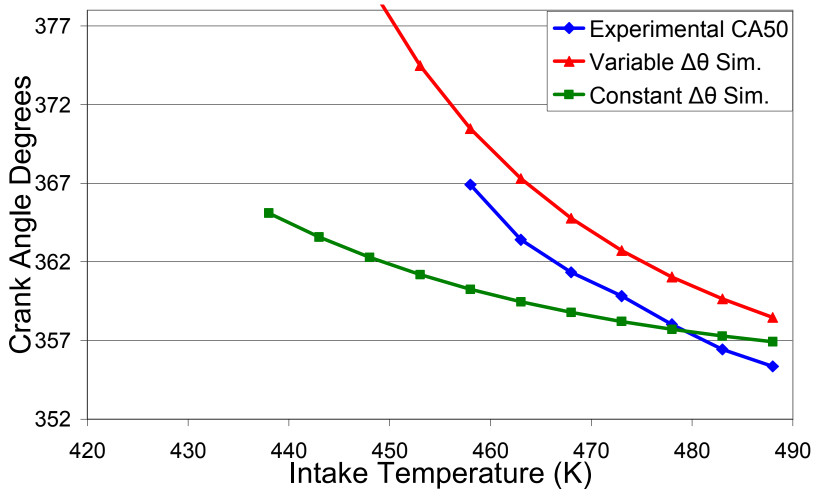

Figure 2.23: Simulation run with variable and constant Δθ for the fueling rate of 6 grams/minute

Figures 2.22 and 2.23 show that the variable Δθ correlation indeed has a significant impact on the performance of the model. When Δθ is held constant, the model is fairly accurate around the point where that Δθ is chosen, but becomes less accurate as the engine moves away from that set point. When Δθ is allowed to vary, however, it is evident that the model is able to track the experimental CA50 values much better as the set point is changed. This improved accuracy, along with the relative simplicity of the correlation developed, therefore supplies justification for inclusion of this correlation within the control model being developed.

2.7 ARRHENIUS RATE THRESHOLD AS A FUNCTION OF FUEL ONLY

The ability of the chosen Integrated Arrhenius Rate combustion timing model to accurately predict the start of combustion relies on the Arrhenius parameters, as well as the threshold value. While the Arrhenius parameters are given for a type of fuel, the threshold value must be calculated using experimental start of combustion data via Equation 2.54. Throughout the process of choosing a combustion timing model, this threshold value was determined using a single experimental data point corresponding to the most advanced combustion timing. Once the Integrated Arrhenius Rate model was chosen, however, the threshold value required a closer examination due to its direct effect on the model's ability to predict SOC. Physically, the Arrhenius Rate expression itself is a global reaction rate which represents the destruction rate of fuel. In order to account for this reaction taking place within an engine, it was divided by the engine speed and then integrated over the part of the engine cycle where the most significant reactions were occurring, i.e. the compression stroke. This resulted in a lower limit of integration that corresponded to IVC and an upper limit corresponding to SOC. The overall process of integrating this global Arrhenius rate expression between these limits resulted in a value which could be physically interpreted as the amount of fuel which had been destroyed at SOC. This meant that the Arrhenius Rate threshold value could be interpreted similarly as the concentration of fuel destroyed at SOC for a given experimental set point. In order to obtain a better understanding of how this threshold varied with set point, it was re-calculated at several different experimental data points. The same procedure was also carried out at a different fueling rate in order to observe the effects of equivalence ratio on the aforementioned threshold value. The results of this analysis can be found in Figures 2.24 and 2.25.

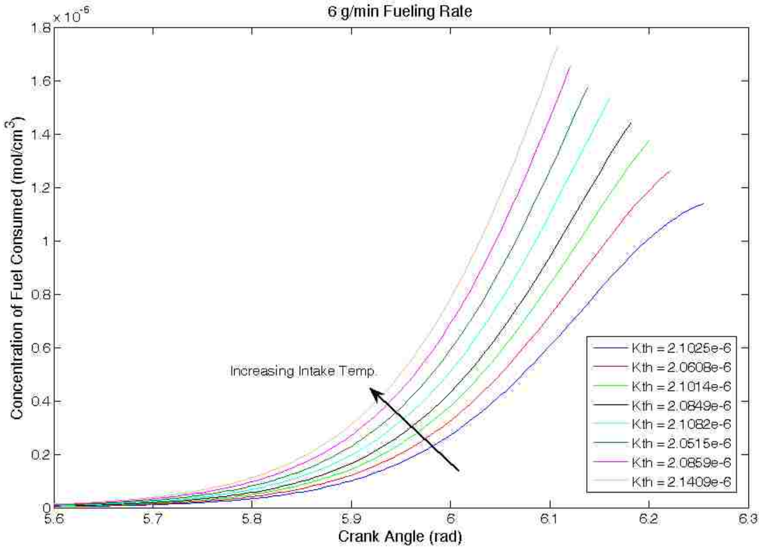

Figure 2.24: Arrhenius Rate Integrand for a Fueling Rate of 6 g/min

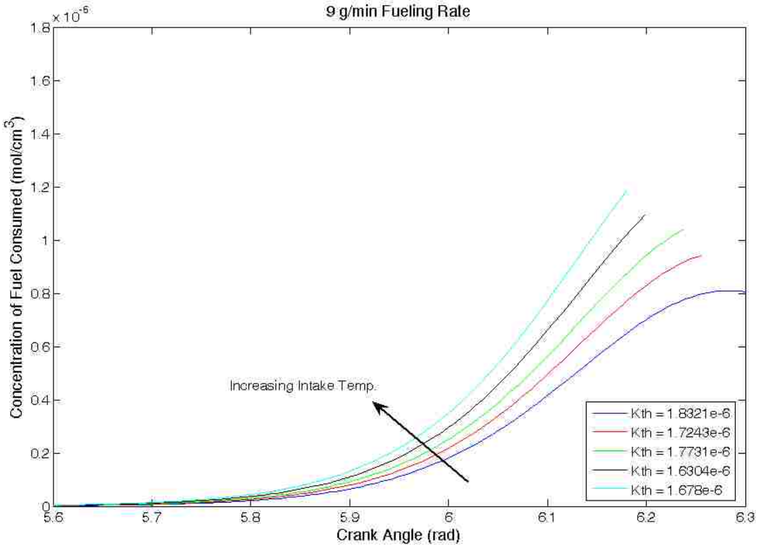

Figure 2.25: Arrhenius Rate Integrand for a Fueling Rate of 9 g/min

These figures displayed the behavior of the Arrhenius Rate integrand as the intake temperature is varied between experimental set point for two different fueling rates. The legend in each figure displayed the threshold values corresponding to each set point, which were again determined using Matlab's quadl integration function. Figure 2.24 showed that the threshold value, for the fueling rate of 6 g/min, remained fairly constant regardless of which experimental data point it was evaluated at. When the fueling rate was increased to 9 g/min, Figure 2.25 showed that the integrated threshold value was slightly lower, but again remained fairly constant regardless of the data point used. The apparent change in threshold magnitude observed between fueling rates was approximately twelve percent, which was well within the realm of experimental uncertainty, and therefore not necessarily representative of the change in fueling rate. These results suggest that the threshold value for a given fuel was insensitive to changes in both the intake temperature and the fueling rate. Therefore, it was concluded that the integrated threshold value remained constant for a particular fuel, and could be determined using any experimental data point available.

2.8 CONTROL MODEL OUTPUTS

2.8.1 Angle of Constant Volume Combustion – θ_{23}. Due to the fact that the combustion process is one of the most complex parts of an HCCI engine cycle, the majority of the assumptions in the model were therefore related to the chosen combustion timing model. As described previously, the combustion timing model was chosen to be the Integrated Arrhenius Rate, and the simplified equation using concentrations and temperature evaluated at TDC can be seen below.

$$F_{des} = \int_{IVC}^{SOC} \left(\frac{A \exp\left(-E_a \big/ R_u T_{TDC} \right) [fuel]^a{}_{TDC} [O_2]^b{}_{TDC}}{\omega} \right) d\theta \qquad (2.61)$$

The justification for this simplification can be found in Section 2.5.5.3. Once the pre-defined threshold value representing the concentration of fuel which must be destroyed before combustion can begin, F_{des}, was reached, the combustion process was assumed to initiate and to proceed as a function of crank angle. The crank angle where fifty percent of the mass is destroyed, θ_{23}, could then be related to the crank angle at which the threshold is crossed, SOC, by SOC = $\theta_{23} - \Delta\theta$. The $\Delta\theta$ term in this expression has been previously defined in Section 2.6, and represents the fact that the combustion event is not entirely instantaneous. Applying this assumption to the integral in Equation 2.61 yielded:

$$F_{des} = \int_{IVC}^{\theta_{23} - \Delta\theta} \left(\frac{A \exp\left(-E_a \big/ R_u T_{TDC} \right) [fuel]^a{}_{TDC} [O_2]^b{}_{TDC}}{\omega} \right) d\theta \qquad (2.62)$$

This expression successfully captures the dependence of the combustion phasing on both the reactant concentrations and temperature. Since both of the concentration terms and the temperature had been evaluated at TDC, the integrand in Equation 2.62 had been reduced to a mere constant that could be pulled out of the integral. Upon doing this, the expression in Equation 2.62 reduced to:

$$F_{des} = \left(\frac{A\exp\left(-E_a \big/ R_u T_{TDC}\right)\left[C_7H_{16}\right]^a{}_{TDC}\left[O_2\right]^b{}_{TDC}\left(\theta_{23} - \Delta\theta - IVC\right)}{\omega} \right) \tag{2.63}$$

The value of the Integrated Arrhenius Rate threshold in Equation 2.63 was evaluated using experimental combustion timing results as described previously in Section 2.5.5.3.

In order to utilize state-space methods for control, the expression in Equation 2.63 had to be reformulated so that it was a function of only the inputs and state variables. To accomplish this, the in-cylinder temperature at TDC could be written as:

$$T_{TDC} = \left(\frac{V_{1,k}}{V_{TDC}} \right)^{\gamma - 1} T_{1,k} \tag{2.64}$$

The reactant concentrations at TDC could be derived from Equation 2.14 on a molar basis as:

$$\left[C_7H_{16}\right]_{TDC,k} = \frac{\phi_{k-1} N_{F,k}}{V_{TDC}} \qquad \left[O_2\right]_{TDC,k} = \frac{11\left(\alpha_{i,k}\left(1 - \phi_{k-2}\right) + 1\right)N_{F,k}}{V_{TDC}} \tag{2.65}$$

Applying the ideal gas law at IVC results in:

$$N_{F,k} = \frac{P_1 V_1}{R_u T_{1,k}\left[\alpha_{i,k}\left(4\phi_{k-2} + 52.36\right) + \left(\phi_{k-1} + 52.36\right)\left(1 + \alpha_{e,k-1}\right)\right]} \tag{2.66}$$

Substituting Equations 2.64-2.66 into Equation 2.63 applied to the kth engine cycle results in the following expression.

$$F_{des} = \frac{A\exp\left(\dfrac{-E_a}{R_u\left(\dfrac{V_{1,k+1}}{V_{TDC}}\right)^{\gamma-1} T_{1,k+1}}\right)\left[\dfrac{\phi_{k-1}P_1V_1}{R_uT_{1,k}\left[\alpha_{i,k}(4\phi_{k-2}+52.36)+(\phi_{k-1}+52.36)(1+\alpha_{e,k-1})\right]}\right]^a\left[\dfrac{11(\alpha_{i,k}(1-\phi_{k-2})+1)P_1V_1}{R_uT_{1,k}\left[\alpha_{i,k}(4\phi_{k-2}+52.36)+(\phi_{k-1}+52.36)(1+\alpha_{e,k-1})\right]}\right]^b(\theta_{23}-\Delta\theta-IVC)}{\omega} \tag{2.67}$$

Rearranging Equation 2.67 yields the following expression for θ_{23}:

$$\theta_{23,k} = \frac{\left(\dfrac{F_{des}\omega}{A\phi_{k-1}{}^{a}\left[11(\alpha_{i,k}(1-\phi_{k-2})+1)\right]^b}\right)\left(\dfrac{V_{TDC}R_u}{P_1}\right)^{a+b}\left(\dfrac{T_{1,k}\left[\alpha_{i,k}(4\phi_{k-2}+52.36)+(\phi_{k-1}+52.36)(1+\alpha_{e,k-1})\right]}{V_1}\right)^{a+b}}{\exp\left(\dfrac{-E_a}{R_u\left(\dfrac{V_{1,k+1}}{V_{TDC}}\right)^{\gamma-1} T_{1,k+1}}\right)} + \Delta\theta_k + IVC + \theta_{offset} \tag{2.68}$$

Equation 2.68 is a powerful expression, in that it relates the output θ_{23} to the system inputs (intake temperature, equivalence ratio and external EGR fraction) as well as the system states (temperature at the start of compression and residual fraction). This expression is therefore written in state space form, and represents an output equation for the control model.

2.8.2 Peak Pressure. Since peak pressure was also defined as an output from the control model, it must also be defined entirely in terms of both the inputs and state variables of the system. To this end, plugging Equations 2.11 and 2.18 into Equation 2.22 results in a nonlinear dynamic expression for the peak in-cylinder pressure.

$$P_{3,k} = \frac{N_{3,k}}{N_{2,k}}P_{atm}\left(\frac{V_1}{V_{23,k}}\right)\frac{c_{3,k-1}+\left(c_{1,k-1}+c_{2,k-1}\alpha_{i,k}+c_{egr,k-1}\alpha_{e,k-1}-R_uN_{2,k}\right)\left(\dfrac{V_1}{V_{23,k}}\right)^{\gamma-1}T_{1,k}-\left(c_{1,k-1}-c_{4,k-1}\right)T_{ref}}{\left(c_{2,k-1}\alpha_{i,k}+c_{egr,k-1}\alpha_{e,k-1}+c_{4,k-1}-R_uN_{3,k}\right)T_{1,k}} \tag{2.69}$$

Equation 2.69 is another powerful expression which relates the peak pressure, P_3, to the model inputs and state variables, thus making it another output equation. Note the dependence on the combustion timing through the V_{23} term, which represents the volume at which the constant volume combustion is occurring.

2.8.3 Pressure Rise Rate. Due to the fact that HCCI combustion involves a nearly instantaneous ignition of a homogenous mixture, there is an inherent risk of extremely violent combustion if the ignition timing becomes too advanced. Under these conditions, large amounts of energy are released during the upward motion of the compression stroke, which oppose the motion of the piston and therefore result in excessively high pressure rise rates. Since HCCI combustion is a lean strategy, high levels of noise, rather than engine damage, are generally the issue due to relatively low combustion temperatures. For this reason, a pressure rise rate threshold is generally established in an attempt to keep the combustion noise from becoming excessive. A generally accepted value for this rate of pressure rise is typically around 10 bar/CAD [17]. In order to incorporate this into the model, a simple correlation was developed which was based on the peak pressure, P_3, along with the combustion duration term $\Delta\theta$.

$$PRR_k = \frac{\left(P_{3,k} - P_{SOC,k}\right)}{\Delta\theta_k} \tag{2.70}$$

This expression approximates the pressure rise rate as the pressure rise due to combustion normalized by the time it took for that combustion event to occur. Plugging Equations 2.12, 2.60 and 2.69 into Equation 2.70 yields:

$$PRR_k = \frac{\dfrac{N_{3,k}}{N_{2,k}} P_{atm} \left(\dfrac{V_1}{V_{23,k}} \right)^{\dfrac{c_{3,k-1} + \left(c_{1,k-1} + c_{2,k-1}\alpha_{i,k} + c_{egr,k-1}\alpha_{e,k-1} - R_u N_{2,k} \right) \left(\dfrac{V_1}{V_{23,k}} \right)^{\gamma-1} T_{1,k} - \left(c_{1,k-1} - c_{4,k-1} \right) T_{ref}}{\left(c_{2,k-1}\alpha_{i,k} + c_{egr,k-1}\alpha_{e,k-1} + c_{4,k-1} - R_u N_{3,k} \right) T_{1,k}}} - P_{SOC,k}}{2.0677 \times 10^{-18} \left(0.00003515 \right)^{\phi_{k-1}} \left(0.99296 \right)^{\left(V_1 / V_{SOC,k} \right) T_{1,k}} \left(1.1609 \right)^{SOC,k}} \tag{2.71}$$

Equation 2.71 gives an expression for the pressure rise rate which is written entirely in terms of inputs and state variables, and is therefore another output equation for the control model.

2.8.4 Gross Indicated Work.

While peak pressure values give a rough estimate of what the engine is outputting, a more direct indicator of engine performance is the work output from the engine. In practice, the engine must meet certain power requirements set by the operator, which demand a certain amount of work output from the engine. Due to its importance, the work output from the engine was therefore chosen to be yet another output from the model.

In order to develop a relatively simplistic expression for this output, the gross indicated work (W_{ig}) was therefore chosen to represent the overall work output from the engine. This is a reasonable assumption due to the fact that this gross work term accounted for the work done during both the compression and expansion strokes, which comprised the large majority of work done during each cycle. A detailed P-V diagram is provided in Figure 2.26, which displays the compression, expansion and gross indicated work for a given cycle.

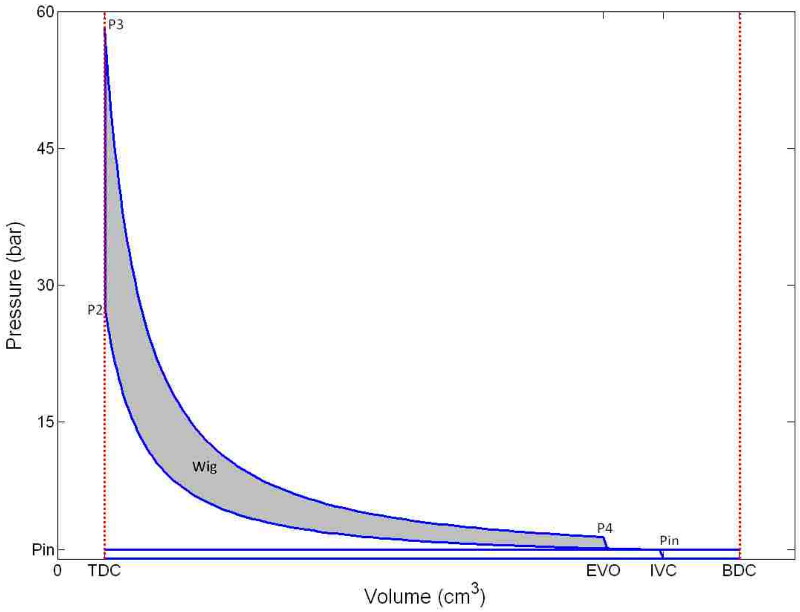

Figure 2.26: Pressure-volume diagram for generic HCCI engine cycle

Figure 2.26 displays the pressure-volume history of a typical HCCI engine cycle run on the Hatz engine. The work for this engine cycle can be approximated using the following expression:

$$W = \int_{V_1}^{V_2} PdV \tag{2.72}$$

In order to determine the gross indicated work, the compression and expansion processes from Figure 2.26 were both assumed to be polytropic. This meant that both processes could be described analytically by:

$$PV^n = \text{Constant} \tag{2.73}$$

Assuming that the intake charge is at atmospheric pressure, and that the polytropic exponent (n) is equal to the ratio of specific heats (γ), Equation 2.73 could be plugged into Equation 2.72 to determine the compression work. Integrating from V_4 to V_{23}:

$$W_{comp,k} = \frac{P_2 V_{23} - 0.01157 V_4}{1-\gamma} \tag{2.74}$$

Due to the valve timing, Figure 2.26 displayed that there is a small amount of additional compression work which occurs between IVC and EVO. Assuming atmospheric intake pressure, Equation 2.73 can again be plugged into Equation 2.72 and integrated to determine the work.

$$W_{comp2,k} = \frac{0.01157 V_4 - P_{in} V_1 + P_{in}(1-\gamma)(V_1 - V_4)}{1-\gamma} \tag{2.75}$$

Assuming a blowdown to atmospheric pressure, Equation 2.73 was again plugged into Equation 2.72 in order to determine the expansion work. Integrating from V_{23} to V_4 yields:

$$W_{\exp,k} = \frac{P_4 V_4 - P_3 V_{23}}{1-\gamma} \tag{2.76}$$

Combining Equations 2.74, 2.75 and 2.76 yields the following expression for the gross indicated work.

$$W_{ig,k} = \frac{P_4 V_4 - P_3 V_{23} + P_2 V_{23} - 0.01157 V_4}{1-\gamma} + \frac{0.01157 V_4 - P_{in} V_1 + P_{in}(1-\gamma)(V_1 - V_4)}{1-\gamma} \tag{2.77}$$

Plugging Equations 2.11, 2.12, 2.18, 2.22 and 2.24 into Equation 2.77 yields the output equation for the gross indicated work which was used in the control model.

$$W_{ig,k} = \frac{\left[V_4\left(\frac{V_{23,k}}{V_4}\right)^{\gamma} - V_{23,k}\right]\left[\frac{N_{3,k}}{N_{2,k}}\,\mathrm{d}\,P_{in}\left(\frac{V_1}{V_{23,k}}\right)\right] + P_{in}\left[\left(\frac{V_1}{V_{23,k}}\right)^{\gamma} V_{23,k} - V_1 + (1-\gamma)(V_1 - V_4)\right]\left[\left(c_{2,k-1}\alpha_{i,k} + c_{egr,k-1}\alpha_{e,k-1} + c_{4,k-1} - R_u N_{3,k}\right)T_{1,k}\right]}{\left(c_{2,k-1}\alpha_{i,k} + c_{egr,k-1}\alpha_{e,k-1} + c_{4,k-1} - R_u N_{3,k}\right)T_{1,k}(1-\gamma)}$$

$$\text{where d} = c_{3,k-1} + \left(c_{1,k-1} + c_{2,k-1}\alpha_{i,k} + c_{egr,k-1}\alpha_{e,k-1} - R_u N_{2,k}\right)\left(\frac{V_1}{V_{23,k}}\right)^{\gamma-1} T_{1,k} - \left(c_{1,k-1} - c_{4,k-1}\right)T_{ref} \tag{2.78}$$

Equation 2.78 gives an expression for the gross indicated work which is written entirely in terms of inputs and state variables, and is therefore another output equation for the control model.

2.8.5 Efficiency. In addition to the work output from the engine, it was also desired to have an additional parameter which gave an indication of how efficient the engine was operating at a given engine setpoint. To accomplish this, an efficiency term was introduced which was based on the amount of work output from the engine normalized by the amount of fuel energy input.

$$\eta = \frac{W_{ig,k}}{N_{f,k} LHV_f} \tag{2.79}$$

In order to define this output entirely in terms of system inputs and state variables, Equation 2.78 was plugged into Equation 2.79 to yield:

$$\eta_k = \frac{\left[V_4\left(\frac{V_{23,k}}{V_4}\right)^{\gamma} - V_{23,k}\right]\left[\frac{N_{3,k}}{N_{2,k}}\,\mathrm{d}\,P_{in}\left(\frac{V_1}{V_{23,k}}\right)\right] + P_{in}\left[\left(\frac{V_1}{V_{23,k}}\right)^{\gamma} V_{23,k} - V_1 + (1-\gamma)(V_1 - V_4)\right]\left[\left(c_{2,k-1}\alpha_{i,k} + c_{egr,k-1}\alpha_{e,k-1} + c_{4,k-1} - R_u N_{3,k}\right)T_{1,k}\right]}{\left(c_{2,k-1}\alpha_{i,k} + c_{egr,k-1}\alpha_{e,k-1} + c_{4,k-1} - R_u N_{3,k}\right)T_{1,k}(1-\gamma)(100)N_{f,k}LHV_{C7H16}}$$

$$\text{where } \mathrm{d} = c_{3,k-1} + \left(c_{1,k-1} + c_{2,k-1}\alpha_{i,k} + c_{egr,k-1}\alpha_{e,k-1} - R_u N_{2,k}\right)\left(\frac{V_1}{V_{23,k}}\right)^{\gamma-1} T_{1,k} - \left(c_{1,k-1} - c_{4,k-1}\right)T_{ref} \tag{2.80}$$

Equation 2.80 is another powerful expression which now relates the efficiency, η, to the model inputs and state variables, thus making it another output equation.

2.9 STATE UPDATE EQUATIONS

State-space methods for control require that the outputs be written entirely in terms of both the inputs and the state variables of the system. As a result, these methods also require the state variables in one cycle to be entirely dependent upon the inputs and state variables of the previous cycle. These expressions are known as state update equations, and are what allows the controller to "predict" what will happen in a future cycle, and then choose an appropriate control input for the given conditions. The state variables of the current system, which have been previously defined, have already been formulated and presented in Equations 2.10, 2.27 and 2.63. These expressions are still a step removed from application to control, however, since they are written in terms of the five state thermodynamic cycle. In order to bridge the gap, these expressions must therefore be reformulated so that they are functions of only the inputs and state variables.

The first state variable investigated in this respect is α_i, which represents the trapped residual which is carried over from cycle to cycle. In order to develop an update equation for this parameter, the expression in Equation 2.27 must be redeveloped. There are several intermediate variables which are functions of engine geometry that can be evaluated in order to simplify this expression. The geometry of the single cylinder CI engine being modeled was used to this end, and the corresponding values can be seen in Table 2.1. In addition to geometry considerations, Equation 2.27 is also dependent on the difference between intake and exhaust pressure. Since both pressures are assumed to be atmospheric in the current model, values for these pressures are taken from averaged experimental data in order to preserve the accuracy of the residual calculation. Under these conditions, Equations 2.11, 2.18, 2.22, 2.23, 2.24, and 2.25 can be sequentially plugged into Equation 2.27 in order to arrive at the state update equation for the residual. This expression can be seen in Equation 2.81.

$$\alpha_{i,k+1} = \frac{0.0912558432\ 97\, T_{in,k}}{\left[\dfrac{\left(c_{2,k-1}\alpha_{i,k} + c_{egr,k-1}\alpha_{e,k-1} + c_{4,k-1} - R_u N_{3,k}\right)T_{1,k}}{\dfrac{N_{3,k}}{N_{2,k}}\, d \left(\dfrac{V_1}{V_{23,k}}\right)}\right]^{\gamma-1/\gamma} \left[\dfrac{d}{c_{2,k-1}\alpha_{i,k} + c_{egr,k-1}\alpha_{e,k-1} + c_{4,k-1} - R_u N_{3,k}}\right]}$$

$$where\ d = \left(c_{3,k-1} + \left(c_{1,k-1} + c_{2,k-1}\alpha_{i,k} + c_{egr,k-1}\alpha_{e,k-1} - R_u N_{2,k}\right)\left(\frac{V_1}{V_{23,k}}\right)^{\gamma-1} T_{1,k} - \left(c_{1,k-1} - c_{4,k-1}\right)T_{ref} \right) \tag{2.81}$$

The second state variable investigated is the temperature at the start of compression, T_1. Plugging Equations 2.11, 2.18, 2.22, 2.23, 2.24, and 2.25 into the expression previously developed in Equation 2.10 yields the second of these state update equations. This newly developed expression can be seen in Equation 2.82, where $\alpha_{i,k+1}$ is replaced with the expression in Equation 2.81. The result is an update equation for T_1 which is a function of only inputs and state variables from previous cycles.

$$T_{1,k+1} = \frac{c_{1,k}T_{in,k} + c_{egr,k}\alpha_{e,k}T_{egr} + c_{2,k}\alpha_{i,k+1}\xi\left[\dfrac{\left(c_{2,k-1}\alpha_{i,k} + c_{egr,k-1}\alpha_{e,k-1} + c_{4,k-1} - R_u N_{3,k}\right)T_{1,k}}{\dfrac{N_{3,k}}{N_{2,k}}d\left(\dfrac{V_1}{V_{23,k}}\right)}\right]^{\gamma-1/\gamma}\left[\dfrac{d}{c_{2,k-1}\alpha_{i,k} + c_{egr,k-1}\alpha_{e,k-1} + c_{4,k-1} - R_u N_{3,k}}\right]}{c_{1,k} + c_{2,k}\alpha_{i,k+1} + c_{egr,k}\alpha_{e,k}} \tag{2.82}$$

The final state variable represented the angle of peak pressure within the cycle. The output equation in Equation 2.68 can be used to develop the necessary update equation for this parameter. Plugging Equations 2.81 and 2.82 back into Equation 2.68 results in an expression for θ_{23}, which is entirely in terms of inputs and states from the previous cycle. This expression can be seen in Equation 2.83, where $\alpha_{i,k+1}$ is again replaced with the expression in Equation 2.81, $T_{1,k+1}$ is replaced with the expression in Equation 2.82, and $\Delta\theta$ is again replaced with the expression in Equation 2.60.

$$\theta_{23,k+1} = \frac{\left(\dfrac{F_{des}\,\omega}{A\,\phi_k^{\,a}\left[11\left(\alpha_{i,k+1}\left(1-\phi_{k-1}\right)+1\right)\right]^{b}}\right)\left(\dfrac{V_{TDC}R_u}{P_{atm}}\right)^{a+b}\left(\dfrac{\left[\alpha_{i,k+1}\left(4\phi_{k-1}+52.36\right)+\left(\phi_k+52.36\right)\left(1+\alpha_{e,k}\right)\right]T_{1,k+1}}{V_1}\right)^{a+b}}{\exp\left[\dfrac{-E_a}{\left(\dfrac{V_1}{V_{TDC}}\right)^{\gamma-1}T_{1,k+1}}\right]} + \Delta\theta_{k+1} + \theta_{IVC} + \theta_{offset} \tag{2.83}$$

Since this nonlinear model was developed from a controls perspective, these output and state update equations have been formulated such that they are directly applicable to nonlinear state-space control techniques. While linearization is a popular technique often used to simplify nonlinear representations of a physical system such as this one, there are several disadvantages associated with it. Since linearization requires the model to be evaluated at some engine operating point, it therefore has an inherently limited operating range. This is not desirable for control of HCCI engines, which regularly change engine set point and have the ability to operate on several different types of fuels. This ability to change fuels complicates the controller design even further in that it requires that the model be linearized individually for each fuel. Linearization can also eliminate certain unknown, yet important, nonlinearities in the system dynamics when the set point or fuel is changed on the engine. By retaining the nonlinear elements in the model, many of these shortcomings associated with linearization can be eliminated. The operating range of the HCCI engine can be extended, and the various nonlinearities within the system dynamics can be preserved. While retaining these nonlinearities has its advantages, it also results in a highly complex nonlinear system. While controller development for such a complex nonlinear system is generally difficult, techniques developed by the authors in [33] can be successfully used to implement nonlinear control strategies.

3. CONTROL MODEL VALIDATION

3.1 BASE STOICHIOMETRY DETERMINATION

The stoichiometry of the model was originally developed using isooctane as the fuel, which was chosen due to its similar chemistry to the Unleaded Test Gasoline used in the experiment. The model was run using this stoichiometry, and the results were shown to agree well with the experimental data when compared with one another. Despite this fairly good agreement, however, many people would argue that a fuel with a chemistry more similar to heptane, rather than isooctane, should have been used to develop the stoichiometry within the model. This arises from the idea that heptane (C_7H_{16}) is more chemically similar (C/H, molecular weight, etc.) to an Unleaded Test Gasoline than isooctane (C_8H_{18}). In an effort to be complete, the model stoichiometry was therefore redeveloped using a fuel with a H/C ratio of 7/16 in order to investigate whether or not the performance of the model was indeed enhanced. The resulting model was identical to the one developed using isooctane, with the only exception being the stoichiometric coefficients from the combustion reaction. For the case of the new fuel, the stoichiometric reaction becomes

$$\phi C_7H_{16} + 11(O_2 + 3.76N_2) \rightarrow 7\phi CO_2 + 8\phi H_2O + 41.36N_2 + 11(1-\phi)O_2 \tag{3.1}$$

Now add the products and EGR to Equation 2.84 in order to get an expression for the coupled cycle.

$$\begin{aligned}&\phi C_7H_{16} + 11(\alpha_{i,k+1}(1-\phi_{k-1})+1)O_2 + (41.36(1+\alpha_{i,k+1})+\alpha_{e,k}(\phi_k + 52.36))N_2 + \\ &7\phi_{k-1}\alpha_{i,k+1}CO_2 + 8\phi_{k-1}\alpha_{i,k+1}H_2O\end{aligned} \tag{3.2}$$

As mentioned previously, the expression in Equation 3.2 is written in an identical form to the isooctane case, with the only difference being the fuel and the resulting coefficients. This implies that the overall structure of the model will remain the same, and that the coefficients need only be changed when redeveloping the stoichiometry. In light of this, the necessary coefficients were updated within the model to reflect those of C_7H_{16}. Once updated, the model was run using a fueling rate of 9 grams/minute, and the results were compared against those obtained from the experiment using an Unleaded Test Gasoline. The results of this analysis can be seen in Figures 3.1-3.3.

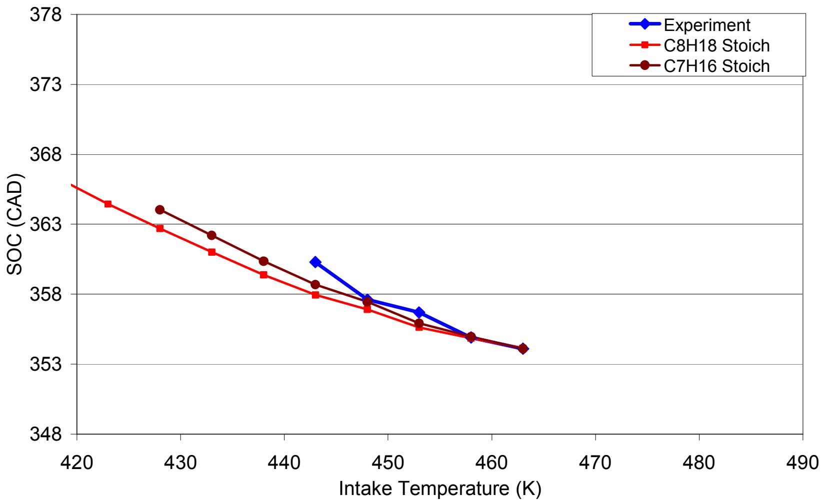

Figure 3.1: SOC tracking versus experimental UTG96 using C_8H_{18} and C_7H_{16} stoichiometries for the fueling rate of 9 grams/minute

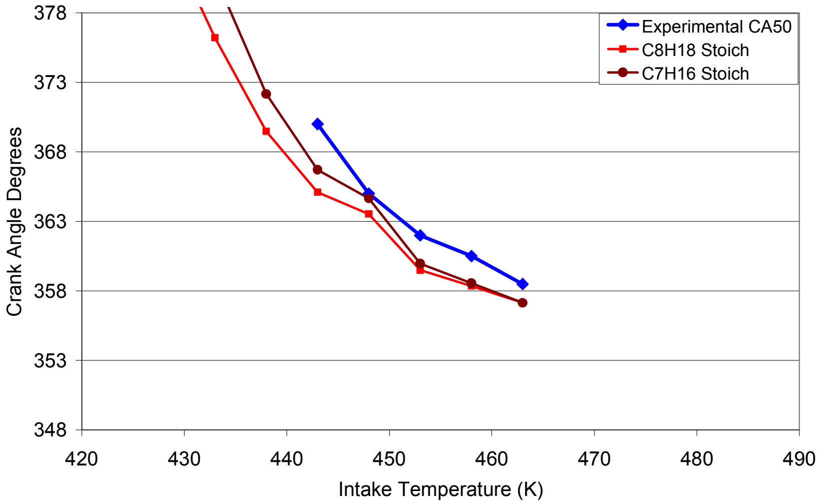

Figure 3.2: Model θ_{23} versus experimental UTG96 CA50 using C_8H_{18} and C_7H_{16} stoichiometries for the fueling rate of 9 grams/minute

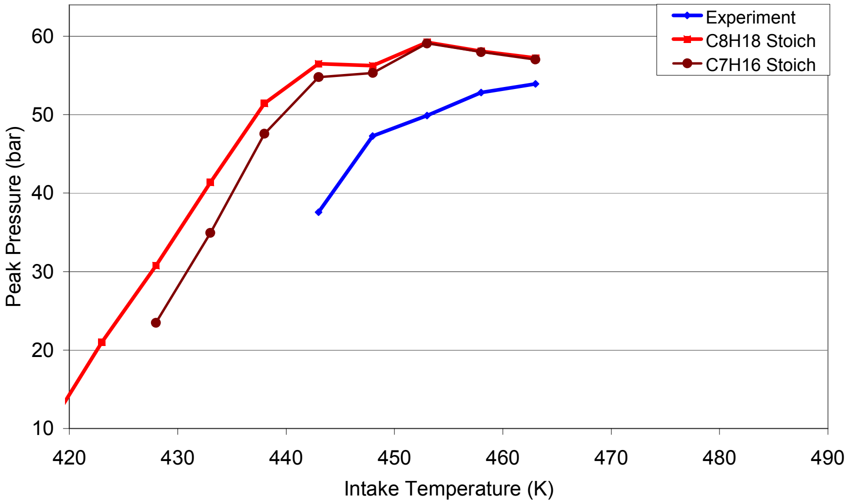

Figure 3.3: Model peak pressure versus experimental UTG96 using C_8H_{18} and C_7H_{16} stoichiometries for the fueling rate of 9 grams/minute

Figures 3.1-3.3 display model results from both isooctane and C_7H_{16} stoichiometries. From these figures, it is apparent that modeling the stoichiometry using C_7H_{16}, rather than isooctane, does indeed improve the performance of the overall model. Figure 3.1 shows that start of combustion values predicted by the model get closer to the experimental values for UTG96. In addition, Figures 3.2 and 3.3 show that the model is also able to more accurately track both the experimental CA50 as well as the peak pressure. An explanation for this improved model performance is that the fuel used to develop the stoichiometry within the model, C_7H_{16} in this case, was indeed more chemically similar to the Unleaded Test Gasoline than isooctane. Since the fuel was modeled more accurately, the model was therefore able to do a better job of predicting the experimental trends. These results seem to suggest that the stoichiometry within the model should be developed using C_7H_{16} in order to increase its accuracy. Prior to making this adjustment, however, it is necessary to verify these results at a different engine setpoint.

In order to ensure that C_7H_{16} stoichiometry was indeed superior to that of isooctane, the model was run using a different fueling rate in order to obtain results at a different setpoint. The fueling rate was set to 6 grams/minute in the model, and the results were once again compared to those obtained from the experiment for UTG96. The results of this comparison can be seen in Figures 3.4-3.6.

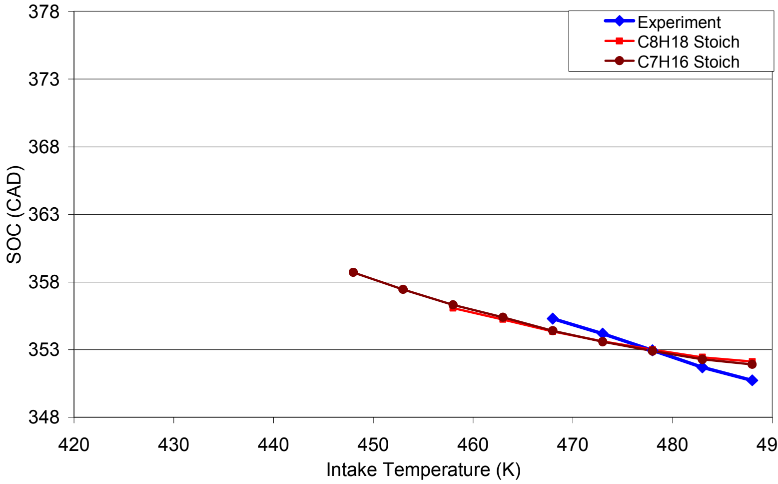

Figure 3.4: SOC tracking versus experimental UTG96 using C_8H_{18} and C_7H_{16} stoichiometries for the fueling rate of 6 grams/minute

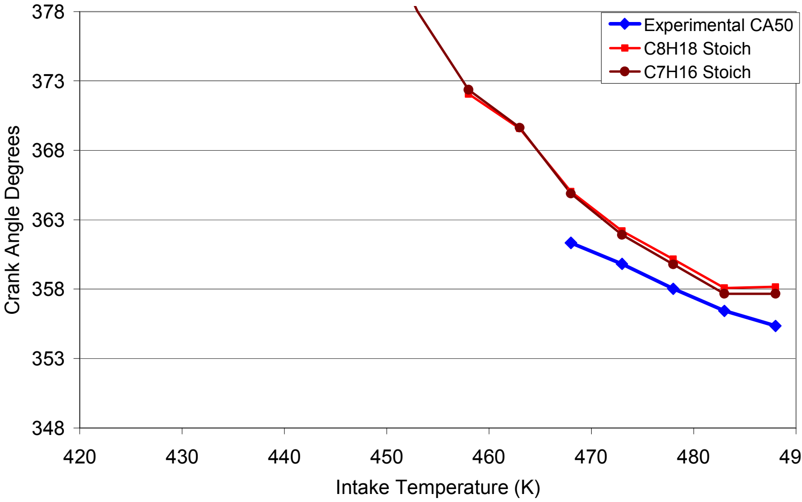

Figure 3.5: Model θ_{23} versus experimental UTG96 CA50 using C_8H_{18} and C_7H_{16} stoichiometries for the fueling rate of 6 grams/minute

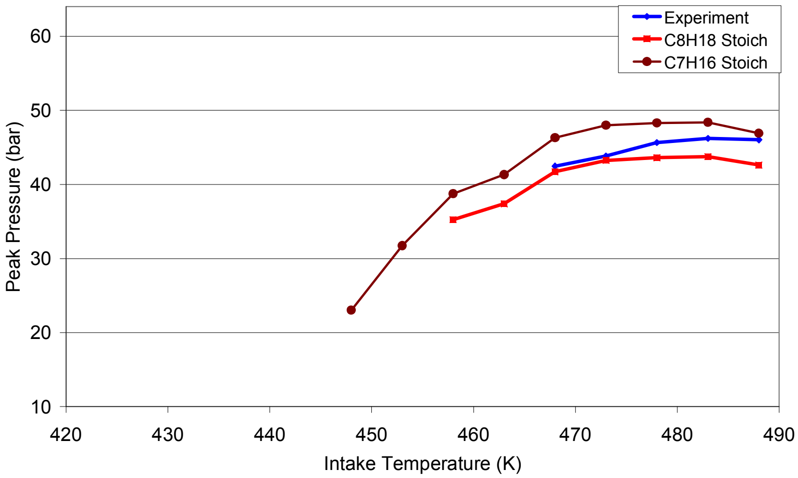

Figure 3.6: Model peak pressure versus experimental UTG96 using C_8H_{18} and C_7H_{16} stoichiometries for the fueling rate of 6 grams/minute

Figures 3.4-3.6 once again display results for both isooctane and C_7H_{16} stoichiometries in order to directly compare the two cases. These figures reveal that using the C_7H_{16}-derived stoichiometry once again results in slightly improved model performance when compared to the experimental UTG96 data, this time for the fueling rate of 6 grams/minute. Due to the fact that C_7H_{16} stoichiometry improves model performance at two entirely different setpoints, it can therefore be implemented more confidently as a means to improve the accuracy of the model. For these reasons, C_7H_{16} was chosen to model the stoichiometry within the model. It is also important to note that, while the C_7H_{16} stoichiometry seemed to enhance the performance of the model, the effect was somewhat minor.

3.2 C_7H_{16}: 9 G/MIN FUELING RATE

Now that these assumptions have been made to the combustion timing model, the next step is to ensure that they are not adversely affecting the fidelity of the control model. The easiest way to check the accuracy of these simplified equations is to simply compare the results of the model to those from the experiment. In order to benchmark the model with the experiment, the intake temperature was varied while all other parameters were held constant. This forced any changes in the outputs from the model to be directly related to the temperature of the intake. This procedure was carried out, and the available experimental data was compared against the corresponding outputs from the model. The aforementioned experimental data used UTG96 as the fuel, with an equivalence ratio of 0.38 and no external EGR. The results of this benchmarking process were tabulated, and can be found below.

Table 3.1: Integrated Arrhenius Rate: Comparison of Experiment and Simulation I (9gpm)

Intake Temp (K)	$P_{max, exp}$ (bar)	$P_{max, model}$ (bar)	% error	$\theta_{SOC, exp}$ (CAD)	$\theta_{SOC, model}$ (CAD)	% error
463	53.923	57.03	5.76%	354.1	354.0997	0.00%
458	52.84	57.99	9.75%	354.9	354.9651	0.02%
453	49.885	59.09	18.45%	356.7	355.9181	-0.22%
448	47.285	55.31	16.97%	357.6	357.4408	-0.04%
443	37.571	54.78	45.80%	360.3	358.6861	-0.45%
438		47.56			360.3597	
433		34.93			362.1958	
428		23.47			364.0327	

Table 3.2: Integrated Arrhenius Rate: Comparison of Experiment and Simulation II (9gpm)

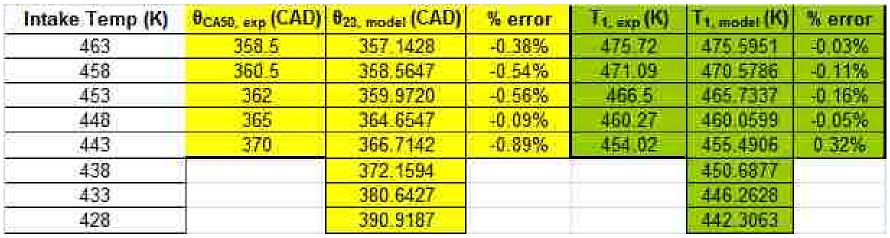

Intake Temp (K)	$\theta_{CA50, exp}$ (CAD)	$\theta_{23, model}$ (CAD)	% error	$T_{1, exp}$ (K)	$T_{1, model}$ (K)	% error
463	358.5	357.1428	-0.38%	475.72	475.5951	-0.03%
458	360.5	358.5647	-0.54%	471.09	470.5786	-0.11%
453	362	359.9720	-0.56%	466.5	465.7337	-0.16%
448	365	364.6547	-0.09%	460.27	460.0599	-0.05%
443	370	366.7142	-0.89%	454.02	455.4906	0.32%
438		372.1594			450.6877	
433		380.6427			446.2628	
428		390.9187			442.3063	

Table 3.3: Integrated Arrhenius Rate: Comparison of Experiment and Simulation III (9gpm)

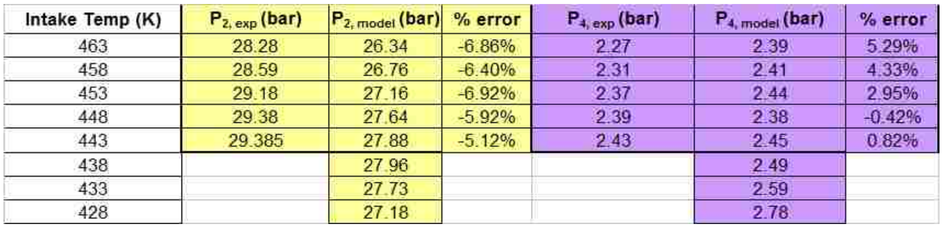

Intake Temp (K)	$P_{2,\,exp}$ (bar)	$P_{2,\,model}$ (bar)	% error	$P_{4,\,exp}$ (bar)	$P_{4,\,model}$ (bar)	% error
463	28.28	26.34	-6.86%	2.27	2.39	5.29%
458	28.59	26.76	-6.40%	2.31	2.41	4.33%
453	29.18	27.16	-6.92%	2.37	2.44	2.95%
448	29.38	27.64	-5.92%	2.39	2.38	-0.42%
443	29.385	27.88	-5.12%	2.43	2.45	0.82%
438		27.96			2.49	
433		27.73			2.59	
428		27.18			2.78	

Table 3.4: Integrated Arrhenius Rate: Comparison of Experiment and Simulation IV (9gpm)

Intake Temp (K)	$T_{3,\,exp}$ (K)	$T_{3,\,model}$ (K)	% error	$T_{ex,\,exp}$ (K)	$T_{5,\,model}$ (K)	% error	PRR_{exp} (bar/CAD)	PRR_{model} (bar/CAD)	% error
463	1604	2068.2	28.94%	520.15	815.3	56.74%	10.54	10.086	-4.31%
458	1533	2063.7	34.62%	521.75	810.4	55.32%	9.29	8.6752	-6.62%
453	1498	2074.5	38.48%	524.38	811.2	54.70%	6.61	7.8753	19.14%
448	1491	1977.3	32.62%	525.23	785	49.46%	4.91	3.8347	-21.90%
443	1312	1997.3	52.23%	529.17	794.7	50.18%	2.13	3.3514	57.34%
438		1939.5			797.3			1.7696	
433		1843.9			814			0.5766	
428		1758.7			850.9			0.3629	

As the intake temperature was decreased, the outputs from the model seemed to agree fairly well with the experiment. While the experimental data stopped at an intake temperature of 443 K, Tables 3.1-3.4 show that the simulation was run for intake temperatures extending down to 428 K. The reason for doing this was to observe the behavior of the model for inputs outside of the experimental range. Since the actual outputs from the control model were prescribed to be the most important, they were therefore the first parameters to be investigated. The first columns of Table 3.1 show the results of the peak pressure comparison. The experimental and simulation results were both plotted on the same axes, and this plot can be seen below in Figure 3.7.

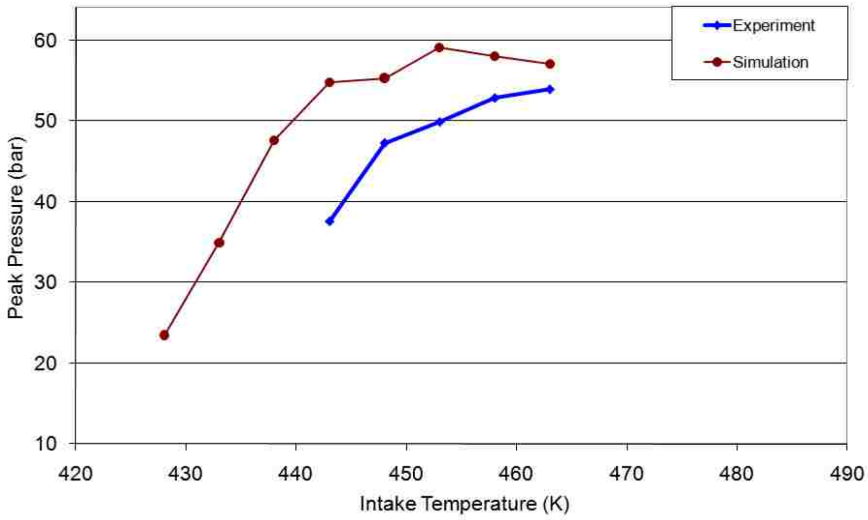

Figure 3.7: Integrated Arrhenius Rate: Peak Pressure Comparison between Experiment and Simulation (9 g/min)

Figure 3.7 shows the behavior of the peak pressure for both the experiment and simulation as the intake temperature is decreased. The most striking difference between the two lines is the fact that the magnitudes are different. This behavior is not surprising, however, due to the simplistic nature of the control model being used. It is unrealistic to expect the simplified control model to precisely predict the experimental values due to the numerous assumptions that were made in developing it. Despite these slight differences in magnitude, the control model does succeed in capturing the overall trend of the experimental peak pressure. The only discrepancy in this trend occurs in the model as the peak pressure approaches the transition point located at top dead center. Table 3.1 shows that the experimental data immediately begins to drop off, while the simulation predicts that the peak pressure first becomes slightly greater before starting to drop off. The correct decreasing trend in peak pressure is indeed captured by the simulation, it is merely delayed. This delay can be explained by looking at the combustion duration term, Δθ, which was added to account for the fact that combustion does not occur instantaneously. For an actual engine, the duration of combustion will typically increase slightly as the start of combustion is retarded. As will be discussed later, while the variable Δθ correlation used in the model was accurately predicting this overall increasing trend, it was slightly under-predicting the magnitudes due to the simplistic nature of the expression being used. Since combustion was taking place near top dead center, this meant that the peak pressure location for the simulation was being held below top dead center for a longer period of time than that of the experiment. This explains why the simulation shows an initial rise in the peak pressure and then begins to fall off. When the peak pressure occurs before top dead center, some additional pressure rise is inevitable due to the contribution from the remainder of the compression stroke. As soon as the simulation pushes the peak pressure location past top dead center, the values begin to drop off similar to those in the experiment due to the contributions of the expansion stroke. Other than the slight delay that occurs around top dead center, Figure 3.7 shows that the control model accurately predicts the correct trend in the peak pressure evolution. Even though the magnitudes are slightly off, correctly predicting this trend is all that is required in order for the control model to be able to effectively control the peak pressure.

The next parameter that was investigated was the angle at which start of combustion occurred. The intake temperature was varied, and the results for the simulation, as well as the experiment, can be found in Table 3.1. These results were also plotted against each other, and this diagram can be found in Figure 3.8 below.

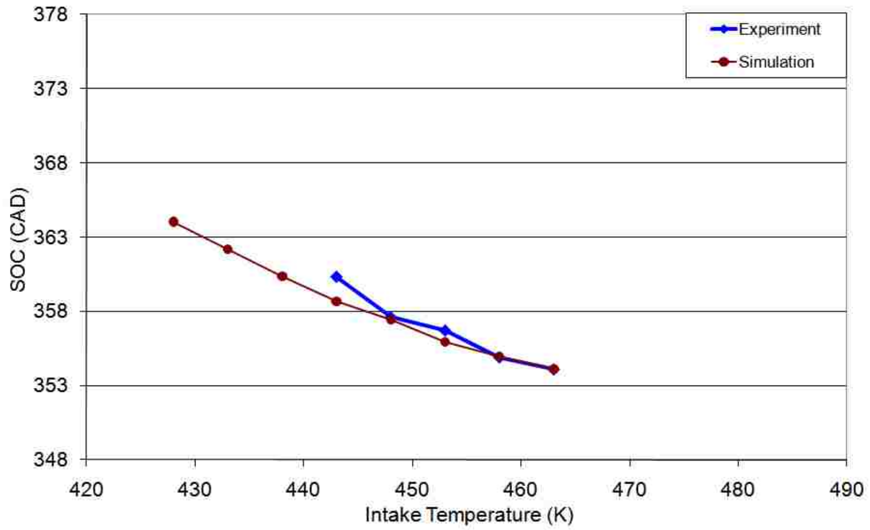

Figure 3.8: Integrated Arrhenius Rate: Start of Combustion Comparison between Experiment and Simulation (9 g/min)

Figure 3.8 shows that the simulation does a very good job of predicting the onset of combustion. Both the magnitude and the trend of the start of combustion seem to be captured by the control model. This makes sense due to the fact that the model was calibrated using the experimental start of combustion data. Figure 3.8 shows that the model was calibrated at an intake temperature of 190^{o}C (463 K), and then allowed to predict the onset of combustion for the remaining set of inlet conditions. Since the start of combustion is a major factor in determining the performance of an HCCI engine, the ability to accurately track its evolution is therefore vital to the operation of any type of control model. Figure 3.8 shows that the control model successfully captures both the magnitude and the trend of the onset of combustion when compared against experimental data. This provides evidence that the simplified control model is still doing a reasonable job of predicting engine outputs.

The next parameter that was investigated was the crank angle at which the peak pressure was occurring, θ_{23}. Within the model, this parameter was closely related to the crank angle at the start of combustion. The only difference between the two lay in the combustion duration term, $\Delta\theta$, which was added to account for the combustion event not occurring instantaneously. Once the reactant mixture starts to combust, there will be some finite amount of time before the reaction is completed. This finite amount of time is represented by the combustion duration term, and is simply added onto the start of combustion within the control model in order to predict θ_{23}. With this new term now added, the model can be compared with the experimental data in order to determine how accurately it is predicting θ_{23}. The most logical experimental value to compare against is the CA50 value, which is the crank angle at which 50 percent of the total heat release has occurred. The simulation was run for the same inlet conditions and the results, as well as the experimental CA50 values, can be found in Table 3.2. These results were plotted against one another and can be seen in Figure 3.9 below.

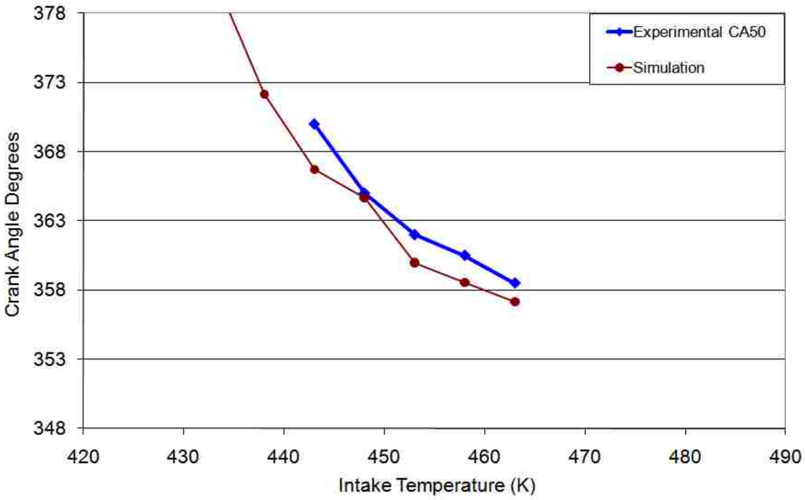

Figure 3.9: Integrated Arrhenius Rate: Angle of Peak Pressure Comparison between Experiment and Simulation (9 g/min)

Figure 3.9 shows that the model also does a reasonable job of predicting θ_{23}. The overall magnitudes are again slightly off, but the general trend seems to be captured by the simulation. The reasoning behind the difference in magnitudes can again be explained by looking at the combustion duration term, $\Delta\theta$. Similar to the case of the peak pressure, the duration of combustion has a direct impact on the crank angle at which θ_{23} is occurring within the model. As described previously, the model utilizes a variable $\Delta\theta$ correlation which varies the combustion duration based largely on where SOC is occurring. The model is calibrated using experimental SOC data, and the $\Delta\theta$ correlation is then used in order to predict values for θ_{23}. There is therefore no direct calibration of θ_{23}, which explains why the magnitudes seen in Figure 3.9 are slightly different. Despite these slight differences in magnitude, however, Figure 3.9 shows that the simulation does successfully capture the overall trend of θ_{23}. Similar to the case of the peak pressure, capturing this overall trend is more important for control than precisely predicting the values.

The next parameter was the temperature at the start of compression. This point represented the temperature of the mixture after the induction and mixing of both reactants and products. The simulation was again run for the same inlet conditions and compared with the experiment. These results were tabulated and can be seen in Table 3.2 along with the experimental values. These results were also plotted, and the results can be found in Figure 3.10 below.

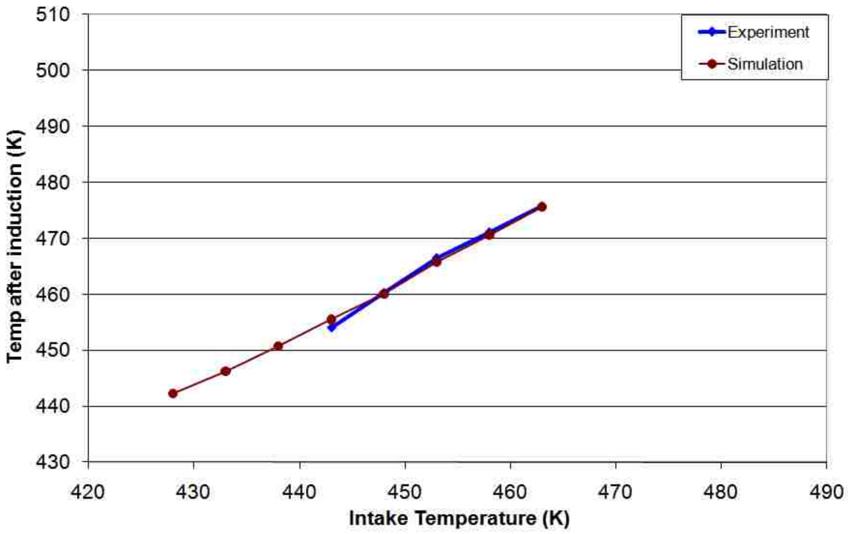

Figure 3.10: Integrated Arrhenius Rate: Temperature after Induction Comparison between Experiment and Simulation (9 g/min)

From Figure 3.10, it is evident that the simulation predicts the temperature at the start of compression (T_1) very well. The slopes of the lines are almost identical, and the magnitudes are only slightly off. One reason for the slight difference in magnitudes comes about due to the simplicity of the model. While the model includes a heat transfer term to account for the heat lost during the induction phase, the actual mixing of reactants and products is far too complex to be able to precisely model the heat transfer that takes place. Due to this complexity, the model therefore cannot be expected to exactly predict the temperature following mixing. With that being said, the model still predicts values for T_1 that are very similar to the experimental values, which is again all that can be expected due to the simplistic nature of the model. Once again, capturing the general trend is what is most important with respect to the control model. Figure 3.10 displays that this trend is indeed captured, which supplies even more evidence that this simplified version of the Arrhenius Rate model is sufficiently accurate.

The pressure just before the start of combustion was the next parameter of interest. While this parameter is usually not of particular interest with respect to engine performance, it can still be used in order to verify whether or not the simulation is predicting reasonable values. The simulation was run again, and compared against the experimental pressure values. These results can be found in Table 3.3. Once the values were known, they could be plotted on the same graph for comparison. This plot can be seen in Figure 3.11 below.

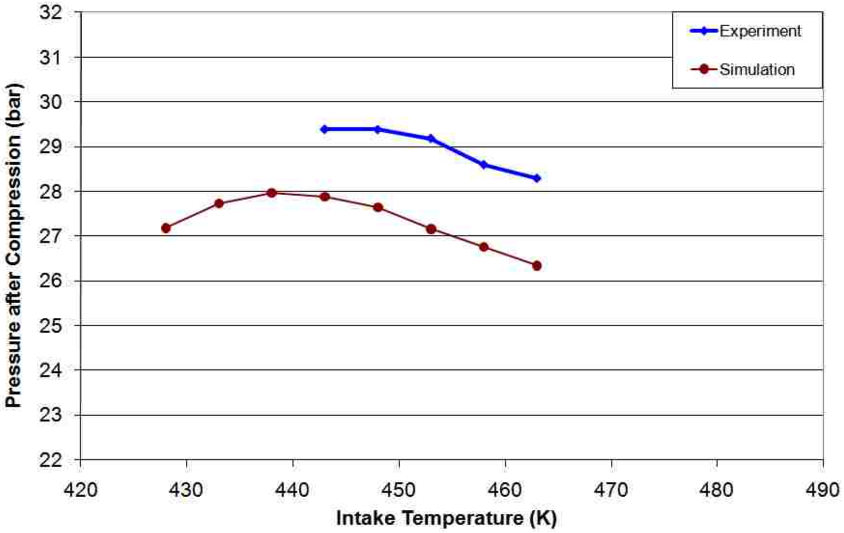

Figure 3.11: Integrated Arrhenius Rate: Pressure after Compression Comparison between Experiment and Simulation (9 g/min)

The plot in Figure 3.11 shows that the simulation successfully tracks the pressure in the cylinder after compression. Similar to the temperature after induction, the simulation again seems to predict the overall trend of the pressure evolution, but the magnitudes are again slightly off. These differences are once again due to the assumptions and simplifications made in developing a simplistic model for control. Similar to the previous argument for the peak pressure parameter, however, these differences in magnitude are not detrimental. As long as the simulation is able to predict the general behavior of the pressure evolution, that is all that is required for a control scheme to operate. As seen in Figure 3.11, the model does indeed capture this trend, which supports the idea that it is accurate enough to be implemented in an actual control scheme.

The pressure after expansion, at the instant the exhaust valve opens, is yet another parameter of interest. While this pressure is typically not of much interest from the viewpoint of engine performance, it is readily available from the experiment and therefore supplies an additional benchmarking point for the control model. The simulation was run and compared against the experiment, and the results of this comparison can also be found in Table 3.3. These results were also plotted against each other, and can be found in Figure 3.12 below.

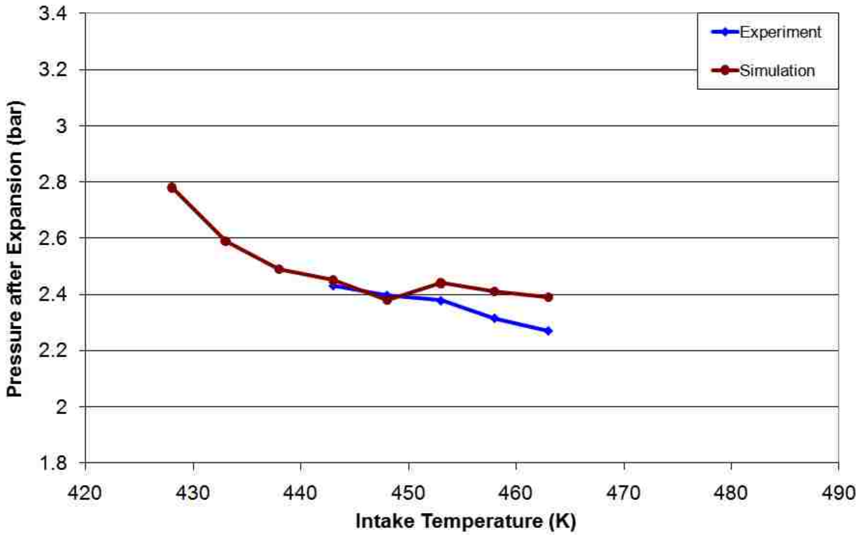

Figure 3.12: Integrated Arrhenius Rate: Pressure after Expansion Comparison between Experiment and Simulation (9 g/min)

It can be seen in Figure 3.12 that the control model is also successful in predicting the pressure after the expansion stroke, at the instant the exhaust valve opens. Similar to the previous parameters investigated, the magnitudes are slightly different, but the overall trend is the same. The differences in magnitude are again a result of the simplifications made to the model. While the magnitudes are slightly off, they are still being predicted within 10 percent of the experiment, which is very reasonable considering the simple model being used. Figure 3.12 shows that the control model captures the general behavior of the pressure evolution after the expansion stroke. This is yet more proof that the simplified control model in question is indeed capable of accurately predicting engine outputs.

Another parameter that was readily available for comparison was the temperature in the cylinder after combustion. Since this temperature occurred immediately after combustion, it was therefore the peak temperature within the cycle. The temperatures predicted by the model, along with those from the experiment, were tabulated and can be found in Table 3.4 above. These values were plotted, and can be seen in Figure 3.13 below. In this Figure, the model once again behaves as it did in Figure 3.7, when it was predicting the peak pressure in the cycle. The argument in this case is once again similar to that of the peak pressure case. The overall trend of the temperature evolution is captured, but the magnitudes are again different. This difference in magnitude can once again be attributed to the simplifications that were made to the model. Due to the simplistic nature of the model, factors such as heat

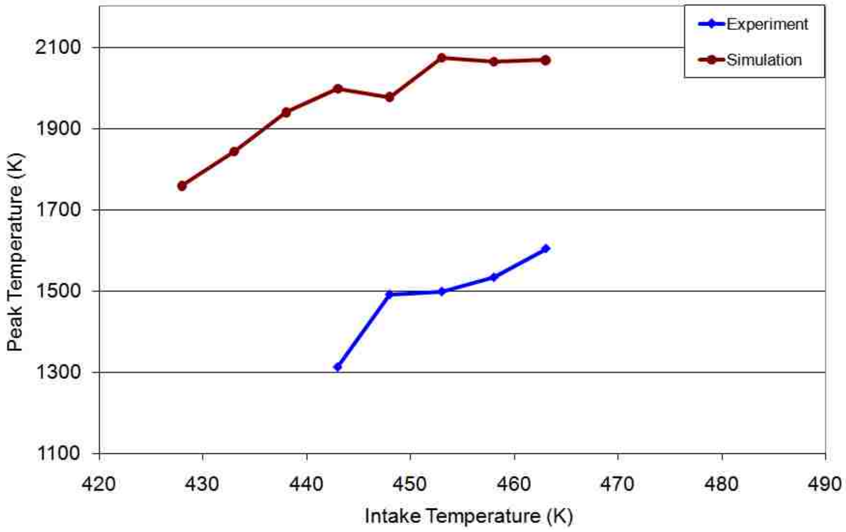

Figure 3.13: Integrated Arrhenius Rate: Peak Temperature Comparison between Experiment and Simulation (9 g/min)

transfer are not completely accounted for. This results in the model predicting values, especially for temperatures, that are higher than those from the experiment. This behavior can be observed in Figure 3.13 above. Even though the model seems to over predict the peak temperature in the cycle, the general behavior of the parameter is captured for changes in inlet conditions. Similar to previous arguments, this overall trend is all that is required for the control model to operate effectively.

The next parameter that was used to benchmark the control model was the exhaust temperature. This parameter was of importance due to the fact that it had a direct impact on the temperature of the following cycle. Since exhaust gas recirculation was being utilized on the engine, the temperature of the re-inducted exhaust from the previous cycle acted to heat up the intake charge. This acted to provide a direct link from cycle to cycle within the operation of the engine. These temperatures were obtained from the model and experiment, and the results can be found in Table 3.4. These temperatures were then plotted against each other, and this can be found in Figure 3.14 below.

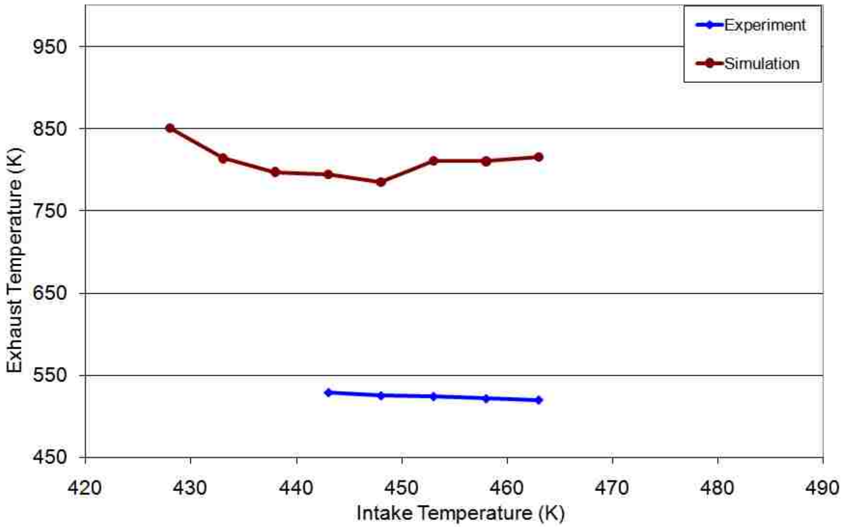

Figure 3.14: Integrated Arrhenius Rate: Exhaust Temperature Comparison between Experiment and Simulation (9 g/min)

The results in Figure 3.14 show that when predicting the exhaust temperature, the model once again displays a certain delay. Similar to the case of the peak pressure, this delay is once again caused by the combustion duration term which was added to the model. As described previously, the Δθ correlation in the model acts to delay the peak pressure location from going past top dead center. In the experimental data the combustion duration varies slightly faster, which causes the peak pressure to initially occur at top dead center and then increasingly expand out into the expansion stroke. Since the volume at which peak pressure occurs is directly related to θ_{23}, the model displays a slightly delayed prediction of the exhaust temperature. Since the exhaust was determined to be isentropic, the exhaust temperatures in the model are therefore dependent on the volume at which the peak pressure is occurring. Since the model predicts that this volume initially decreases up to top dead center and then begins to increase, the resulting exhaust temperatures therefore also decrease before they start to increase. Since the actual combustion duration is variable, the experiment shows that the exhaust temperature should begin increasing immediately as the intake temperature is decreased. Again similar to the case of peak pressure, the correct increasing trend is captured by the model, it is merely delayed. Since top dead center is the critical inflection point for the cylinder volume, the model will always have some inherent delay when the combustion event crosses over this threshold. The fact that the magnitudes are different can once again be explained by the simplifications to the model. Since heat transfer is not entirely accounted for, the temperatures predicted by the model cannot be expected to match exactly with the experiment. Other than the slight delay that occurs around top dead center, Figure 3.14 shows that the control model accurately predicts the correct trend in the exhaust temperature evolution, which is again all that is necessary in order for the control model to operate effectively.

The final parameter that was used to benchmark the control model was the pressure rise rate. This parameter was of importance due to the fact that it had a direct impact on the operating range of the engine. Once the rate of pressure rise within the cylinder reached a certain threshold, the combustion event would become violent and would lead to excessive noise emission from the engine. These pressure rise rates were obtained from the model and experiment, and the results can be found in Table 3.4.

These values were then plotted against each other, and the results can be found in Figure 3.15 below.

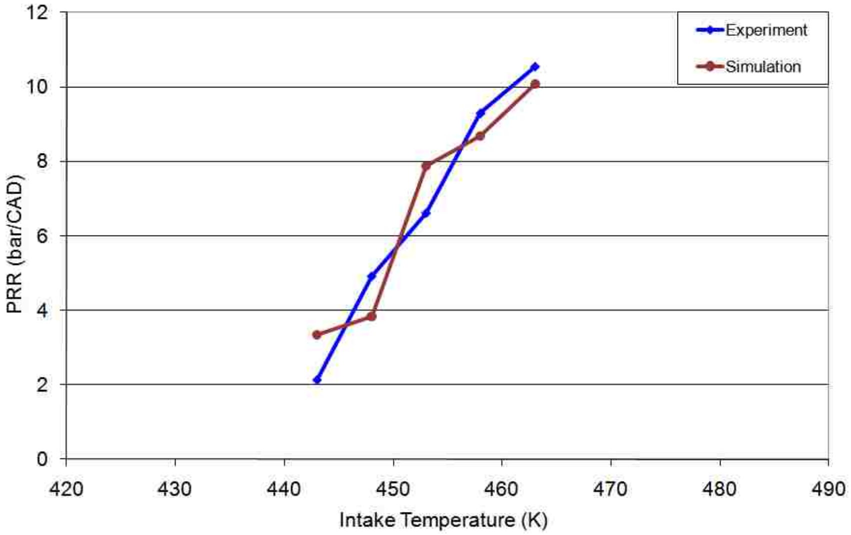

Figure 3.15: Integrated Arrhenius Rate: Pressure Rise Rate Comparison between Experiment and Simulation (9 g/min)

It can be seen in Figure 3.15 that the control model is successful in predicting the pressure rise rate. Similar to the previous parameters investigated, the magnitudes are again slightly different, but the overall trend is effectively captured. These differences in magnitude arise due to the simplified expression which is used to predict the pressure rise rate within the model. Despite these slight differences, however, Figure 3.15 shows that the control model captures the general trend of the pressure rise rate as the intake temperature is decreased.

3.3 C_7H_{16}: 6 G/MIN FUELING RATE

With the control model already benchmarked against experimental UTG96 data, the next step was to further validate the model by benchmarking it against another set of experimental data at a different operating point. This new set of data again used UTG96 as the fuel, but had a significantly different fueling rate than that of the previous data. This reduction in fueling rate caused the equivalence ratio to drop to 0.25, while the external EGR was still held at zero. In order to benchmark the model for this fueling rate, the intake temperature was again varied while all other inputs were held constant. The Arrhenius Rate threshold value, as well as the value for θ_{offset}, was also held constant based on previous discussions. This again forced any changes in the model outputs to be directly related to the changes in intake temperature. The results of this benchmarking were tabulated, and can be seen below.

Table 3.5: Integrated Arrhenius Rate: Comparison of Experiment and Simulation I (6gpm)

Intake Temp (K)	$P_{max, exp}$ (bar)	$P_{max, model}$ (bar)	% error	$\theta_{SOC, exp}$ (CAD)	$\theta_{SOC, model}$ (CAD)	% error
488	46.03	46.92	1.93%	350.7	351.9104	0.34%
483	46.22	48.4	4.72%	351.7	352.2764	0.16%
478	45.65	48.32	5.85%	353.0	352.9058	-0.01%
473	43.83	48	9.51%	354.2	353.5889	-0.17%
468	42.47	46.31	9.04%	355.3	354.4046	-0.25%
463	40.26	41.33	2.66%	356.5	355.3997	-0.32%
458	36.41	38.76	6.45%	358.4	356.3181	-0.58%
453		31.74			357.457	
448		23.03			358.7147	

Table 3.6: Integrated Arrhenius Rate: Comparison of Experiment and Simulation II (6gpm)

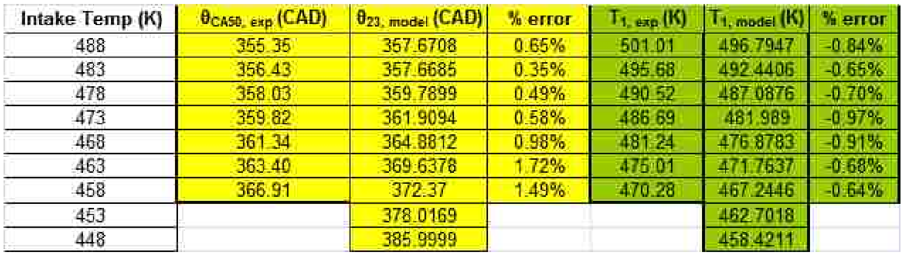

Intake Temp (K)	$\theta_{CA50, exp}$ (CAD)	$\theta_{23, model}$ (CAD)	% error	$T_{1, exp}$ (K)	$T_{1, model}$ (K)	% error
488	355.35	357.6708	0.65%	501.01	496.7947	-0.84%
483	356.43	357.6685	0.35%	495.68	492.4406	-0.65%
478	358.03	359.7899	0.49%	490.52	487.0876	-0.70%
473	359.82	361.9094	0.58%	486.69	481.989	-0.97%
468	361.34	364.8812	0.98%	481.24	476.8783	-0.91%
463	363.40	369.6378	1.72%	475.01	471.7637	-0.68%
458	366.91	372.37	1.49%	470.28	467.2446	-0.64%
453		378.0169			462.7018	
448		385.9999			458.4211	

Table 3.7: Integrated Arrhenius Rate: Comparison of Experiment and Simulation III (6gpm)

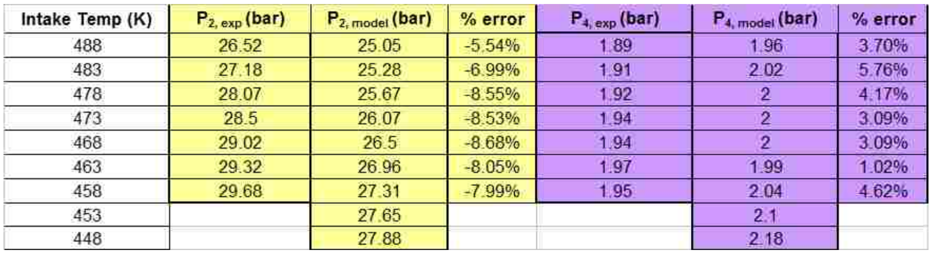

Intake Temp (K)	$P_{2, exp}$ (bar)	$P_{2, model}$ (bar)	% error	$P_{4, exp}$ (bar)	$P_{4, model}$ (bar)	% error
488	26.52	25.05	-5.54%	1.89	1.96	3.70%
483	27.18	25.28	-6.99%	1.91	2.02	5.76%
478	28.07	25.67	-8.55%	1.92	2	4.17%
473	28.5	26.07	-8.53%	1.94	2	3.09%
468	29.02	26.5	-8.68%	1.94	2	3.09%
463	29.32	26.96	-8.05%	1.97	1.99	1.02%
458	29.68	27.31	-7.99%	1.95	2.04	4.62%
453		27.65			2.1	
448		27.88			2.18	

Table 3.8: Integrated Arrhenius Rate: Comparison of Experiment and Simulation IV (6gpm)

Intake Temp (K)	$T_{3, exp}$ (K)	$T_{3, model}$ (K)	% error	$T_{ex, exp}$ (K)	$T_{5, model}$ (K)	% error	PRR_{exp} (bar/CAD)	PRR_{model} (bar/CAD)	% error
488	1389.7	1781.9	28.22%	477.96	734.8	53.74%	5.38	3.7964	-29.43%
483	1391.56	1820.6	30.83%	477.09	745.4	56.24%	4.94	4.2879	-13.20%
478	1371.3	1785.5	30.20%	474.85	731.3	54.00%	4.28	3.2898	-23.14%
473	1326.32	1764	33.00%	472.58	723.6	53.12%	3.43	2.6359	-23.15%
468	1289.02	1730.1	34.22%	470.67	715.6	52.04%	2.85	1.891	-33.65%
463	1256.02	1666.3	32.67%	472.18	707.6	49.86%	2.32	1.0097	-56.48%
458	1192.25	1657.8	39.05%	469.20	714.5	52.28%	1.34	0.7132	-46.78%
453		1598.5			721.4			0.5269	
448		1515.4			736.4			0.4689	

As the intake temperature was varied, the model again seemed to track the experimental values fairly well. Similar to the previous fueling rate, the model was again run for intake temperatures outside of the range of experimental values. This allowed for the behavior of the model outside of the experimental range to be investigated. Once again, the outputs from the model were deemed to be the most important parameters, and were therefore investigated first. Table 3.5 shows the results of the peak pressure comparison, which were plotted on the same graph and can be seen below in Figure 3.16. This Figure shows the behavior of the peak pressure for both the experiment and simulation as the intake temperature is decreased. The most striking difference between the two lines in this case is the fact that they appear to be slightly offset from one another. This behavior was expected, however, again due to the simplistic nature of the model being used. The model does seem to effectively capture

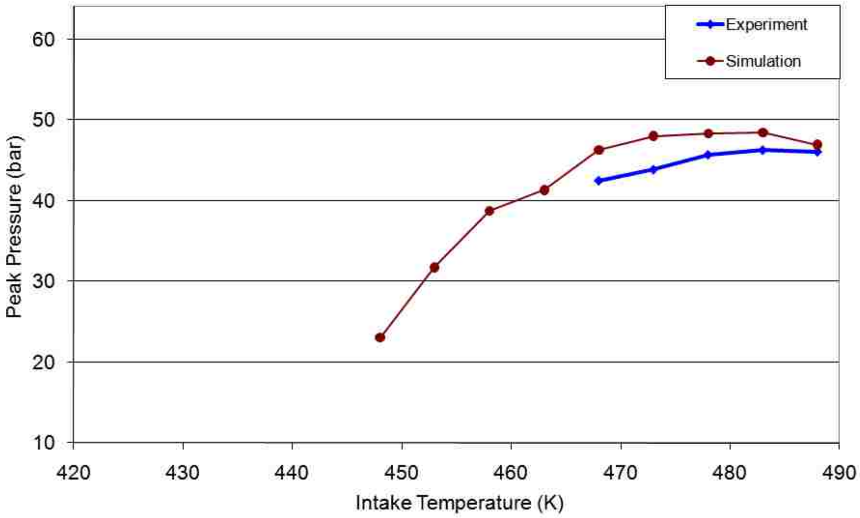

Figure 3.16: Integrated Arrhenius Rate: Peak Pressure Comparison between Experiment and Simulation (6 g/min)

the overall trend of the pressure evolution, with a slight delay from those observed in the experiment. This delay in the model can once again be explained by examining the critical dynamics that take place when the combustion event crosses over the TDC threshold. For the experimental case, Table 3.5 shows that the peak pressure begins to decrease immediately, despite the fact that the start of combustion is occurring before top dead center. This phenomenon is a result of the remainder of the compression stroke having a smaller impact on the peak pressure as the combustion event approaches TDC. In reality, when combustion occurs before TDC the pressure rise takes place during the compression stroke, which acts to increase the peak pressure. Since combustion is occurring closer and closer to TDC, the compression stroke therefore has less of an impact on the pressure and it decreases accordingly. This phenomenon is somewhat complex, and was therefore not included in the simplistic control model developed. Due to this simplification, the control model predicts that the peak pressure actually increases as combustion approaches TDC, which is evident in Table 3.5. Therefore, the delay apparent in Figure 3.16 enters the model through this simplification. Despite the delay, however, the overall trend of the experimental pressure is indeed captured. Once the model pushes the combustion event past TDC, the pressures begin to fall off similar to those in the experiment. As described previously, the correct prediction of these trends is central to the operation of the control model.

The next parameter that was investigated was the angle at which start of combustion occurred. The intake temperature was varied, and the results for the simulation, as well as the experiment, can be found in Table 3.5. These results were also plotted against each other, and this diagram can be found in Figure 3.17 below.

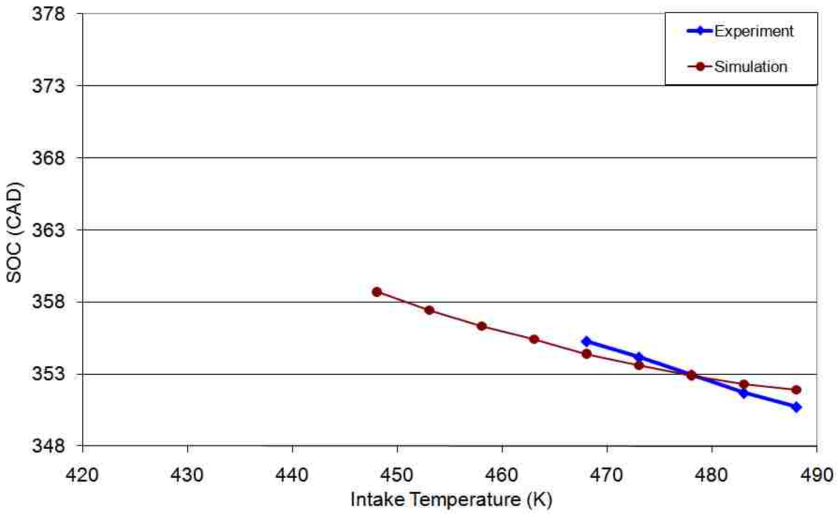

Figure 3.17: Integrated Arrhenius Rate: Start of Combustion Comparison between Experiment and Simulation (6 g/min)

Figure 3.17 shows that the simulation again does a very good job of predicting the onset of combustion. Both the magnitude and the trend of the start of combustion seem to be captured by the control model. Figure 3.17 reveals that the model was calibrated using experimental data from the previous fueling rate, which explains why the simulation is no longer “pinned” to the experiment. Since the same fuel was being used, the model could utilize the same threshold value in order to predict the onset of combustion as the inlet conditions were varied. Figure 3.17 also shows that the control model successfully captures both the magnitude and the trend of the onset of combustion when compared against experimental data. This provides evidence that the simplified control is doing a reasonable job of predicting engine outputs.

The next parameter that was investigated was the crank angle at which the peak pressure was occurring, θ_{23}. The most logical experimental value to compare against was again the CA50 value, which is again the crank angle at which 50 percent of the total heat release is realized. The simulation was run for the same inlet conditions as before and the results, as well as the experimental CA50 values, can be found in Table 3.6. These results were plotted against one another and can be seen in Figure 3.18 below. This Figure shows that the model also does a reasonable job of predicting θ_{23}. The overall magnitudes are again slightly off, but the general trend seems to be captured by the simulation. The reasoning behind the difference in magnitudes can again be explained by looking at the combustion duration term, $\Delta\theta$. As described previously, the model utilizes a variable $\Delta\theta$ correlation which varies the combustion duration based largely on where SOC is occurring. There is therefore no direct calibration of θ_{23}, which explains why the magnitudes seen in Figure 3.18 are slightly different. Despite these

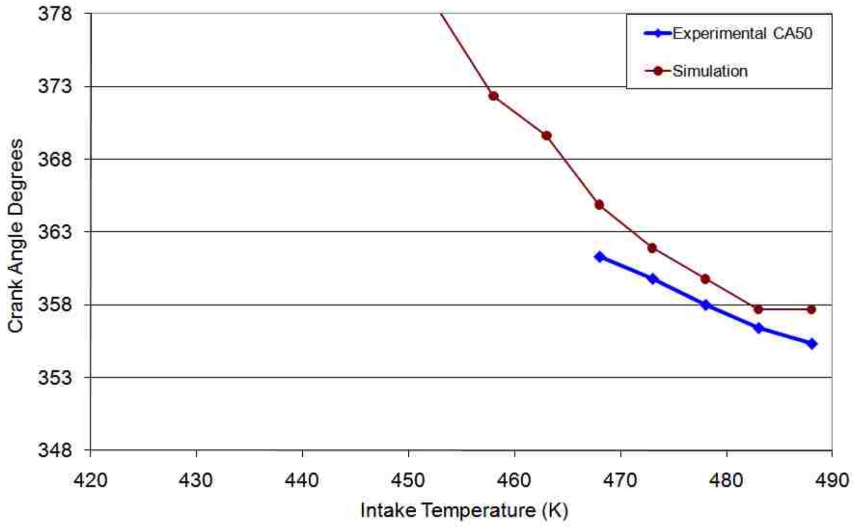

Figure 3.18: Integrated Arrhenius Rate: Angle of Peak Pressure Comparison between Experiment and Simulation (6 g/min)

slight differences in magnitude, however, Figure 3.18 shows that the simulation does successfully capture the overall trend of θ_{23}. Similar to the case of the peak pressure, capturing this overall trend is more important than precisely predicting the values.

The next parameter of interest was the temperature at the start of compression. This point represented the temperature of the mixture after the induction and mixing of both reactants and products. The simulation was run for the same inlet conditions and compared with the experiment. These results were tabulated and can be seen in Table 3.6 along with the experimental values. These results were also plotted, and the results can be found in Figure 3.19 below.

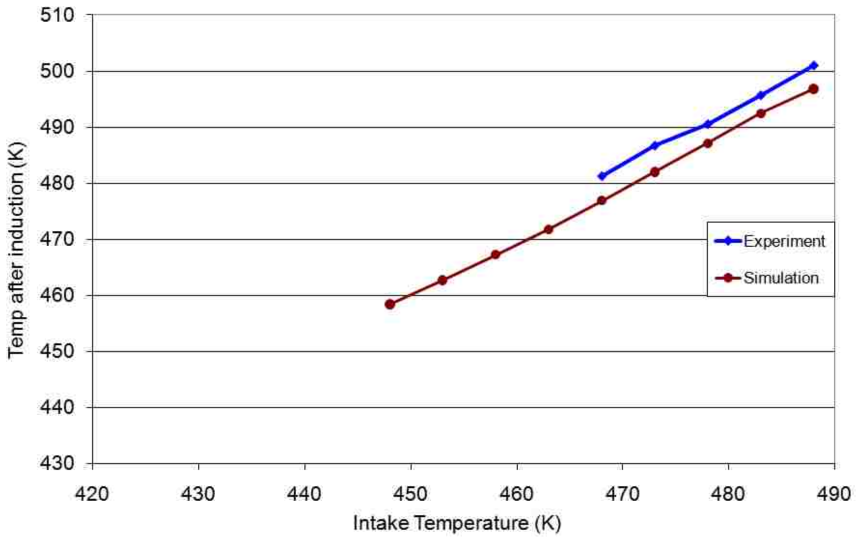

Figure 3.19: Integrated Arrhenius Rate: Temperature after Induction Comparison between Experiment and Simulation (6 g/min)

From Figure 3.19, it is evident that the simulation predicts the temperature at the start of compression very well. Similar to the data for the previous fueling rate, the slopes of the lines are almost identical and the magnitudes are only slightly off. One reason for the difference in magnitudes comes about due to the simplicity of the model. While the model includes a heat transfer term to account for the heat lost during the induction phase, the actual process is far too complex to model. With that being said, the model still predicts values for the temperature after induction that are within five degrees Kelvin of the experimental values, which is again all that can be expected due to the simplistic nature of the model. Once again, capturing the general trend is the most important with respect to the control model, and Figure 3.19 displays that this trend is indeed captured.

The next parameter of interest was the pressure just before the start of combustion. While this parameter is usually not of particular interest with respect to engine performance, it can still be used in order to verify whether or not the simulation is predicting reasonable values. The simulation was run again, and compared against the experimental pressure values from the Hatz engine. These results can be found in Table 3.7. Once the values were known, they could be plotted on the same graph for comparison. This plot can be seen in Figure 3.20 below.

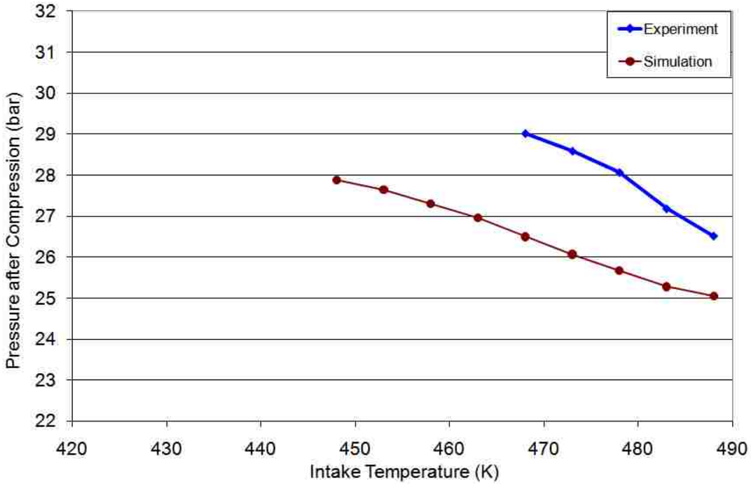

Figure 3.20: Integrated Arrhenius Rate: Pressure after Compression Comparison between Experiment and Simulation (6 g/min)

The plot in Figure 3.20 shows that the simulation successfully tracks the pressure in the cylinder after compression. Similar to the temperature after induction, the simulation again seems to predict the overall trend of the pressure evolution, with the magnitudes being only slightly off. As long as the simulation is able to predict the general behavior of the pressure evolution, that is all that is required for a control scheme to operate. As seen in Figure 3.20, the model does indeed capture this trend.

The pressure after expansion, at the instant the exhaust valve opens, is yet another parameter that can be used to benchmark the model with the experiment. While this pressure is usually not of much interest from the viewpoint of engine performance, it is readily available from the experiment and therefore supplies an additional benchmarking point for the control model. The simulation was run and compared against the experiment, and the results of this comparison can also be found in Table 3.7. These results were also plotted against each other, and can be found in Figure 3.21 below.

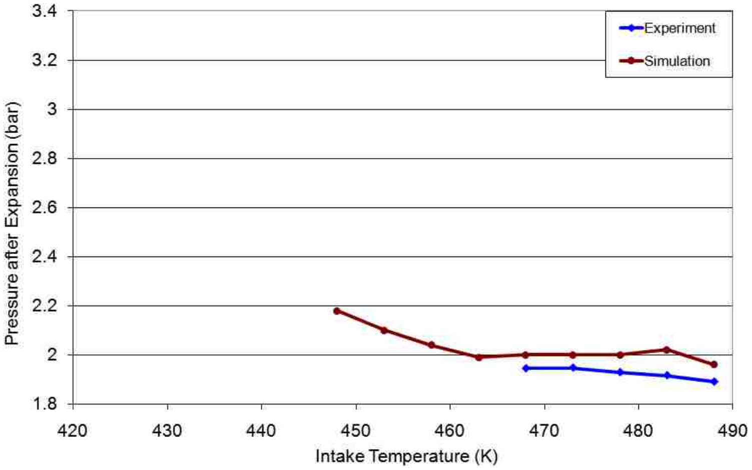

Figure 3.21: Integrated Arrhenius Rate: Pressure after Expansion Comparison between Experiment and Simulation (6 g/min)

It can be seen in Figure 3.21 that the control model is also successful in predicting the pressure after the expansion stroke, at the instant the exhaust valve opens. Similar to the previous parameters investigated, the magnitudes are slightly different, but the overall trend is the same. The differences in magnitude are again a result of the simplifications made to the model. Figure 3.21 shows that the control model captures the general behavior of the pressure evolution after the expansion stroke.

Another parameter that was readily available for comparison was the temperature in the cylinder after combustion. Since this temperature occurred immediately after combustion, it was therefore the peak temperature within the cycle. The temperatures predicted by the model, along with those from the experiment, were tabulated and can be found in Table 3.8 above. These values were plotted, and can be seen in Figure 3.22 below.

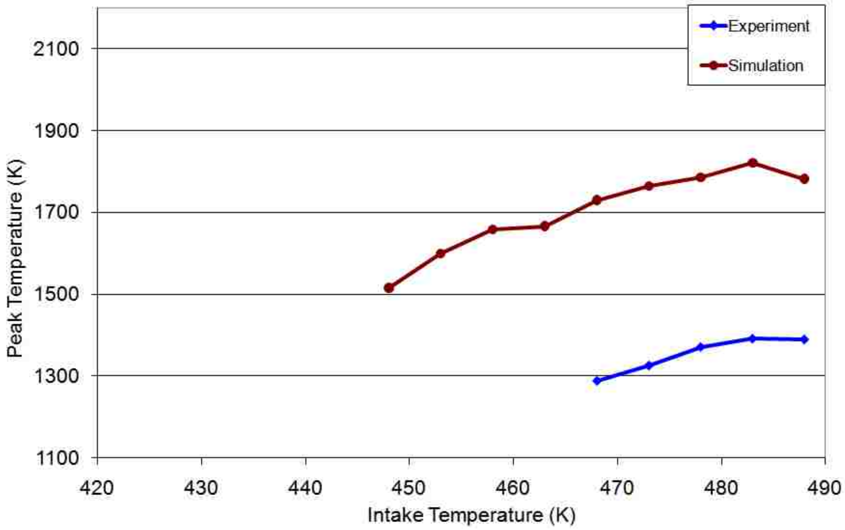

Figure 3.22: Integrated Arrhenius Rate: Peak Temperature Comparison between Experiment and Simulation (6 g/min)

In Figure 3.22, the overall trend of the temperature evolution is captured, but the magnitudes are again slightly different. This difference in magnitude can once again be attributed to the simplifications that were made to the model. Due to the simplistic nature of the model, heat transfer effects are not completely accounted for, which results in values, especially for temperatures, that are higher than those seen in the experiment. Even though the model seems to over predict the peak temperature in the cycle, the general behavior of the parameter is captured for changes in inlet conditions. Similar to previous arguments, this overall trend is all that is required for the control model to operate effectively.

The next parameter that was used to benchmark the control model was the exhaust temperature. Since exhaust gas recirculation was being utilized on the engine, the temperature of the re-inducted exhaust from the previous cycle acted to heat up the intake charge. This acted to provide a direct link from cycle to cycle within the operation of the engine. These temperatures were obtained from the model and experiment, and the results can be found in Table 3.8. These temperatures were then plotted against each other, and this can be found in Figure 3.23 below.

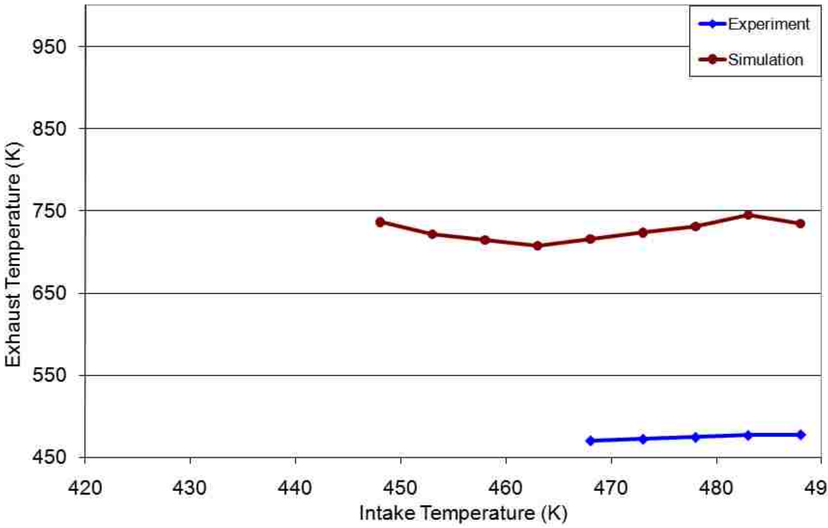

Figure 3.23: Integrated Arrhenius Rate: Exhaust Temperature Comparison between Experiment and Simulation (6 g/min)

The results in Figure 3.23 show that when predicting the exhaust temperature, the model once again displays a good correlation with the experiment. Again similar to the case of peak pressure, the correct decreasing trend is captured by the model; it is merely offset in magnitude. The fact that these magnitudes are different can once again be explained by the simplifications to the model. Since heat transfer is not entirely accounted for, the temperatures predicted by the model cannot be expected to match exactly with the experiment. Figure 3.23 shows that the model accurately predicts the correct trend in the exhaust temperature evolution, which is all that is necessary from a controls perspective.

The final parameter that was used to benchmark the control model was again the pressure rise rate. This parameter was of importance due to the fact that it had a direct impact on the operating range of the engine. These pressure rise rates were obtained from the model and experiment, and the results can be found in Table 3.8. These values were then plotted against each other, and the results can be found in Figure 3.24 below.

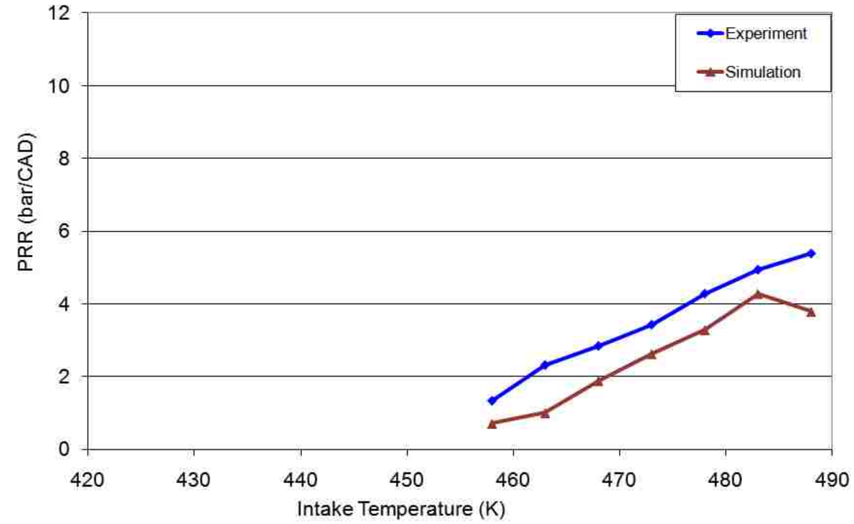

Figure 3.24: Integrated Arrhenius Rate: Pressure Rise Rate Comparison between Experiment and Simulation (6 g/min)

It can be seen in Figure 3.24 that the control model is again successful in predicting the pressure rise rate. Similar to the previous fueling rate investigated, the magnitudes are again slightly different, but the overall trend is the same. These differences again arise due to the simplified expression which is used to predict the pressure rise rate within the model. Despite these slight differences in magnitude, Figure 3.24 shows that the control model captures the general trend of the pressure rise rate as the intake temperature is decreased.

This simplified Arrhenius Rate model showed good correlation to the experiment for all of the parameters that were investigated for both fueling rates. Even if the model did not precisely track the parameter, it was still able to capture the overall trends of how that parameter was changing with inlet conditions. From the information supplied in Figures 3.16-3.24, it can therefore be concluded that this Arrhenius Rate model is capable of accurately predicting the trends of both the pressure and temperature evolution within the cylinder. Accurate prediction of these trends provides valuable evidence that this simplified Arrhenius Rate model can indeed be used in order to develop a control scheme for effective control of an HCCI engine.

3.4 HCCI OPERATING RANGE

HCCI test data taken from the Hatz 1D50Z single-cylinder engine at Oak Ridge National Labs seems to suggest a fairly narrow band of acceptable combustion timing values which result in stable HCCI operation. As the timing is advanced from TDC, combustion becomes increasingly violent resulting in higher and higher pressure rise rates (PRR) and therefore unacceptable amounts of noise emission from the engine. If the timing is retarded, combustion becomes sporadic and unpredictable resulting in large amounts of cyclic variation. In order to get a better understanding of this phenomenon, the combustion timing is varied within the model while the efficiency, along with PRR, is used as a gauge to determine an acceptable range of operation. The results of this analysis can be seen in Figure 3.25.

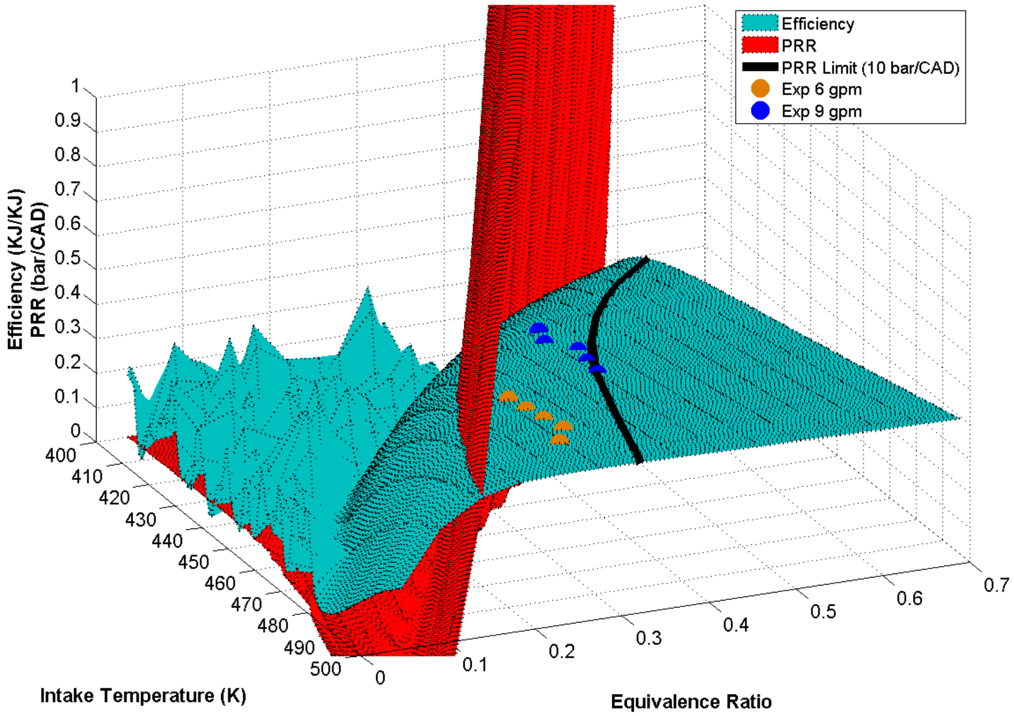

Figure 3.25: HCCI efficiency and PRR surface plots

Figure 3.25 shows both the efficiency (work out/fuel energy in) and the PRR predicted by the model for a variety of different intake temperatures and equivalence ratios. The efficiency (shown in blue) is predicted in the model using gross indicated work along with fueling rate, and serves to roughly indicate when stable HCCI combustion is being achieved. As shown in the Figure, the efficiency surface can be related to a waterfall, where the water originates from the corner of high equivalence ratios/intake temperatures and flows downstream to the corner of low equivalence ratios/intake temperatures. For relatively high equivalence ratios and intake temperatures (i.e. advanced combustion timing), the efficiency predicted by the model is fairly constant for a variety of setpoints, and increases slightly as the “water” approaches the falloff. For relatively low equivalence ratios and intake temperatures (i.e. retarded combustion timing), the efficiency displays large spikes, which indicates that combustion is becoming unstable thus resulting in large cyclic variations from cycle to cycle. Based on these findings, an operating window for stable HCCI combustion has been defined using the efficiency plot in Figure 3.25. The right edge of this window is defined using a PRR limit of 10 bar/CAD [17], and is represented in Figure 3.25 by the solid black line. This black line originates from the PRR predicted by the model (shown in red) and is simply transposed down onto the efficiency surface. The left edge of this operating window is already being predicted by the combustion model as the edge where the efficiency begins to fall off. In other words, the model is predicting stable, acceptable HCCI operation when the setpoint is kept to the right of the “waterfall” and to the left of the PRR limit. For comparison, experimental data from the Hatz is also included in Figure 3.25, and is represented by the small orange and blue spheres. As is evident, these experimental data points all fall within the window predicted by the model, which gives confidence that the model is indeed predicting a reasonable operating window for HCCI combustion.

4. PERTURBATION ANALYSIS

With the control model now developed and validated against experiment, a logical next step is to investigate the effect of perturbations, or disturbances, on the system. Within the control model there exist inputs which can be tweaked in order to control the various output variables. In simulation, it is possible to exactly specify these input variables without the inclusion of any type of extraneous noise. In practice, however, this is not possible. The inputs, which are intake temperature, fueling rate and external EGR fraction, are typically controlled on an actual engine using some sort of actuator. These actuators are mechanical devices, which cannot realistically be expected to provide noise free operation. There will always be some degree of uncertainty associated with the actuator, along with various other disturbances, which will cause the desired input to oscillate around some nominal value which has been specified by the ECU. In light of this behavior, disturbances must therefore be introduced into the control model in order to force the inputs to fluctuate around some nominal value. The effects of these disturbances on the model outputs can then be examined in order to determine the sensitivity of these outputs to small variations of the input variables. From a controls standpoint, it is desired that the outputs remain relatively unaffected by small variations in the inputs in order to maintain sufficient control of the process. Within the control model developed, inputs include a pre-heated intake temperature, fueling rate and the fraction of external EGR applied. In an effort to duplicate the small variations typically seen in implementation, a random number generator which used a Gaussian distribution about some nominal value was utilized. This random number generator effectively produced input values on a cycle to cycle basis that fluctuated around some desired input value. The magnitude of the fluctuations was chosen so as to represent typical variations seen during experiment. The intake temperature, which was controlled using a resistance heater, was allowed fluctuations of one percent of the nominal value. The fraction of external EGR, however, which was controlled using a solenoid, was allowed fluctuations of three percent of the nominal value. These perturbations then allowed the corresponding outputs to be monitored in order to determine their behavior.

4.1 TEMPERATURE PERTURBATIONS

The first perturbation analysis that was run corresponded to a fueling rate of 9 grams/minute, which resulted in an equivalence ratio of 0.38. The intake temperature was assigned nominal values between 420 K and 560 K in an attempt to stay within the typical HCCI operation range of the engine. For simplicity, the external EGR rate was set to zero during this analysis. The internal EGR fraction, α_i, was set at 0.05, which corresponded to typical values seen in the experiment. The intake temperature was varied under these conditions for 500 cycles, and return maps were created in order to display the results. Both output variables, peak pressure and θ_{23}, were investigated. The results of this initial investigation can be seen in Figures 4.1 and 4.2.

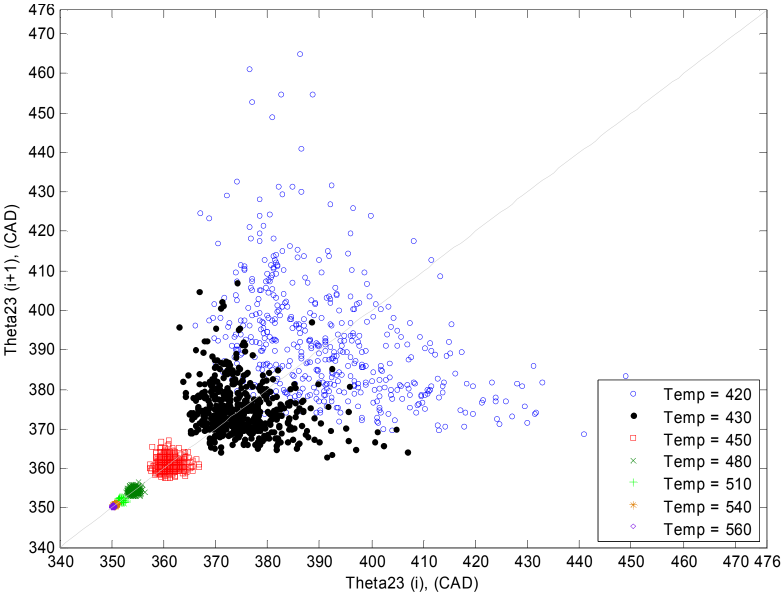

Figure 4.1: θ_{23} Return Map for Varying Intake Temperatures: low iEGR (9 gpm fuel rate)

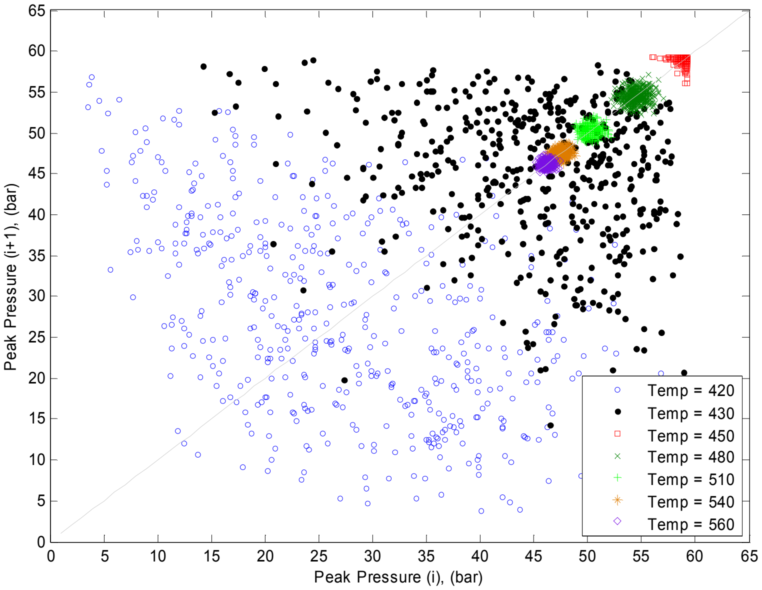

Figure 4.2: Peak Pressure Return Map for Varying Intake Temperatures: low iEGR (9 gpm fuel rate)

As the intake temperature was increased, Figure 4.1 shows an overall trend of the angle of peak pressure, θ_{23}, decreasing. This result makes physical sense due to the fact that a mixture which begins compression at a higher initial temperature should ignite sooner.

The model predicts that combustion timing will continue to advance with increasing temperature, and will cross the TDC threshold for an intake temperature of approximately 450 K. Figure 4.1 also reveals the sensitivity of θ_{23} to small variations of intake temperature around the five nominal values which were used. It appears as though θ_{23} gets less and less sensitive to perturbations as the intake temperature is increased. This trend is evident in Figure 4.1 due to the noticeably smaller variations in the output as intake temperature is disturbed. Figure 4.2 summarizes the second output, which is the peak pressure. Since peak pressure values rely on combustion timing for a particular engine cycle, these results follow closely to those seen in Figure 4.1. The variations again seem to diminish as the intake temperature is increased, as can be seen by the smaller variations between data points. Peak pressure is unique, however, in that it initially rises until it hits a maximum and then begins to fall. This result makes sense, though, due to the dependence of peak pressure on combustion timing. Since θ_{23} initially occurs after TDC (aTDC) and then advances to TDC, the pressure will inherently rise between those points and reach a maximum at TDC. As θ_{23} advances beyond that even further, the pressure will then begin to drop off again due to combustion initiating earlier in the compression stroke. Overall, the main trend observed in these plots was the tendency of the output sensitivity to decrease as nominal intake temperatures were increased. Figure 4.2 also seems to suggest an operating envelope for the engine, in that combustion does not occur for intake temperatures less than approximately 430K. Similar behavior has also been observed in the experimental data.

The next case investigated was similar in every way to the first case, with the exception of the internal EGR fraction. In the previous simulation, this parameter was set at 0.05 in order to reproduce experimental conditions. In this trial, however, the internal EGR fraction was increased to 0.4 in order to determine the behavior of the model when the intake temperature was perturbed about an elevated EGR rate. With all other test parameters the same, the intake temperature was again assigned nominal values between 420 K and 560 K with the external EGR set to zero for simplicity. Each intake temperature was run for 500 cycles, and return maps were created in order to display the results, which can be seen in Figures 4.3 and 4.4.

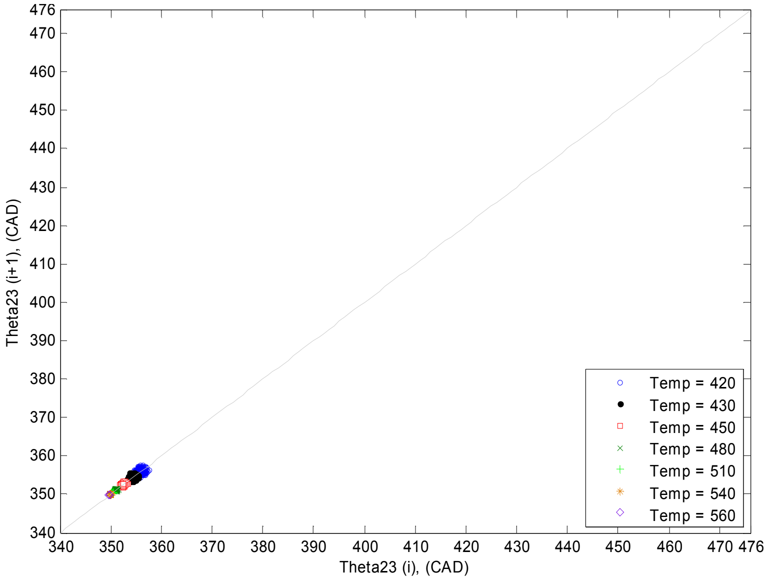

Figure 4.3: θ_{23} Return Map for Varying Intake Temperatures: high iEGR (9 gpm fuel rate)

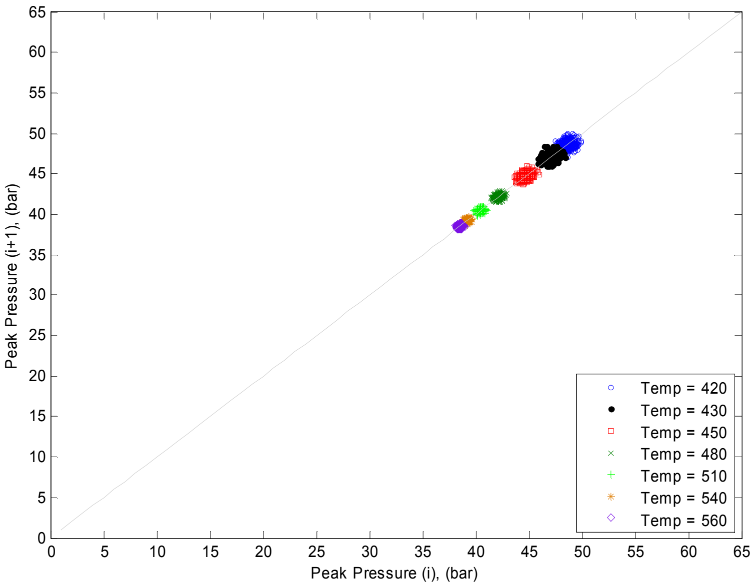

Figure 4.4: Peak Pressure Return Map for Varying Intake Temperatures: high iEGR (9 gpm fuel rate)

The effect of increasing the internal EGR in Figures 4.3 and 4.4 appears to have a drastic impact on the sensitivity of the output variables. For a high internal EGR, neither the angle of peak pressure, nor the peak pressure itself, appear to be significantly affected by perturbations of intake temperature. This is in stark contrast to the results seen in Figures 4.1 and 4.2 corresponding to a low EGR rate. This change in sensitivity can be explained by looking at the temperature effect of the internal EGR. It was previously concluded that sensitivity appeared to decrease as intake temperature increased with a low EGR rate. In this case, the internal EGR rate is now significantly higher, which acts to increase the in-cylinder temperature significantly from the previous case. Increasing the intake temperature still has the same overall effect on the system, i.e. advancing combustion timing along with decreasing pressure, the magnitude of this effect is merely reduced due to the higher initial temperature of the mixture due to the hot internal EGR present. Another interesting observation deals with the fact that for high internal EGR the range of combustion timings only varied 3-4 degrees whereas it varied almost 20 degrees for low EGR. This hints at the idea that temperature *difference* may play a role in determining the ability of the input to effectively vary the output.

With several cases already run for one fueling rate, the next step was to change this fueling rate in order to determine the effects it would have on the system outputs. This was accomplished by lowering the fueling rate to 6 grams/minute, which then resulted in an equivalence ratio of ϕ=0.25. With this change, the first two cases could now be repeated in order to determine the effects of altering the equivalence ratio. The intake temperature was again assigned nominal values between 420 K and 560 K and allowed to fluctuate +/- 1 percent of that value. The external EGR was again set at zero for simplicity, and the internal EGR was set at 0.05 to replicate experimental conditions. The simulation was run for 500 cycles at each intake temperature, and the results can be seen in Figures 4.5 and 4.6.

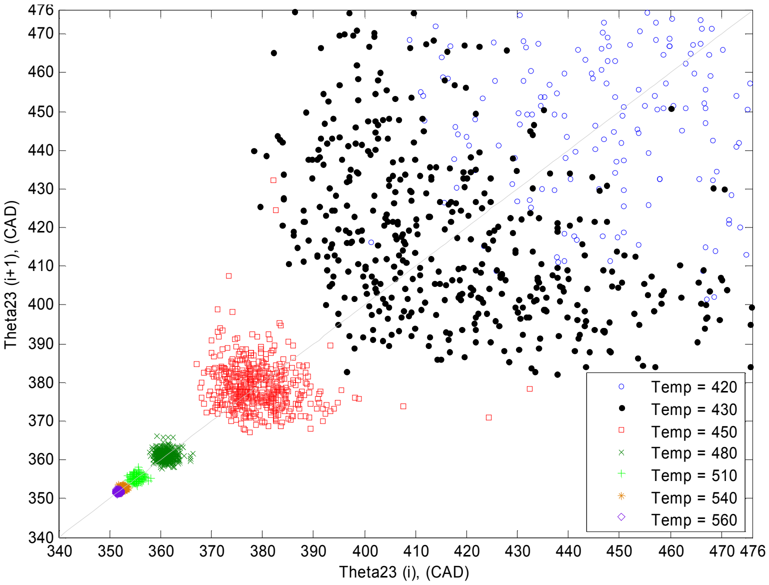

Figure 4.5: θ_{23} Return Map for Varying Intake Temperatures: low iEGR (6 gpm fuel rate)

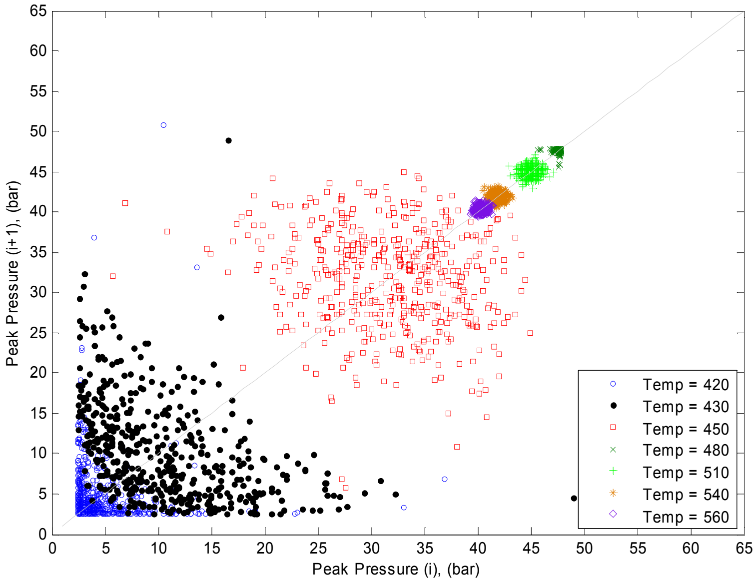

Figure 4.6: Peak Pressure Return Map for Varying Intake Temperatures: low iEGR (6 gpm fuel rate)

With the only change being a lowered fueling rate, the results in Figures 4.5 and 4.6 can therefore be directly compared with those in Figures 4.1 and 4.2 in order to determine the effect of changing the equivalence ratio. Comparison of the results shows that the overall behavior of the system is maintained for the lowered fueling rate, and that the magnitudes are merely shifted. Due to a leaner mixture, combustion is occurring later and with slightly more variability. The magnitude of the peak pressure is significantly reduced, which can again be attributed to the leaner mixture being burned. Overall, it still appears as though higher temperatures, and therefore more advanced combustion timing, lead to smaller sensitivities with respect to the output variables.

The next case run with the new fueling rate was similar to the previous one, with the only exception being the internal EGR rate. In order to duplicate the cases previously run, this case again set the internal EGR to 0.4 in order to determine the effect it would have on the sensitivity of the output variables. The intake temperature was still varied between 420 K and 560 K, and the external EGR remained at zero. The simulation was again run for 500 cycles at each intake temperature, and the corresponding results can be seen in Figures 4.7 and 4.8.

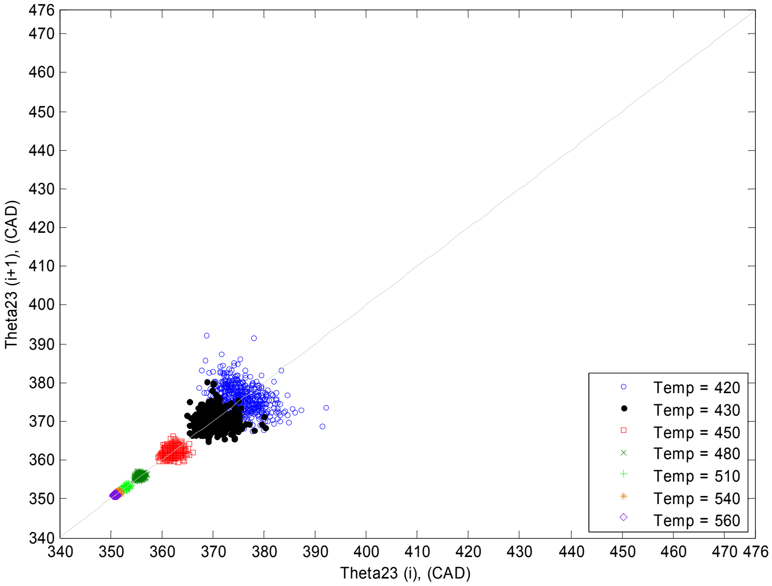

Figure 4.7: θ_{23} Return Map for Varying Intake Temperatures: high iEGR (6 gpm fuel rate)

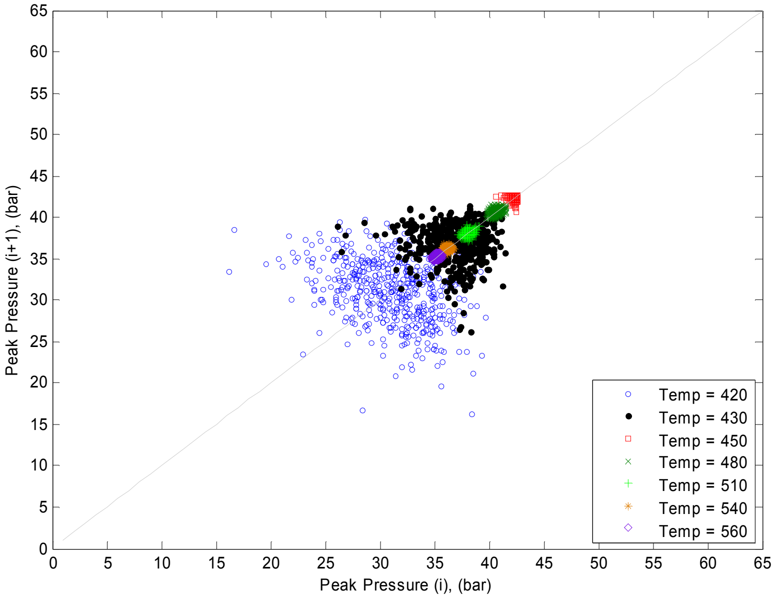

Figure 4.8: Peak Pressure Return Map for Varying Intake Temperatures: high iEGR (6 gpm fuel rate)

When compared to Figures 4.3 and 4.4, Figures 4.7 and 4.8 above display very similar results to those for the previous fueling rate. The overall behavior is still present, while the magnitudes are again slightly shifted. When compared to Figure 4.3, combustion timing, while advancing with increasing temperature, occurs slightly later for lower temperatures and again with slightly more variation. This variation is insignificant, however, when compared with the temperature perturbations at low internal EGR rates of shown in Figures 4.5 and 4.6. The peak pressure also shows more variation, and the overall magnitudes drop due to the leaner mixture in the cylinder.

4.2 INTERNAL EGR PERTURBATIONS

Another perturbation case was run using the original fueling rate of 9 grams/minute, which attempted to look at the effect of adding a disturbance to the internal EGR fraction. Despite the fact that the engine being modeled could not independently vary the internal EGR using variable valve timings, this analysis was performed to get a better understanding of what parameters the system outputs were most sensitive to. In order to accomplish this, the internal EGR, α_i, was assigned nominal values between 0 and 0.6 (0-36% by mass), and was allowed to fluctuate +/- 3% of that value. These values were chosen so as to represent reasonable values which could be attained on an actual engine. The external EGR fraction was again set to zero for simplicity. The intake temperature was set at 520K in order to attribute changes in the outputs solely to the variations of internal EGR. This analysis was run for 500 cycles at each nominal operating point, and the results can be seen in Figures 4.9 and 4.10.

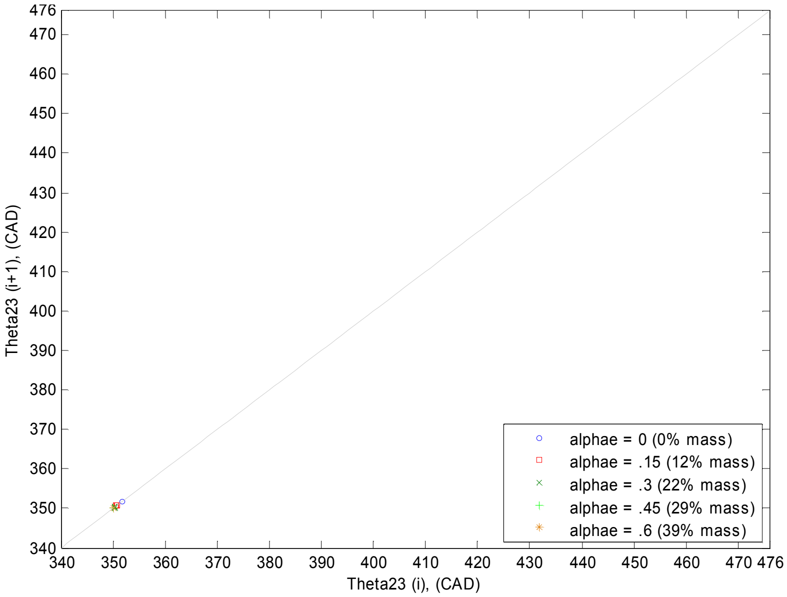

Figure 4.9: θ_{23} Return Map for Varying Internal EGR Rates: high Tin (9 gpm fuel rate)

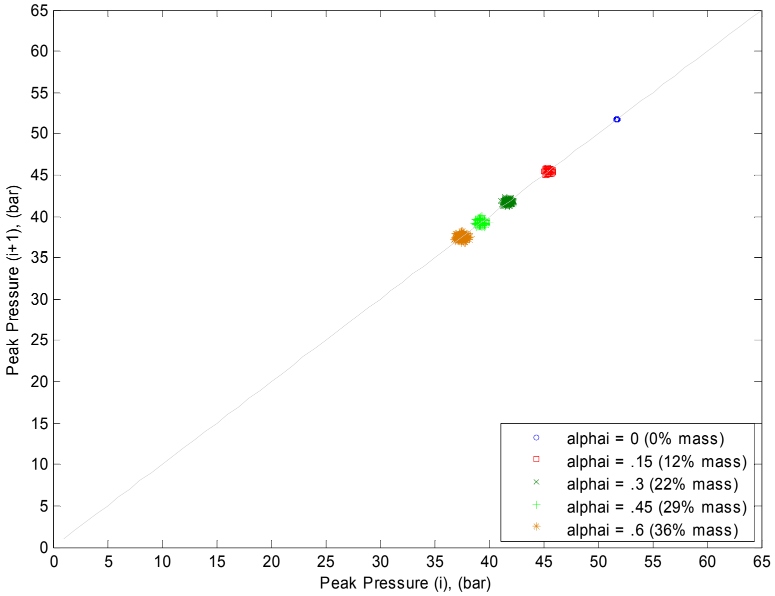

Figure 4.10: Peak Pressure Return Map for Varying Internal EGR Rates: high Tin (9 gpm fuel rate)

This analysis showed both output variables to be noticeably less sensitive to perturbations of internal EGR fraction than they were intake temperature. Both Figures 4.9 and 4.10 show that perturbing the internal EGR has only minor effects on θ_{23} and the peak pressure. This somewhat correlates to the previous assumption that sensitivity decreases with increasing temperature. For this case, the intake temperature was set at 520 K, which is already indicative of the upper end of the HCCI operating window. In addition, internal EGR has naturally elevated temperatures due to the hot exhaust gases, which acts to increase the temperature even more. This is one possible explanation for the decrease in output sensitivity. These results also make physical sense due to the elevated temperatures forcing combustion to always occur before TDC (bTDC). Since combustion continues to advance with increasing EGR, the peak pressure therefore decreases. One interesting observation from Figure 4.9 was that combustion timing seems to remain constant once the internal EGR fraction reaches approximately 0.4. This phenomenon was most likely due to the ability of the internal EGR to both heat up and dilute the fresh intake charge. This charge heating and dilution effectively cancel each other out at high EGR rates so that the combustion timing remains fairly constant.

The next case that was investigated was similar in every way to the previous case where the internal EGR was varied, with the exception of the nominal intake temperature. In the previous test, this parameter was held at 520 K in order to simulate a high nominal temperature. In this simulation, however, the intake temperature was lowered to 450 K in order to observe the behavior of the system when internal EGR was varied about a low nominal temperature. With the fueling rate held at 9 grams/minute and the internal EGR still assigned nominal values between 0 and 0.6, the simulation was again run for 500 cycles at each nominal EGR value. The results were summarized in return maps, which can be seen in Figures 4.11 and 4.12.

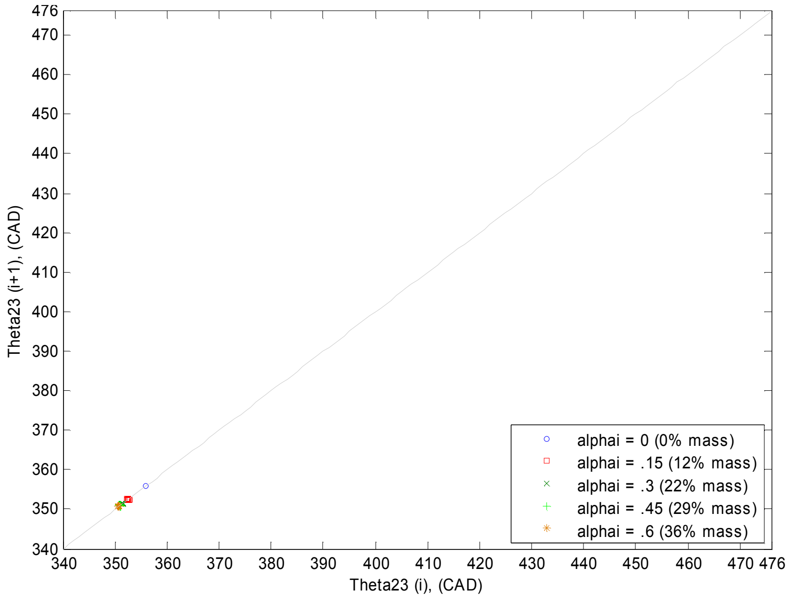

Figure 4.11: θ_{23} Return Map for Varying Internal EGR Rates: low Tin (9 gpm fuel rate)

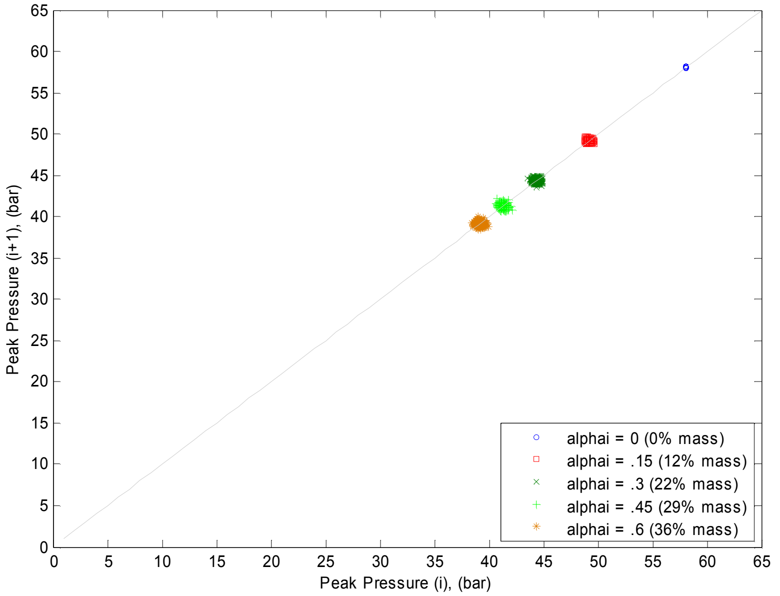

Figure 4.12: Peak Pressure Return Map for Varying Internal EGR Rates: low Tin (9 gpm fuel rate)

These results reveal that decreasing the intake temperature serves to increase the sensitivity of the outputs to perturbations of the internal EGR rate. This again seems to fortify the idea that sensitivity decreases with increasing temperature. Since the intake temperature was decreased for this run, the temperature in the cylinder therefore decreased as well. This could explain why there seems to be larger variations in the output variables in Figures 4.11 and 4.12 for identical variations in the internal EGR rate. The temperature in this case was high enough initially for combustion to occur bTDC, which resulted in the peak pressure continuing to decrease as EGR was increased. Similar to the previous case, the combustion timing once again seems to level off once the internal EGR rate reaches approximately 0.4.

With several cases already run for the fueling rate of 9 gram/minute, the next step was to change this fueling rate in order to determine the effects it would have on the system outputs. This was accomplished by again lowering the fueling rate to 6 grams/minute, which then resulted in an equivalence ratio of $\phi=0.25$. With this change, the first two cases could now be repeated in order to determine the effects of altering the equivalence ratio. The internal EGR fraction was again assigned nominal values ranging between 0 and 0.6 in order to duplicate realistic values seen on a typical engine, and allowed to fluctuate +/- 3 percent of that value. The external EGR was again set at zero for simplicity, while the intake temperature was held at 520 K in order to simulate a high temperature intake charge. This analysis was again run for 500 cycles at each nominal operating point, and the results can be seen in Figures 4.13 and 4.14.

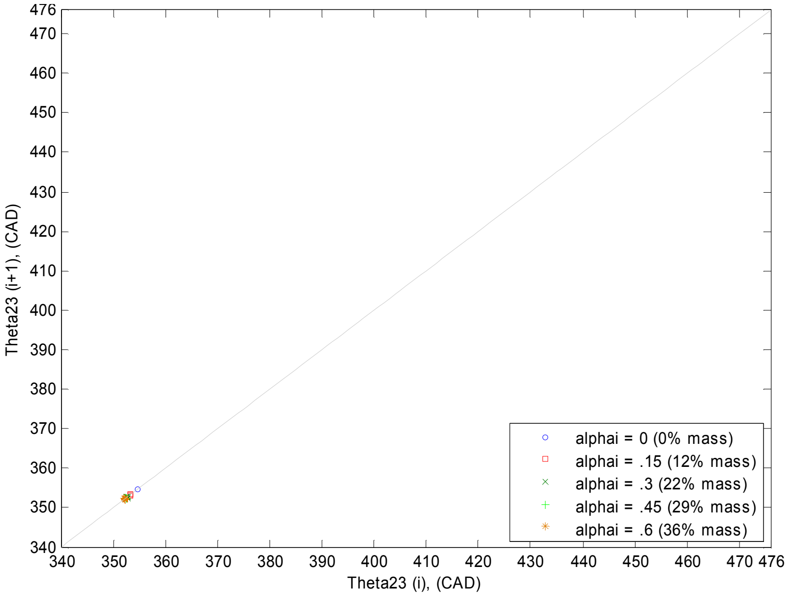

Figure 4.13: θ_{23} Return Map for Varying Internal EGR Rates: high Tin (6 gpm fuel rate)

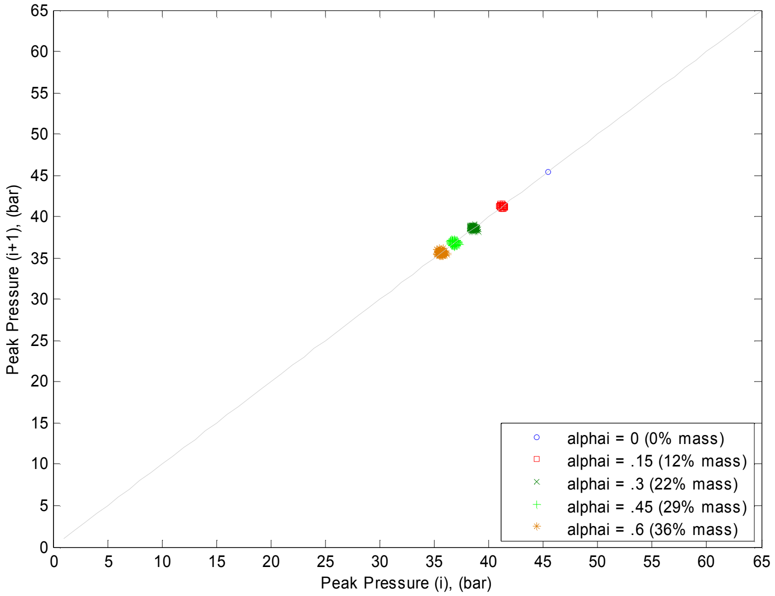

Figure 4.14: Peak Pressure Return Map for Varying Internal EGR Rates: high Tin (6 gpm fuel rate)

The results in Figures 4.13 and 4.14 show some striking similarities to those from the previous fueling rate. When compared to Figures 4.9 and 4.10, the overall behavior of the outputs are the same for each fueling rate. The elevated intake temperature forces combustion to always occur before TDC, which then results in very small variations at each setpoint. The actual magnitudes of the combustion timings are only slightly affected by the new fueling rate, where a slight retarding is seen due to less fuel in the cylinder. The variations in peak pressure are comparable to the previous fueling rate, with the overall magnitudes dropping slightly with the leaner mixture.

The next case again varied the internal EGR using the lowered fueling rate, the only difference being the nominal intake temperature. The previous test held the intake temperature at 520 K to simulate a high cylinder temperature, while this test lowered that temperature to 450 K in order to observe the effects of a low temperature intake charge. The internal EGR fraction, α_i, was again varied between 0 and 0.6, and the external EGR fraction, α_e, was held at zero in order to be consistent with the test run for the previous fueling rate. The simulation was run at these conditions, and the results are summarized in Figures 4.15 and 4.16.

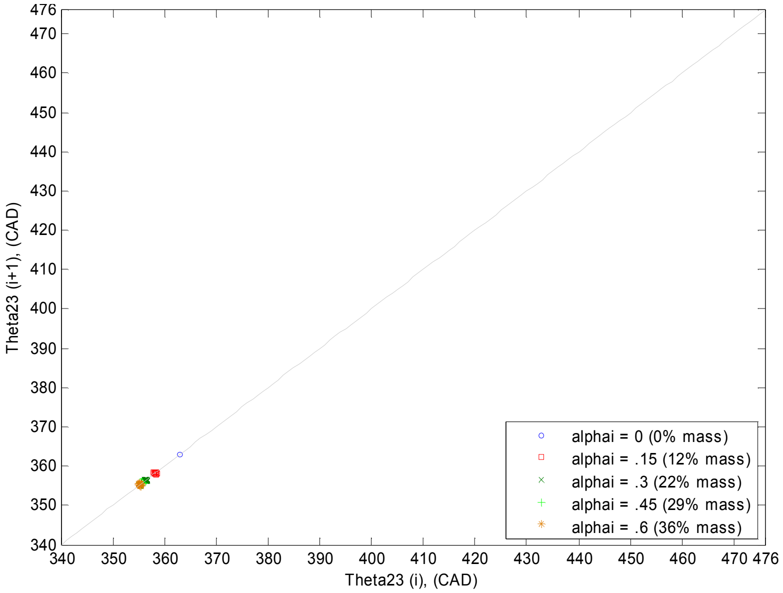

Figure 4.15: θ_{23} Return Map for Varying Internal EGR Rates: low Tin (6 gpm fuel rate)

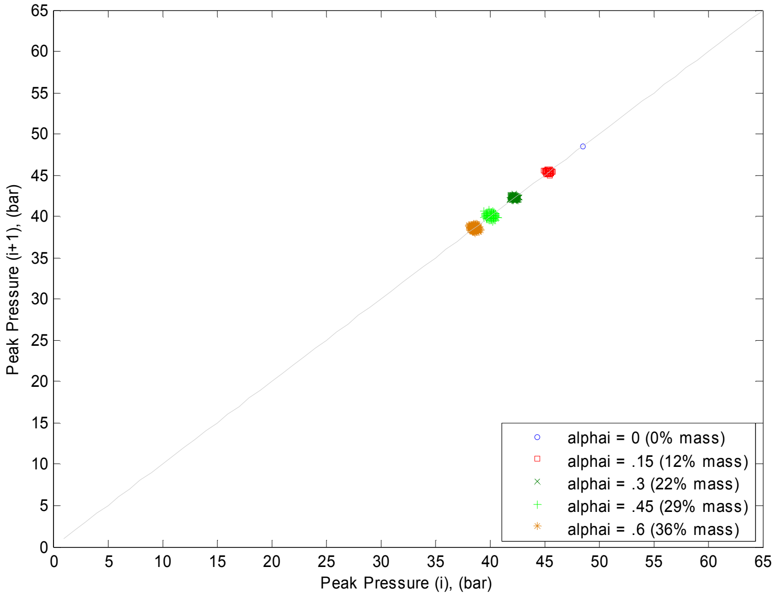

Figure 4.16: Peak Pressure Return Map for Varying Internal EGR Rates: low Tin (6 gpm fuel rate)

The results in Figures 4.15 and 4.16 can be directly compared to those of Figures 4.11 and 4.12 in order to determine the effect of changing the fueling rate. Similar to the previous cases, the results are again very similar to the previous fueling rate. The lowered intake temperature allows combustion to initiate after TDC, and then ultimately advance across the TDC threshold. The magnitudes of the combustion timing are slightly later for this fueling rate, which is reasonable due to the leaner mixture present in the cylinder. Also observed was the phenomenon of the combustion timing seemingly leveling off when the internal EGR rate reaches approximately 0.4. Similar to previous tests, the heating and dilution effects of the EGR are effectively cancelling each other out. The variations in both timing and peak pressure are again comparable for both fueling rates, with sensitivity seeming to increase slightly as the cylinder temperature drops. The peak pressure values are again smaller, which can be explained by the leaner mixture. Overall, the change in fueling rates seemed to affect only the overall magnitudes of the outputs, and not necessarily their sensitivities. Similar trends were seen for both fueling rates, which implies that the output sensitivities are not dependent upon the fueling rate being used.

4.3 EXTERNAL EGR INVESTIGATION

With the issue of changing fueling rates now addressed, the next logical parameter of interest is the external EGR rate, α_e. Similar to the intake temperature, this parameter is also an input to the control model which will be used to stabilize and control the model outputs. On an actual engine, this external EGR will likely be controlled with some sort of actuator. This implies that the EGR rate cannot be exactly specified, and that it will rather oscillate about some nominal operating point specified by the ECU. This is due to uncertainties, along with mechanical limitations, associated with the actuator device. In order to simulate this oscillatory behavior, perturbations were introduced to the input variable α_e. The end goal in this study was to determine the variations that these small perturbations would produce in the model outputs.

4.3.1 Low Temperature External EGR. The first case investigated in this series dealt with varying the intake temperature while the external EGR was held constant in an attempt to make a comparison to previous cases. In light of this, the intake temperature was again varied between 420 K and 560 K to be consistent. Since the fueling rate had previously been determined to be a nonfactor, it was arbitrarily chosen to be 9 grams/minute. The internal EGR was held constant at 0.05, also similar to previous tests. Since the external EGR was now being investigated, it was set at 0.4 to represent a high EGR rate, where it had been set to zero in previous tests to simulate a low EGR rate. In the end, this test consisted of varying the intake temperature for conditions of low internal EGR and high external EGR. Since external EGR must be rerouted into the intake stream via a lengthy process that allows for large amounts of heat transfer, the corresponding EGR temperature was set at 300 K. This assumed that the EGR being injected into the intake had been cooled down to ambient conditions. Under these conditions, the simulation was again run for 500 cycles at each intake temperature, and the results can be seen in Figures 4.17 and 4.18.

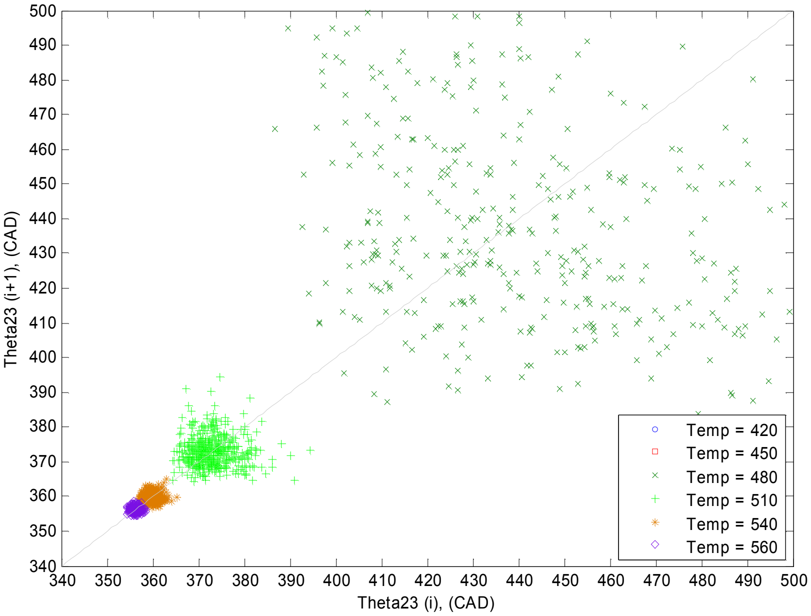

Figure 4.17: θ_{23} Return Map for Varying Intake Temperatures: cool eEGR (9 gpm fuel rate)

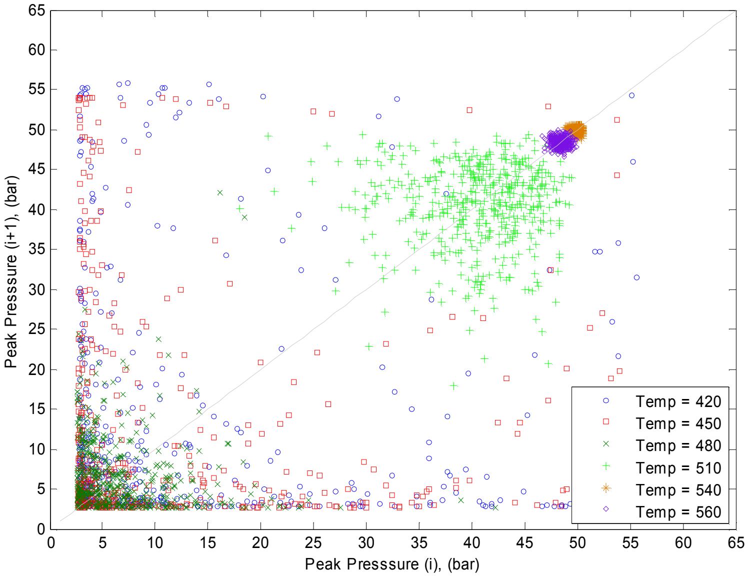

Figure 4.18: Peak Pressure Return Map for Varying Intake Temperatures: cool eEGR (9 gpm fuel rate)

With the only difference being the addition of cool external EGR, these results can be directly compared to those in Figures 4.1 and 4.2 in order to determine the effects on output sensitivity. Comparison between the two cases reveals that the system behaves significantly different when the intake temperature is varied about a high external EGR fraction. For the high EGR rate, the timing was significantly retarded as compared to the previous case due to the addition of large amounts of cooled EGR. This acted to cool the intake charge enough to require intake temperatures of approximately 510K before combustion would occur. This is in stark contrast to the intake temperatures of 430K required to initiate combustion at a low external EGR rate in Figure 4.1. The variation also appeared to increase for the case of high external EGR, especially for the operating points corresponding to later timing. This observation fortifies the idea that cooler temperatures, and therefore later combustion timing, increases the amount of variation in the outputs.

For the next case, the intake temperature was held constant while the external EGR fraction was varied. In order to simulate elevated temperatures, the intake temperature was held constant at 520 K. The internal EGR fraction, similar to other cases, was again held at 0.05 to simulate realistic conditions. Cooled EGR at ambient temperature was applied using the same 9 gram/minute fueling rate as previously mentioned. Five hundred cycles were run for varying external EGR rates ranging from 0 to 0.6 (0-36% mass) in order to easily compare the effects of both internal and external EGR. This simulation was run, and the results can be seen in Figures 4.19 and 4.20.

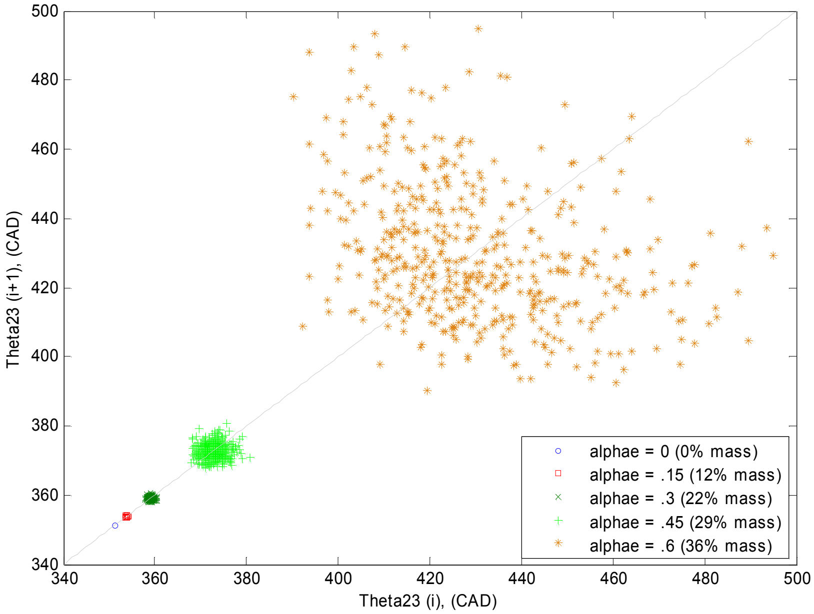

Figure 4.19: θ_{23} Return Map for Varying External EGR Rates: high Tin (9 gpm fuel rate)

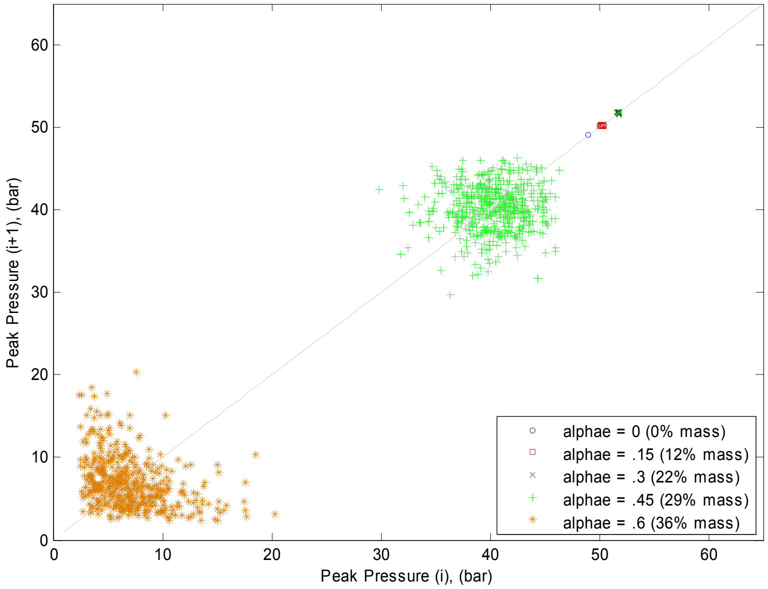

Figure 4.20: Peak Pressure Return Map for Varying External EGR Rates: high Tin (9 gpm fuel rate)

Figures 4.19 and 4.20 reveal some interesting behavior with respect to varying the cool EGR fraction. One observation is the fact that the combustion timing actually retarded with higher amounts of external EGR, whereas the hot internal EGR caused the timing to advance. This behavior makes sense, however, due to the fact that the external EGR is colder than the intake charge. Adding more and more EGR in this case therefore acts to decrease the temperature in the cylinder, which in turn acts to retard the timing. Another interesting observation is the fact that external EGR appears to have a far greater impact on the peak pressure magnitude then the internal EGR. This behavior can be explained by investigating the temperature of the EGR being injected. Since the intake temperature was held at 520K, the cool external EGR therefore had a larger temperature difference and was able to have a greater impact on the timing. The effects of temperature are once again shown to dominate the process. One final observation made here was the fact that the variations in the output variables appear to increase as the external EGR is increased, shown by the larger circles in Figures 4.19 and 4.20. This behavior of increasing cyclic variability with increased EGR has also been observed in the literature [18].

In this case, it was desired to determine the effect of varying the external EGR fraction while the intake temperature was held low, as opposed to being held high in the previous case. In staying consistent with previous tests, the intake temperature for this test was held at 450 K, which was meant to represent a cool intake charge. The internal residual remained at 0.05, and the same fueling rate of 9 grams/minute was again used. The ambient temperature external EGR was again varied between nominal values of 0 and 0.6. The results of this test can be found in Figures 4.21 and 4.22.

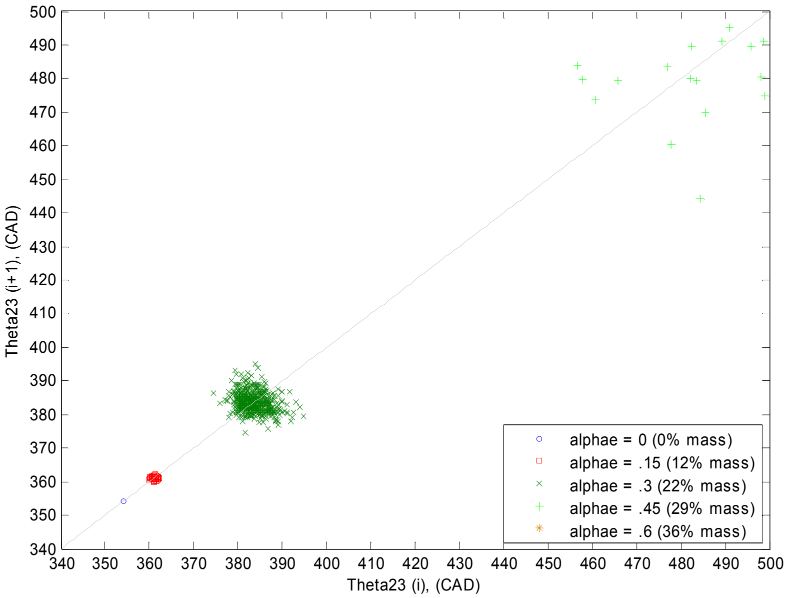

Figure 4.21: θ_{23} Return Map for Varying External EGR Rates: low Tin (9 gpm fuel rate)

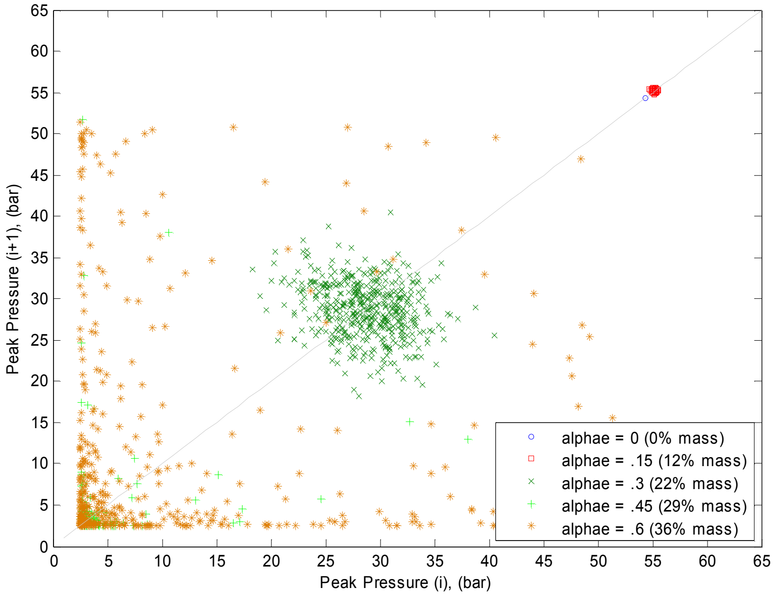

Figure 4.22: Peak Pressure Return Map for Varying External EGR Rates: low Tin (9 gpm fuel rate)

When compared to similar results for internal EGR, Figures 4.21 and 4.22 reveal somewhat different behavior for the case when cool external EGR is applied. The timing, for example, was initially late for the internal EGR and then began to advance slightly as larger amounts of hot residual were added. Figure 4.21, however, reveals that the timing is significantly retarded as cooler external EGR is added. This result makes sense due to the low temperatures seen in the cylinder. The intake temperature is held low, while the cool EGR acts to cool the mixture even further. This cooling effect results in the mixture igniting later. The effect of temperature again seems to dominate the process. Similar to the previous case, these results also seem to suggest that the variability of the outputs increases with increased amounts of cool external EGR.

4.3.2 High Temperature External EGR. In order to fully understand the effect of external EGR on the system, it was desired to increase the temperature of the EGR being added and monitor the effects. The cases which were run at a low external EGR temperature were repeated with the increased temperature in order to isolate the effects of the temperature change. Any differences in the results between the two tests could then be attributed solely to the increase in temperature of the external EGR. The first test which was repeated was the case of varying the intake temperature about a fixed high external EGR rate. The external EGR was held at 0.4, the internal EGR was held at 0.05 and the same fueling rate of 9 grams/minute was used. The intake temperature was varied in exactly the same manner as before, and the test was run for 500 cycles at each temperature. The results can be seen below in Figures 4.23 and 4.24.

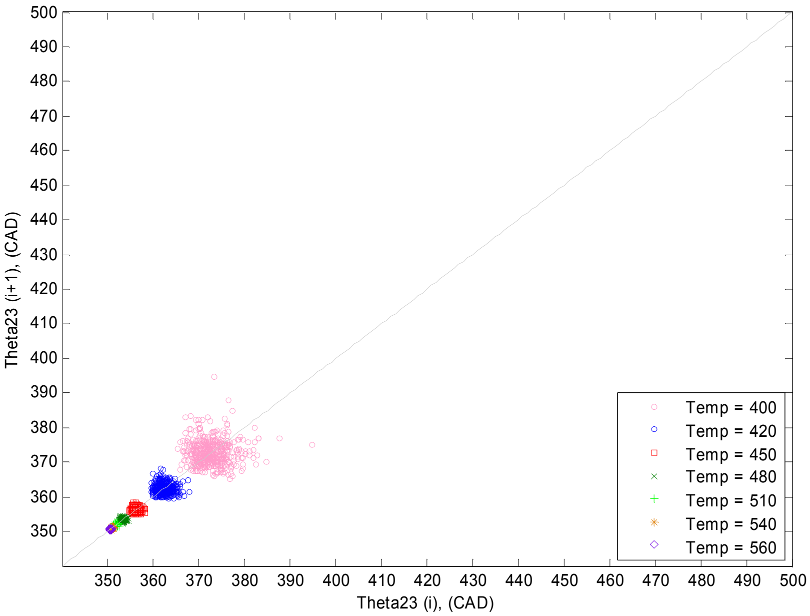

Figure 4.23: θ_{23} Return Map for Varying Intake Temperatures: hot eEGR (9 gpm fuel rate)

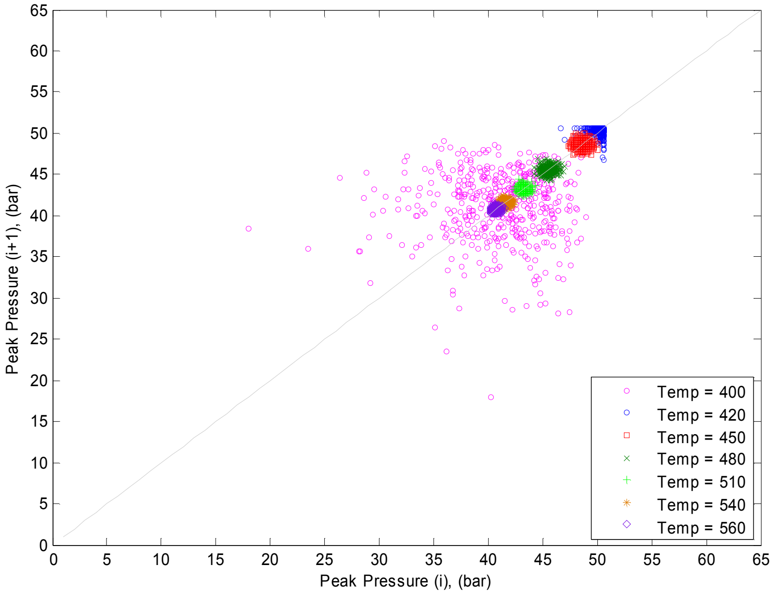

Figure 4.24: Peak Pressure Return Map for Varying Intake Temperatures: hot eEGR (9 gpm fuel rate)

The behavior in Figures 4.23 and 4.24 is strikingly dissimilar from that seen in Figures 4.17 and 4.18 for the case of cool external EGR. The overall behavior is the same for each case, but the combustion timing is drastically advanced for the current case of hot external EGR. This behavior is due to the elevated temperature of the EGR being applied. The intake charge is initially hotter due to the hot EGR, which in turn causes the engine to continue to operate for significantly lower intake temperatures. In fact, the engine still operates for intake temperatures as low as 400K for the elevated temperature EGR, whereas combustion stopped occurring around intake temperatures of 510K for the case of cooled EGR. Another observation deals with the fact that variability seems to decrease for the case of hot external EGR. This is even more evidence that elevated temperatures lead to less variability.

The next case investigated looked at the effects of varying the now hot external EGR about some fixed intake temperature. In order to reproduce the same conditions from the previously run test with cool EGR, this intake temperature was set at 520 K. The internal residual was set at 0.05, again to duplicate the previous test case. The external EGR was varied about the same nominal values, and the simulation was run for 500 cycles. The results of this analysis can be seen in Figures 4.25 and 4.26.

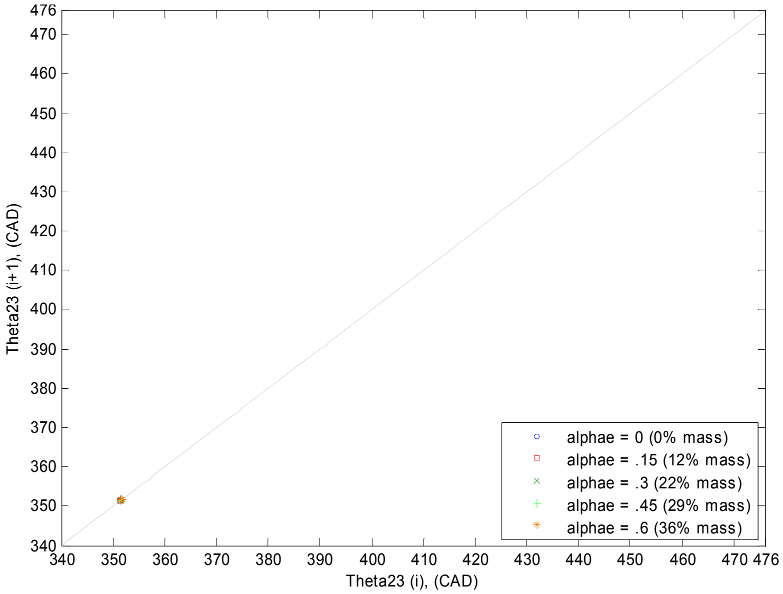

Figure 4.25: θ_{23} Return Map for Varying External EGR Rates: high Tin (9 gpm fuel rate)

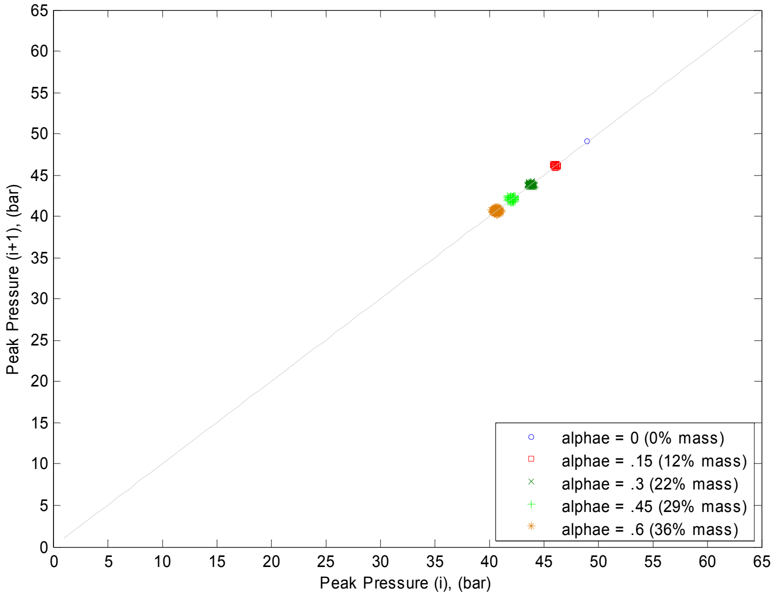

Figure 4.26: Peak Pressure Return Map for Varying External EGR Rates: high Tin (9 gpm fuel rate)

When compared to the case of cool EGR, Figures 4.25 and 4.26 reveal that varying hot external EGR causes the system to behave somewhat differently. For the case of cool EGR, the timing was retarded as the amount of exhaust gas was increased. When hot EGR is applied, however, the timing actually advances as more is added. This behavior is a result of the elevated temperature of the EGR, which acts to increase the overall temperature of the charge and therefore cause combustion to occur earlier. This reversing trend in the combustion timing hints at the idea of a temperature difference effect. While the actual temperature of the EGR itself is important, the difference in temperature between the EGR and the intake air may play a major role in determining the overall behavior of the system. As in previous cases, the variability again increases as more external EGR is applied.

The final test case to be investigated dealt with varying the elevated temperature external EGR about a low intake temperature. This would again allow a comparison of the effects of internal and external EGR. Holding true to a previous case, the intake temperature was again set at 450 K to represent a cool intake charge. The internal residual was set at 0.05 and the same fueling rate of 9 grams/minute was again used. The hot external EGR was varied between the same nominal values as before, and the simulation was run for 500 cycles at each of those values. The results can be seen in Figures 4.27 and 4.28.

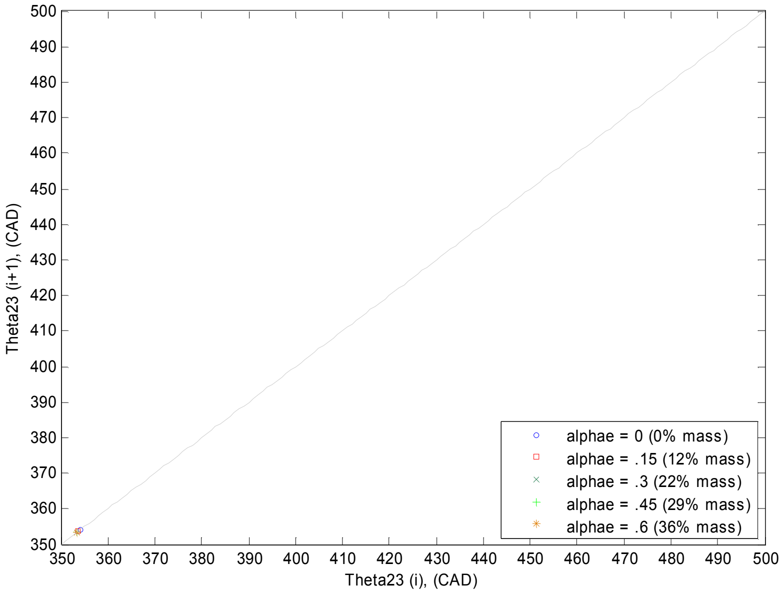

Figure 4.27: θ_{23} Return Map for Varying External EGR Rates: low Tin (9 gpm fuel rate)

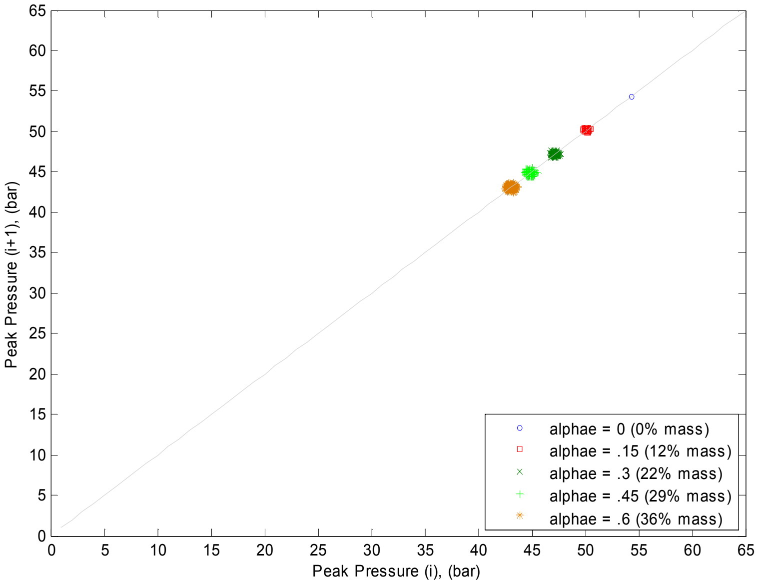

Figure 4.28: Peak Pressure Return Map for Varying External EGR Rates: low Tin (9 gpm fuel rate)

Similar to previous results, Figures 4.27 and 4.28 show that increasing the temperature of the external EGR changes the overall behavior of the system. In fact, these results show that timing and peak pressure behavior are the reverse of what they were in the case of cool EGR. This can again be explained by the heating effect of the external EGR on the intake charge. The hotter exhaust gas heats up the mixture, which then causes combustion to occur sooner rather than later. While the output variability is minimal for a given input, the sensitivity again seems to increase as more external EGR is added. This effect is visible regardless of the temperature of the EGR being applied. In summary, higher temperatures and more advanced combustion timing again seem to reduce variability in the outputs. The temperature difference between the applied external EGR and the intake charge also appears to be significant, in that it affects the overall behavior of the system. Finally, the output variability also seems to increase as the amount of external EGR is increased, regardless of its temperature.

Throughout the entire perturbation analysis, the cyclic coupling was determined to be dominated by temperature effects rather than compositional effects. This was a result of the exponential temperature relation within the Integrated Arrhenius Rate which was used to predict the combustion timing within the model. While compositional effects were also present in the Arrhenius Rate expression, they had a minimal effect on the dynamics of the system, due largely to the assumption of complete combustion at every engine operating condition. If the species present in the intake charge were allowed to vary from cycle to cycle, the effects of composition would most likely have a greater effect on the overall dynamics of the system. To this end, considerations for future work will therefore relax the assumption of complete combustion for very late ignition timings in an attempt to account for misfires and partial burns.

4.4 COMPARISON TO EXPERIMENTAL DATA

One last comparison that needs to be made with respect to this variability analysis is to the experimental data. Any given engine will always experience some level of cyclic variability, which is comparable to the current study being done on the model. In an effort to determine whether the model outputs are behaving similar to the experiment, disturbances were applied to the inputs within the model following the same procedure described above. Since available experimental data utilized variable intake temperatures in order to vary combustion timing, perturbations were therefore applied to the intake temperature within the model in order to make a good comparison. The temperature perturbations were once again defined to be +/- 1 percent of the nominal value, which is representative of the uncertainty associated with resistance heaters. The experiment was run with external EGR shut off, therefore the external EGR was set to zero within the model. The same fueling rate of 9 grams/minute was used in both model and experiment. With all other variables between model and experiment consistent, the intake temperature was varied within the model, and the simulation was run for 500 cycles at each value. These results were plotted against the cyclic experimental data on return maps, and can be seen in Figures 4.29 and 4.30.

These results show that the model effectively captures the overall behavior of the experiment for the case when the intake temperature is varied. Since output variability is in question, however, that is what is focused on. Figures 4.29 and 4.30

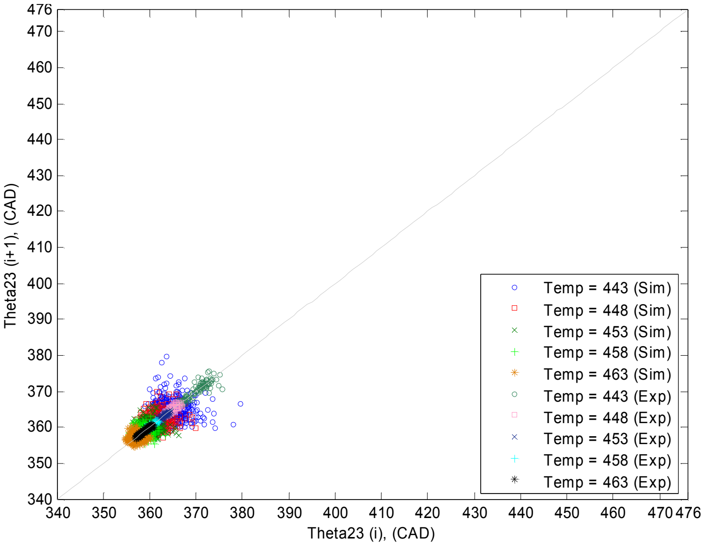

Figure 4.29: θ_{23} Return Map for Varying Intake Temperatures (Exp vs Sim)(9 gpm fuel rate)

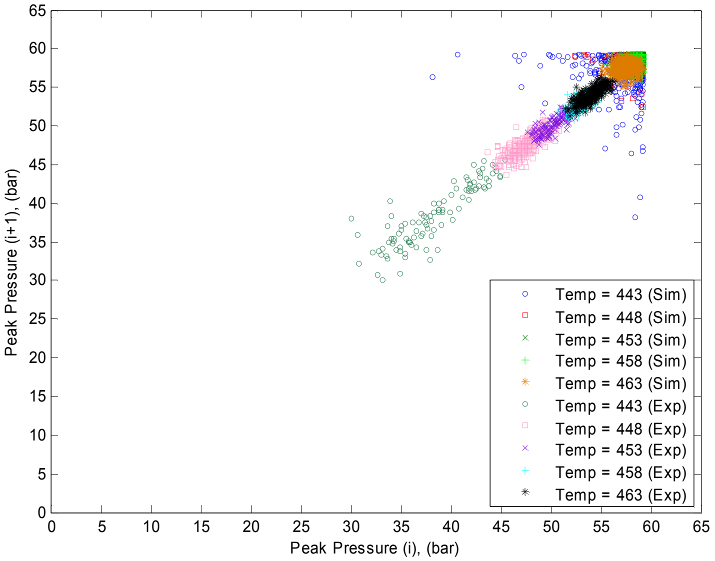

Figure 4.30: Peak Pressure Return Map for Varying Intake Temperatures (Exp vs Sim)
(9 gpm fuel rate)

reveal that the model exhibits a random Gaussian distribution, whereas the experiment seems to exhibit more of a linear distribution. A Gaussian distribution was defined in the model in order to represent random white noise, which is why the marks appear circular in the Figures. The experimental marks, however, appear to be rectangular and seem to follow a somewhat linear path on the return maps in Figures 4.29 and 4.30.

This is most likely due to the variations of experimental intake temperature not being completely random, i.e. they were influenced by some other signal or vibration present on the engine. Despite this influence on the experimental fluctuations, the model and experiment still show reasonable agreement with respect to the output variability.

5. EXTENSION TO OTHER FUELS

For the case when the fuel will remain constant for a certain application, the extension of the model to other fuels reduces to changing the fuel specific parameters within the model, such as the stoichiometry, Arrhenius constants and fuel properties, to match those of the particular fuel being used. If in a particular application, however, the fuel is allowed to vary in real-time, then the extension of the model to multiple fuels now becomes non-trivial. The model must be developed using a certain stoichiometry, and then must detect and adapt to possible fuel changes during operation. If this type of model is to be realized, we must first go back to the experimental data in order to gather as much information as possible so as to get a better understanding of what is physically happening when the fuel is switched in the experiment. Only with this physical insight obtained from running experiments with various fuels can a logical starting place be established for the development of a model with multiple fuel capabilities. The key to arriving at the aforementioned starting point is by answering the question, what physics does the model need to capture in order to be applicable to a number of different fuels?

5.1 EXPERIMENTAL RELATION TO OI

In order to develop a model with multi-fuel capabilities, the experimental data must first be examined for a number of different fuels in order to extract any and all information that may explain the behavior as the fuel is switched. To this end, successful HCCI experiments have been carried out by Jeff Massey at Oak Ridge National

Laboratories using the Hatz 1D50Z CI engine, which span a range of different types of fuels. These fuels included an Unleaded Test Gasoline with a RON of 96, E85, E50, a standard pump gas and a Toluene Reference Fuel (TRF). These fuels, along with their properties, can be seen in Table 5.1.

Table 5.1: Fuel properties

Fuel	**Density** (kg/m^3)	**H/C Ratio**	**MW** (g/mol)	**LHV** (KJ/g)	**$(F/A)_{stoich}$**	**RON**	**MON**
UTG96	0.7405	1.888	105.1	43.077	0.0688	96.4	87.8
E85	0.782	2.45	49.3	31.073	0.0973	113	94
E50	0.7645	2.35	63.74	36.385	0.0737	105	90
Pump Gas	0.74	2.25	114.232	44.4	0.0661	92	82
TRF	0.8123	1.53	75.489	38.633	0.0774	104.2	88.9

Each fuel was run at a fueling rate of 9 grams/minute (ϕ ~ .38), while UTG96 was also run at a fueling rate of 6 grams/minute (ϕ ~ .25). In-cylinder pressure measurements were taken for each fuel, and the results were used to calculate experimental heat release for the various intake temperatures corresponding to each particular fuel. These results can be seen in Figures 5.1-5.6.

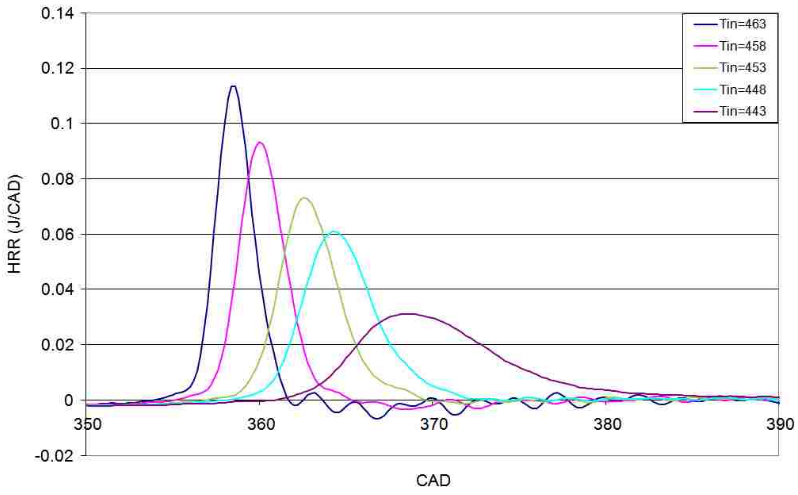

Figure 5.1: Experimental heat release rate for UTG96 (9 g/min fueling rate)

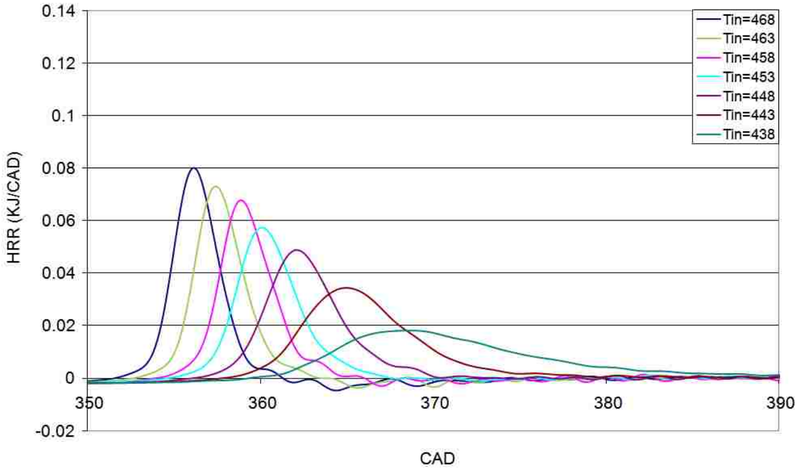

Figure 5.2: Experimental heat release rate for UTG96 (6 g/min fueling rate)

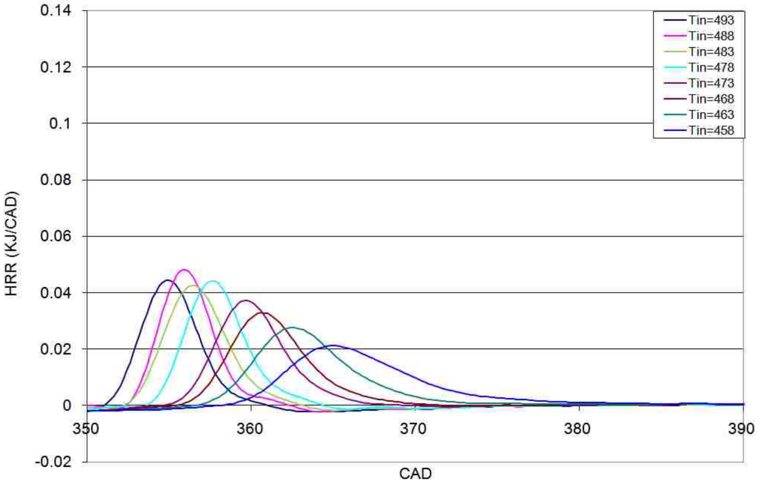

Figure 5.3: Experimental heat release rate for E85 (9 g/min fueling rate)

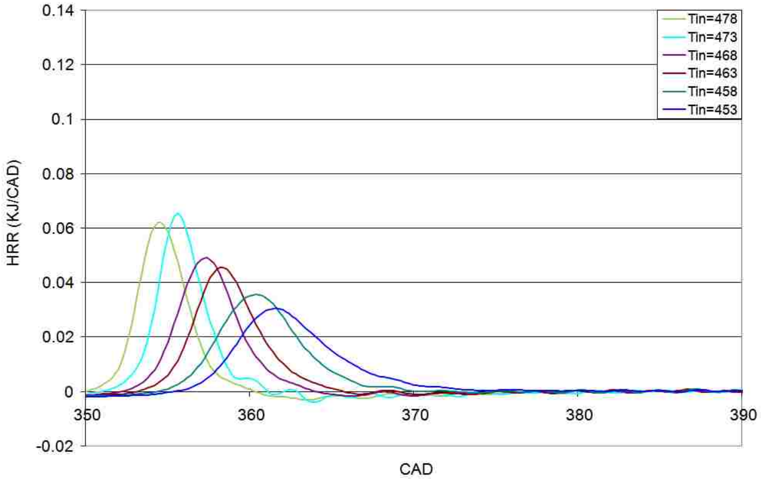

Figure 5.4: Experimental heat release rate for E50 (9 g/min fueling rate)

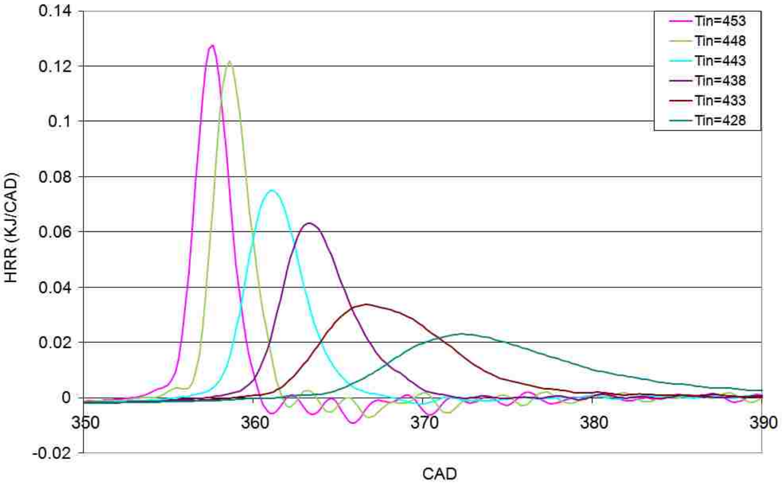

Figure 5.5: Experimental heat release rate for Pump Gas (9 g/min fueling rate)

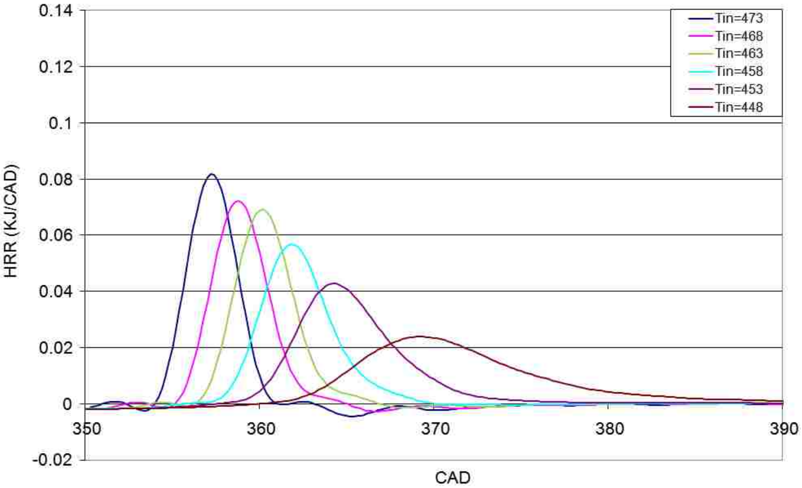

Figure 5.6: Experimental heat release rate for TRF (9 g/min fueling rate)

This heat release rate data was then used to calculate several parameters which were determined to be pertinent to control, such as experimental start of combustion and CA50. These results can be found in Figures 5.7 and 5.8.

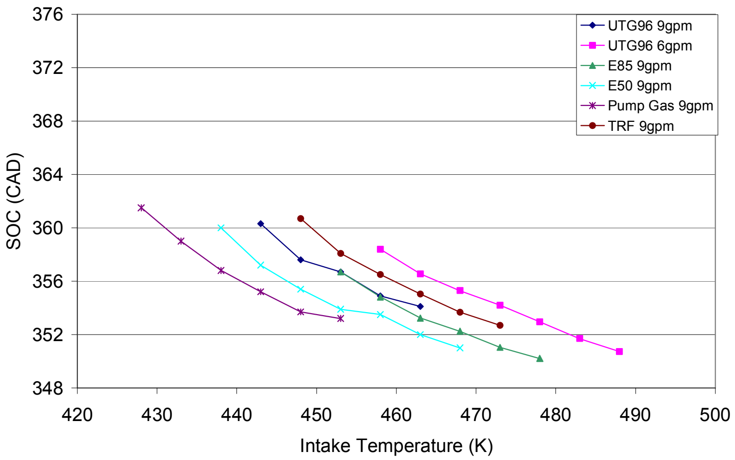

Figure 5.7: Experimental start of combustion values for various fuels and fueling rates

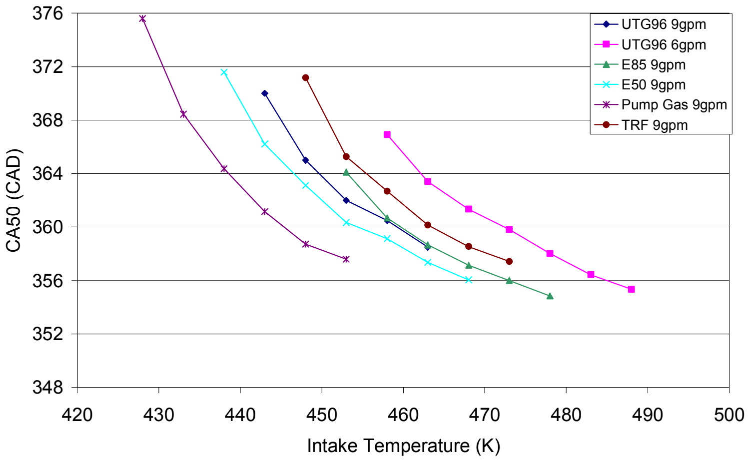

Figure 5.8: Experimental CA50 values for various fuels and fueling rates

The data in these figures represented the experimental temperature ranges between which HCCI operation could be successfully achieved for each fuel. In Figures 5.7 and 5.8, it appeared as though a pattern was developing as the fuel was switched within the experiment. Both the start of combustion and experimental CA50 values seemed to display this pattern, which can be seen as a clear shift in the data as the fuel was varied. In either figure, the general behavior, regardless of which fuel was used, seemed to be to advance the timing as intake temperature was increased. As the fuel type was then changed in the experiment, the same general behavior was again observed, with the only difference being the range of intake temperatures between which that behavior was occurring. In other words, each individual fuel reacted similarly to changes in intake temperature, with the magnitude of that temperature being dependent upon which fuel was being run. Pump gas could be operated at the lowest intake temperatures, followed by E50, then by E85, UTG96 and TRF. The lowered fueling rate case run with UTG96 required the highest intake temperatures in order to achieve HCCI. In each case, both the SOC and CA50 values were similar in magnitude for all the fuels, they were merely shifted farther to the right as the fuel was changed.

With the experimental data for a number of different fuels in hand, the next step was to try and extract any information that would explain the apparent shift in operating range for each fuel. Due to the fact that HCCI combustion is achieved via the auto-ignition of a compressed mixture, it is therefore very similar to knock seen in SI engines as described in previous sections. In SI engines, the knock propensity of a particular fuel is given by its RON (Research Octane Number) and MON (Motor Octane Number) values [34]. These numbers come from standardized tests, and are readily available for a plethora of different fuels. Due to the similarities between HCCI and knock in SI, it therefore makes sense that HCCI combustion may also be somewhat dependent upon these RON and MON values, which are used to describe a fuels “resistance” to auto-ignition. While there is indeed some correlation between the two, previous work has shown that the auto-ignition behavior of different fuels cannot be properly explained by RON or MON on their own in HCCI engines [34]. This arises due to the fact that the RON and MON tests are standardized, which means that they are run using primary reference fuels along with specific engine operating conditions. Since the chemistry of real fuels is quite different from that of primary reference fuels, and the engine operating conditions can vary from those seen in the RON and MON tests, the auto-ignition quality of a fuel cannot be entirely described by RON and MON alone [37]. It turns out, however, that the auto-ignition behavior in HCCI, and therefore the shift seen in Figures 5.7 and 5.8, can be explained more accurately by something called the Octane Index, OI, where OI=RON-KS [34,35,36,37]. In this relationship, S is known as the fuel sensitivity and is given by (RON-MON), while K is independent of the fuel and its value depends only on the operating conditions of the engine. It is this K value that allows the OI to properly describe the auto-ignition quality of fuels in HCCI due to the inclusion of the engine operating conditions. By definition, the higher the OI is for a particular fuel, the higher its "resistance" to auto-ignition.

In an attempt to test the hypothesis that HCCI auto-ignition can be described by the Octane Index, values for the OI were calculated for each fuel using the experimental data from the Hatz engine, along with Kalghatghi's expression below.

$$\begin{aligned} &OI = RON - KS \\ &\qquad \text{where } K = .00497T_{comp15} - .135\lambda - 3.67 \end{aligned} \tag{5.1}$$

In Equation 5.1, the value for K is dependent upon the normalized air/fuel ratio as well as something termed T_{comp15}. This T_{comp15} term is representative of the in-cylinder temperature when the pressure reaches 15 bar during the compression stroke, and is arbitrarily chosen to represent the pressure/temperature history of the mixture [34,36,37]. Since intake temperature was used to adjust the combustion timing on the Hatz engine, this K value, and therefore the OI, will change with engine setpoint due to T_{comp15} being directly affected by the temperature at the start of the compression stroke. Using Equation 5.1, the OI was calculated at each setpoint for each of the different fuels using the fuel properties in Table 5.1, along with the known intake temperatures from the experiment. These results were tabulated and plotted, and can be seen in Table 5.2 and Figures 5.9 and 5.10, respectively.

Table 5.2: Calculated OI values for various fuels at different engine setpoints

UTG96		**E85**		**E50**		**Pump Gas**		**TRF**	
Intake Temp (K)	OI	Intake Temp (K)	OI	Intake Temp (K)	OI	Intake Temp (K)	OI	Intake Temp (K)	OI
463	93.1639	478	102.7524	468	98.4335	453	89.3336	473	96.7952
458	93.5548	473	103.6024	463	99.2611	448	89.7016	468	97.4702
453	93.885	468	104.4933	458	100.2169	443	90.3903	463	98.1622
448	94.5779	463	105.5768	453	100.9225	438	90.7176	458	99.1787
443	94.8303	458	106.5509	448	101.6617	433	91.1573	453	99.1879
		453	107.6018	443	102.2087	428	91.5942	448	100.7974
				438	103.0676				

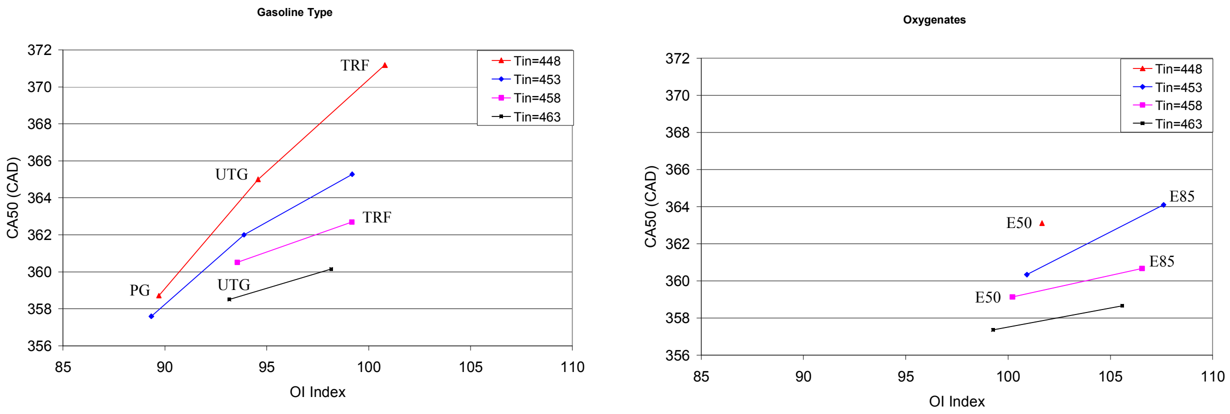

Figure 5.9: Relationship of CA50 to Octane Index at given intake temperatures for gasoline-type and oxygenated fuels

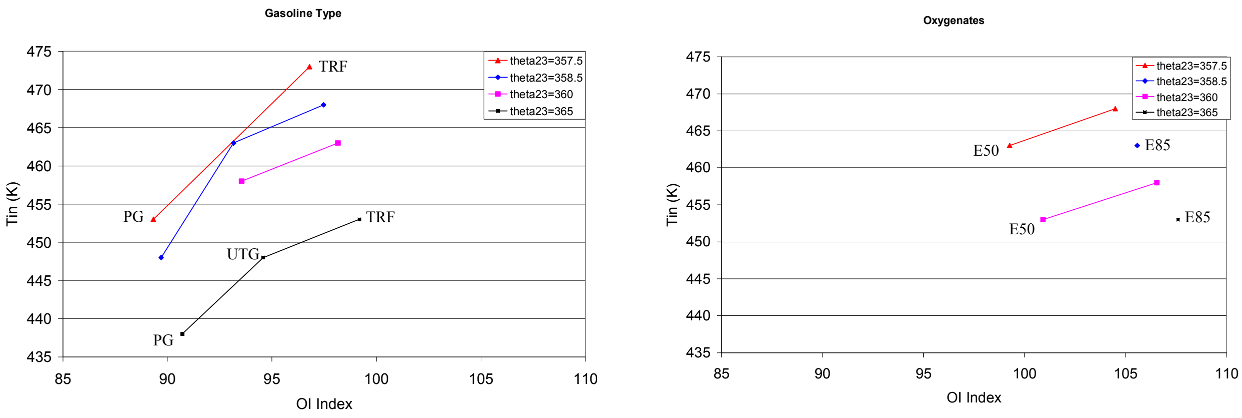

Figure 5.10: Relationship of intake temperature to Octane Index at given CA50 values for gasoline-type and oxygenated fuels

These figures reveal that the auto-ignition quality of the fuels investigated, and therefore at least some of the shift in the data seen in Figures 5.7 and 5.8, can indeed be explained by the OI. Figures 5.9 and 5.10 have been divided into two fuel categories represented by gasoline-type fuels and oxygenated fuels. This treatment was necessary due to the much higher OI ethanol-based fuels resulting in earlier auto-ignition timing than a gasoline-type for a similar intake temperature. This behavior is most likely due to the oxygen content of the ethanol-based fuels, which requires that they be investigated separately in order to eliminate any unknown effects caused by an increased oxygen concentration in the cylinder. In Figure 5.8, it was evident that for a given intake temperature, CA50 is retarded as the fuel is changed in the experiment from Pump Gas to TRF. Figure 5.9 serves to validate this behavior by relating it back to the OI values for the various fuels. In Figure 5.9, it is clear that for a given intake temperature, the CA50 values are increasing as the OI is increased. For each temperature band, the fuel with the lowest OI ignites first, followed by the next lowest OI fuel and so on. Within the 448 K temperature band of Figure 5.9, for example, Pump Gas (OI=89.7) ignites first, followed by UTG96 (OI=94.5) and finally by TRF (OI=100.7). Also evident in Figure 5.9 is the fact that for approximately the same OI, CA50 values are retarded as intake temperature is decreased. In other words, the higher the OI value the more reluctant that particular fuel is to auto-ignite. This ordering predicted by the OI matches that seen in the experiment, which indicates that the OI is indeed providing some correlation between auto-ignition, and the temperatures required to achieve that auto-ignition. Figure 5.10 validates this argument even further by revealing that for a given CA50 that the intake temperature required to achieve that value increases with increasing OI. This behavior again makes physical sense due to the fact that increasing OI results in the fuel becoming more reluctant to auto-ignition, which then requires elevated temperatures in order to maintain the given CA50. Figure 5.10 also reveals that for approximately the same OI, advancing the timing requires increasingly higher intake temperatures in order to achieve. Both of these trends agree well with the experimental data, which provides even more evidence that the OI does indeed provide an explanation for the observed shift in the experimental data when the fuel is changed. In summary, the OI was found to explain the shifts observed in the experimental data, which suggests that the model being developed must therefore capture some sort of information related to the OI in order to successfully achieve multi-fuel capabilities.

5.2 CAPTURING OI INFORMATION IN THE MODEL USING RON AND MON

With the knowledge that the trends in the experimental data for different fuels can be explained using the OI, the next step is to try and incorporate that information into the control model. The model must be able to capture some type of information about the OI so that it will be able to accurately predict engine output parameters if and when the fuel is switched in the engine. With this in mind, a parameter within the model must therefore be chosen which, when altered, will correlate with changes in OI, and therefore the fuel. In addition, this parameter chosen to represent OI within the model should ideally have some sort of physical relationship with the auto-ignition quality of the fuel so as to make a correlation to the OI justifiable. After much deliberation, the parameter chosen from the model to make this correlation was the activation temperature, which is defined to be the activation energy divided by the universal gas constant (E_a/R_u). This activation temperature is one of the Arrhenius parameters, and provides information about the chemical kinetics used within the model via the activation energy, E_a. The activation energy is defined to be the minimum amount of energy necessary in order to start a chemical reaction, which means that a fuel with a higher activation energy correlates to a higher resistance to that fuel undergoing chemical reactions. It is this attribute of the activation energy which allows it to correlate back to the OI for a given fuel. As the activation energy is increased, the fuel will have a higher resistance to chemical reactions, and therefore auto-ignition in the case of HCCI. This behavior mimics that of the OI, which predicts that a higher OI will correspond to a fuel with a higher resistance to auto-ignition, and vice versa. Due to the ability of the activation energy to mimic the behavior of the OI, along with the apparent physical relationship between the two parameters, the activation temperature therefore seems to be a logical parameter to vary within the model in order to account for fuel variability.

In order to utilize the apparent relationship between activation temperature and OI in the model, a mathematical correlation is first needed which is able to relate the widely available RON and MON values used to calculate OI for a fuel to activation temperatures which can then be used within the model. Using 15098 K as the baseline activation temperature correlating to UTG96, along with the calculated OI values in Table 5.2 for the various fuels, the model was calibrated using the experimental data in Figures 5.7 and 5.8. This was done by observing the change in OI between fuels, and then varying the activation temperature within the model accordingly in order to match the predicted θ_{23} values to the corresponding CA50 values from the experiment. This calibration was done for each fuel, and the resulting correlation between the activation temperature and the OI was represented graphically in Figure 5.11.

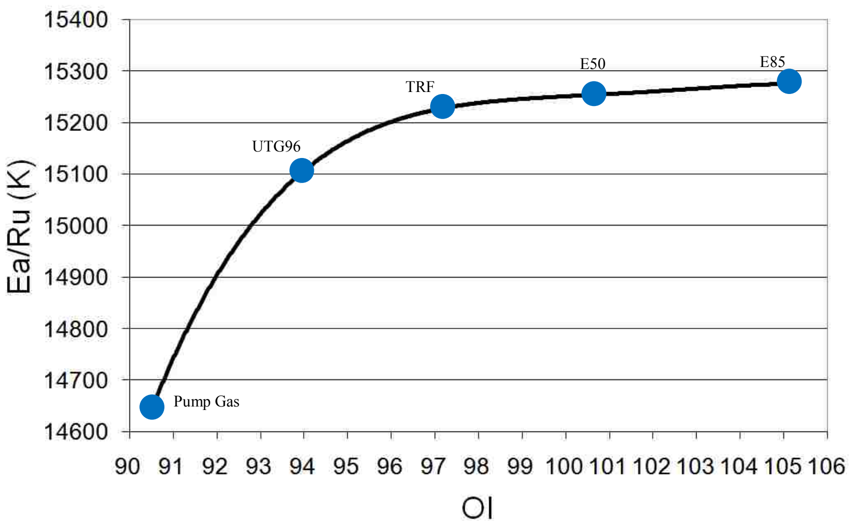

Figure 5.11: Correlation between the activation temperature and OI based on model calibration to match θ_{23} to experimental CA50

In order to be useful in the model, this correlation must first be written in functional form. To accomplish this, a linear regression was done on the data seen in Figure 5.11 and the following power series function was established.

$$\frac{E_a}{R_u} = -.0387(OI)^4 + 15.746(OI)^3 - 2401.493(OI)^2 + 162755.596(OI) - 4120742.23 \qquad (5.2)$$

This experimental correlation provides a link between the readily available RON and MON for various fuels and the Arrhenius activation temperature by means of the OI. While it is understood that the activation temperature is a complex mechanism and is most likely dependent upon a number of variables, it seems to show a fairly strong correlation to the OI. Therefore, since the control model requires that the correlation remain as simple as possible while still capturing the key dynamics of the process, the expression in Equation 5.2 relating activation temperature to OI was developed based on experimental data. This correlation will allow the model to capture information about the fuel using the RON and MON, and then convert that information into an Arrhenius parameter which can be used within the chemical kinetics scheme of the model to predict combustion timing for various fuels. In other words, this correlation will allow the model to compensate for fuel changes by simply tweaking the activation temperature based on the RON and MON of the fuel, while all other parameters remain unchanged.

5.3 APPLYING OI CORRELATION TO PREDICT FUEL CHANGES

Using the correlation from Equation 5.2, the next step was to implement these calculated activation temperatures based on OI into the model in order to determine their ability to mimic the effect of fuel changes, which are evident in Figures 5.7 and 5.8. In order to make a straightforward comparison with the experiment, the activation temperature was modified for each fuel based on its OI and the model was then run through the same set of intake temperatures as the experiment. This analysis would allow for a direct comparison between the experimental results found in Figures 5.7 and 5.8, which display a clear shift in the data as the fuel is changed. This analysis was completed and the model results for SOC are shown in Figure 5.12.

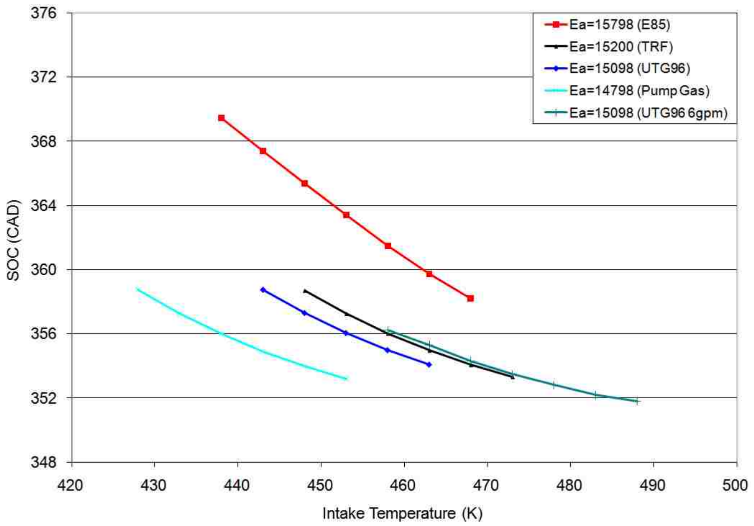

Figure 5.12: Predicted SOC values for various activation temperatures corresponding to the various fuels

This figure contains SOC values predicted by the model as a result of changing only the activation temperature. With the threshold value and fuel properties held constant, the activation temperature was modified to simulate a fuel change and the resulting model was run through a range of intake temperatures. In Figure 5.12, each line represents a different "fuel" similar to the plot of experimental data in Figure 5.7. Since the experimental OI correlation was calibrated using this experimental data, Figures 5.7 and 5.12 should therefore look very similar. If the correlation between OI and activation temperature is indeed functioning properly, the two figures should display the same ranking, or shift, in the lines as the fuel, or in this case the activation temperature, is changed. When these two figures are compared, the model seems to do a very reasonable job of predicting the shifts seen in the experiment, with the exception of the alcohols. The model accurately predicts that pump gas will ignite at the lowest intake temperatures, followed by UTG96 at slightly higher temperatures, then by TRF and finally by the lowered fueling rate of UTG96. The alcohol based fuels, however, are out of place when compared to the experiment. This result is not surprising, however, due to the fact that oxygenated fuels were found to behave differently than gasoline-type fuels with respect to combustion timing and OI in Figures 5.9 and 5.10. Due to the high OI associated with alcohol fuels, the correlation in Equation 5.2 therefore assigns them high activation temperatures. This suggests that higher intake temperatures are required for reactions to occur in these fuels, and results in the uppermost (red) line in Figure 5.12. This line therefore represents predicted SOC values for E85 when activation temperature is used as the sole means of correcting for fuel changes. When compared to the experimental data in Figure 5.7, these SOC values predicted by the model for E85 are significantly different. As a result, the current model is able to accurately predict the ranking of the gasoline-type fuels by means of the activation temperature, but is unable to reproduce the ranking seen in the experimental data with respect to the alcohol fuels. The next logical step is to therefore determine what needs to be captured in the model in order to accurately predict the ranking of both alcohol and gasoline-type fuels.

In order to capture the behavior of the alcohols, some aspect of the model needed to be modified in order to better represent an oxygenated fuel. Since changing the activation temperature alone was not sufficient, it was therefore necessary to modify an additional term which would serve to reveal some sort of fuel specific information to the model. In order to determine which term would reveal the most information, constants related to both the fuel and stoichiometry were individually updated in the model to represent an alcohol-based fuel, E85 in this particular case. After modifying each constant, the model was run for various intake temperatures in order to determine the individual effects of changing each parameter. This process was repeated for each fuel-specific parameter in the model, and the results are shown in Figure 5.13.

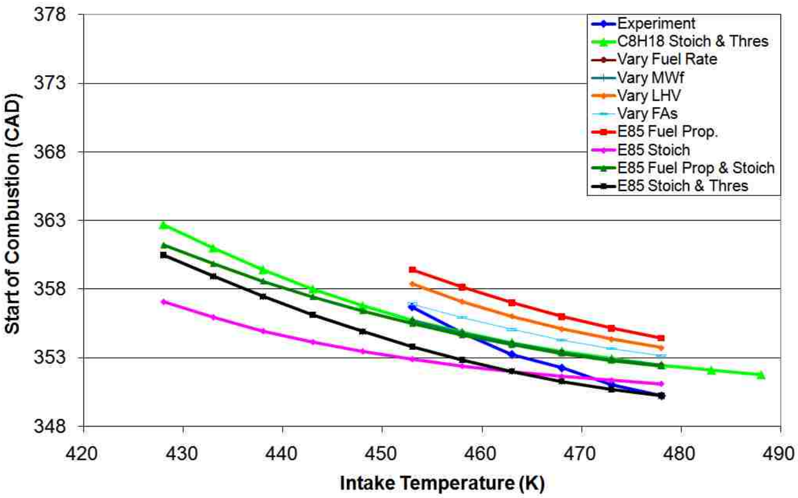

Figure 5.13: Evolution of model SOC from gasoline-type to alcohol stoichiometry

This figure displays the individual effects of modifying fuel specific parameters within the model to represent an alcohol fuel. It displays the entire evolution of the model from a purely gasoline-type stoichiometry to one based on E85. From the previous analysis, it was concluded that the activation temperature alone predicted combustion timing that was significantly retarded from that observed in the experiment with respect to E85. For this reason, the choice fuel parameter must therefore have the ability to advance the timing to better match the experimental data. From Figure 5.13, it is clear that the stoichiometry of the alcohol fuel must be captured in order to advance the timing. In addition to the stoichiometry, a closer inspection reveals that the fuel properties (molecular weight, lower heating value and stoichiometric F/A ratio) must also be accounted for in order to accurately predict the in-cylinder pressure. As a result, it was concluded that the effects of an oxygenated fuel were too complex to capture with a simple parameter, and therefore a separate model was necessary in order to predict the behavior of alcohol-based fuels undergoing HCCI combustion. This new model for alcohol-type fuels was similar to that used for gasoline-type fuels in every way, with the exception of the fuel properties and stoichiometry, which were updated to represent an alcohol.

Due to the alcohol fuels displaying different combustion timing behavior as compared to the gasoline fuels, it was therefore necessary to investigate whether or not the previously developed $\Delta\theta$ correlation was still valid for these fuels. The correlation from Equation 2.60 had been developed based on experimental data corresponding to gasoline-type fuels, and therefore may not apply to alcohol fuels based on the above findings. In order to validate this theory, the experimental data used to develop the correlation was investigated for both gasoline and alcohol fuels. This data can be seen in Figure 5.14.

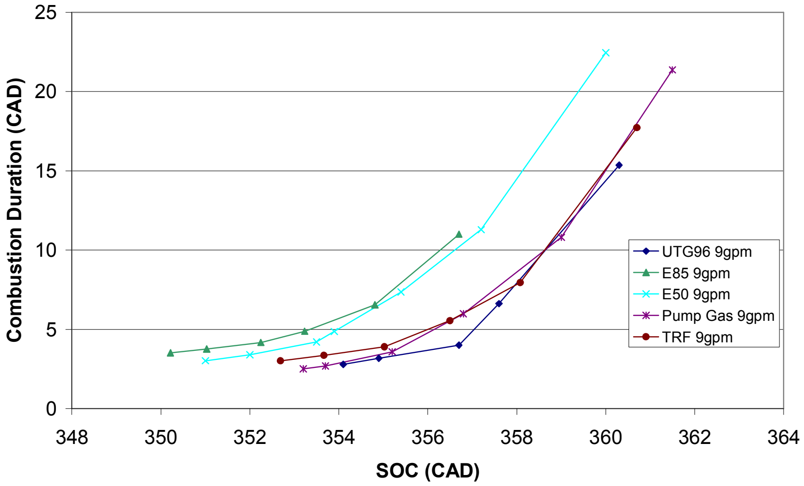

Figure 5.14: Experimental 10-90% burn data for various fuels in HCCI

This figure reveals that the 10-90% burn duration, which was used to develop the Δθ correlation, was indeed behaving differently for oxygenated fuels. While all of the fuels seemed to display a similar trend, the alcohols group was offset from that of the gasoline-type fuels. This behavior again suggested that the oxygen content of the alcohols had some effect on their combustion performance, and also served to verify the hypothesis that a separate Δθ correlation was required to describe these alcohol-type fuels. Using the experimental data in Figure 5.14 for E85, a new experimental Δθ correlation was therefore developed for the oxygenated fuels similar to the one previously developed for the gasoline-type fuels. The form of this correlation was identical to the one for gasoline fuels, with the exception of the constants, which were modified to represent E85.

$$\Delta\theta_{k+1} = \left\lfloor 1.10181\times10^{-35}\left(0.000000062424\right)^{\phi_k}\left(1.002493\right)^{\left(V_1/V_{SOC,k+1}\right)^{\gamma-1}T_{1,k+1}}\left(1.2483169\right)^{\theta_{SOC,k+1}}\right\rfloor \tag{5.3}$$

The correlation in Equation 5.3 could now be integrated directly into the newly developed model for oxygenated fuels, and would allow for a more accurate prediction of θ_{23}. With the development of this correlation, the separate model for oxygenated fuels, which accounted for fuel specific parameters and stoichiometry, as well as burn duration, was now complete. For a given class of fuels, either gasolines or alcohols, the combustion characteristics in HCCI could now be predicted using a universal model for that particular class of fuels.

5.4 MULTI-FUEL VALIDATION WITH EXPERIMENTAL DATA

In order to verify the ability of the two models to predict HCCI behavior for various fuels, it was necessary to compare them to the available experimental data from the Hatz engine. For both the gasoline-type and alcohol fuels, the activation temperature was modified in each code to simulate fuel changes according to the experimental correlation developed in Equation 5.2. For each activation temperature, or “fuel”, the model was run through a range of intake temperatures according to those observed in the experimental data for the respective fuel. The Arrhenius threshold value calculated for UTG96 was held constant for the gasoline-type fuels, while the oxygenated fuels required a different threshold value, which was determined using experimental SOC data corresponding to E85. This analysis was done for all five fuels, and the results, which were grouped according to the fuel class, were plotted along with the experimental data in Figures 5.15-5.17.

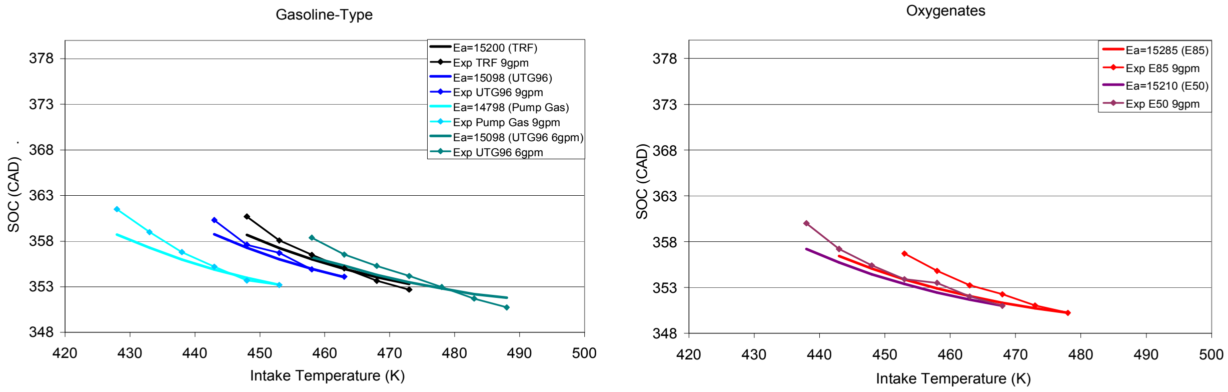

Figure 5.15: Model vs. experimental SOC for gasoline-type and oxygenated fuels

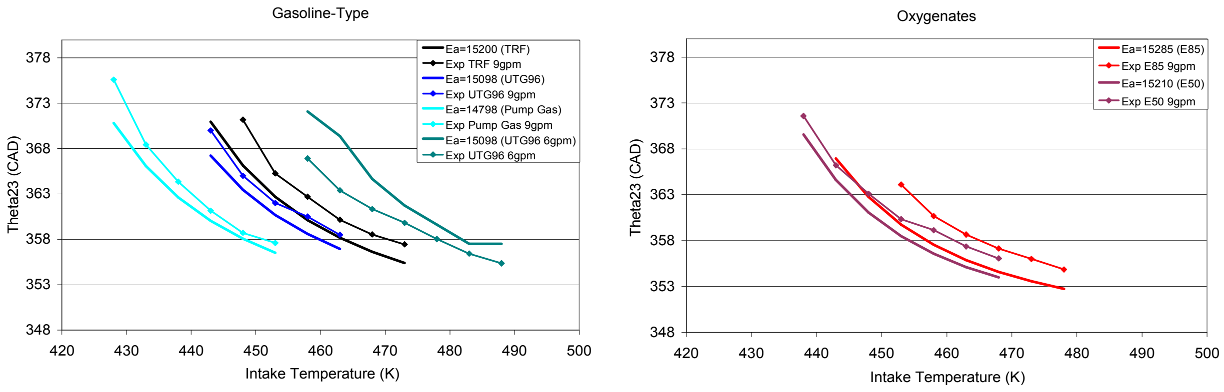

Figure 5.16: Model θ_{23} vs. experimental CA50 for gasoline-type and oxygenated fuels

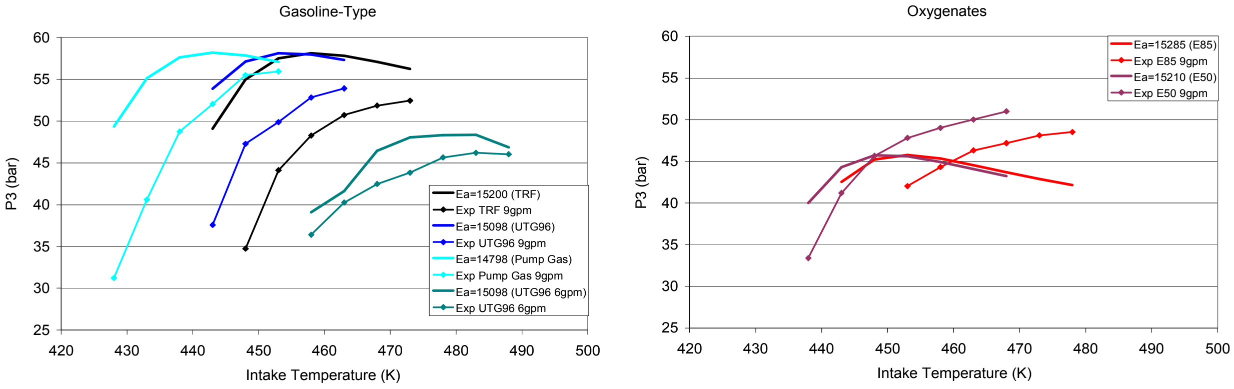

Figure 5.17: Model vs. experimental peak pressure for gasoline-type and oxygenated fuels

These figures reveal that modifying the activation temperature within the model allows it to accurately predict the behavior of a number of different fuels to a level sufficient for control. So long as the proper model is utilized according to the class of fuel being used, a single universal model is able to accurately track the HCCI combustion parameters which are most pertinent to control. This is significant from a controls standpoint due to the fact that the model can be applied to a number of different fuels without having to complete a time intensive calibration process for each one. With knowledge of only the fuel class (gasoline-type or alcohol) and the RON and MON (OI), the appropriate universal model, along with the activation temperature corresponding to the OI of the fuel, can be used to predict the behavior of a plethora of different fuels undergoing HCCI combustion. This ability to use only the OI of a particular fuel to predict its behavior in HCCI, rather than an experimentally intensive engine mapping, allows for a more simplistic model which is ideal for nonlinear control schemes.

6. CONCLUSIONS

Despite the high thermal efficiency and low emissions associated with HCCI, it is inherently difficult to control due to the dependence of the combustion process on chemical kinetics. A control-oriented nonlinear model of the HCCI process is therefore presented, which is based on the underlying physics of the problem. This model is developed in discrete-time by dividing the HCCI process into 5 distinct states, which allows it to be directly applied to state space control methods. The model states are meant to represent parameters with physical significance to the combustion process, and are chosen to be the temperature at IVC, the residual gas fraction and the angle of peak pressure. The outputs from this control model are also meant to represent physical parameters, and are chosen to be the peak pressure, which gives an indication of the work output, and the angle at which that peak pressure occurs. An integrated Arrhenius rate is used to model the HCCI combustion process, which accounts for the effects of both temperature and reactant concentrations on the auto-ignition process. This combustion model predicts the onset of combustion based on an empirically determined threshold value, which is representative of the concentration of fuel which must be destroyed prior to ignition. A variable combustion duration is also utilized within this combustion model, which allows the duration of combustion to vary with set point. The model developed was validated against experimental data from an engine running on a UTG96 RON fuel at two different fueling rates. It was shown to successfully track the pressure evolution in the cylinder for both fueling conditions. The simple model also captures the correct trend in both the start of combustion and the location of peak pressure as the intake temperature is varied, which is crucial for its application to control. Utilizing the relationship between the OI of a particular fuel and its corresponding SOC values, the model was also shown to reasonably predict the trends in both peak pressure and θ_{23} for a number of different gasoline-type fuels. Despite the availability of various control approaches, the nonlinear model presented here is developed primarily for application to nonlinear control. While linearized models provide simplicity, they are only valid around some nominal operating point, which is not characteristic of HCCI engines which regularly change set point. A nonlinear model such as this one is able to retain system nonlinearities over a wider range of operating conditions. The result of this modeling process is therefore a discrete-time nonlinear control model which provides a platform for developing and validating various nonlinear state-space control strategies.

APPENDIX A

HCCI CONTROL MODEL CODE

This appendix contains the HCCI control code which has been discussed in this thesis, and which was developed using MATLAB R2008b. The m-file goes as follows:

```
% This code is a physics based control model for HCCI combustion of
% gasoline-type fuels.
%
% This code uses the integrated arrhenius rate combustion model and its
% parameters in order to predict combustion phasing.
%
% This code includes both heated internal EGR (alphai) and cooled external
% EGR (alphae)
%
% This code uses C7H16 as the operating fuel.
%
% The combustion parameters used are from Turns.
```

Control Model Code

```
cycles=25;                % # times to loop program (engine cycles)

%----------Define Variable Matrices-------------

P1=zeros(1, cycles);
V1=zeros(1, cycles);
T1=zeros(1, cycles);
P2=zeros(1, cycles);
T2=zeros(1, cycles);
T3=zeros(1, cycles);
P3=zeros(1, cycles);       % P3 in cycle, as opposed to output
V4=zeros(1, cycles);
T4=zeros(1, cycles);
P4=zeros(1, cycles);
T5=zeros(1, cycles);
P5=zeros(1,cycles);
T6=zeros(1, cycles);
P6=zeros(1,cycles);

alphae=zeros(1,cycles);
alphai=zeros(1,cycles);
Tin=zeros(1,cycles);
gpm=zeros(1,cycles);
N2=zeros(1, cycles);
N3=zeros(1, cycles);
z=zeros(1, cycles);
Psoc=zeros(1,cycles);
Tsoc=zeros(1,cycles);
Nt=zeros(1,cycles);
Xegr=zeros(1,cycles);
Negr=zeros(1,cycles);
Niegr=zeros(1,cycles);
Nfs=zeros(1,cycles);
PRR=zeros(1, cycles);
V23=zeros(1, cycles);
T1up=zeros(1, cycles);     % Predicts T1 for the next cycle
alphaiup=zeros(1,cycles);
P3op=zeros(1, cycles);     % output P3, as opposed to P3 in cycle
PRRop=zeros(1,cycles);
theta23=zeros(1, cycles);
theta23op=zeros(1,cycles);
W34op=zeros(1, cycles);
Wigef=zeros(1, cycles);
```

```
%-----------Inputs-----------

% alphae=0;         % external EGR
% Tin=460;          % pre-heated intake temperature (K)
% gpm=9;            % fueling rate (gram/min)


%-----------Constants-----------

MWf=100.203;            % molecular weight of fuel (g/mol)
MWa=29;                 % molecular weight of air (g/mol)
FAs=.06634;             % stoichiometric fuel/air ratio
LHV=4501.72;            % LHV of C8H18 (kJ/mol fuel)
LHV2=44.926;            % LHV of C8H18 (KJ/g fuel)
N=188.49555921539;      % engine speed (rad/sec)
s=7.0;                  % stroke (cm)
l=11.042;               % connecting rod length (cm)
bore=9.6999;            % bore diamater (cm)
crank=3.5;              % crank radius (cm)
R=l/crank;
rc=14.5;                % compression ratio
thetaEVO=476*pi/180;    % radians
thetaTDC=360*pi/180;    % radians
thetaLOW=320*pi/180;    % radians
thetaIVO=704*pi/180;    % radians
thetaIVC=228*pi/180;    % radians

Tref=298;               % reference temp corresponding to heat of formation (K)
Tegr=300;               % temperature of cooled EGR (K)
Pin=.0101;              % atmospheric pressure (kN/cm^2)

Vd=pi()*(bore^2)*0.25*s;% disp vol (cm^3)
Vc=Vd/(rc-1);           % clearance vol=V(TDC)=V(360) (cm^3)
Vivc=492.9781;          % (cm^3)
Vevo=444.1483;          % (cm^3)
Vivo=51.4562;           % (cm^3)
Vbdc=Vd+Vc;             % (cm^3)

Cpc7h16R=.224076;       % spec. heat of fuel in reactants (kJ/molfuel*K)
Cpo2R=.030481;          % spec. heat of O2 in reactants (kJ/molO2*K)
Cpn2R=.029414;          % spec. heat of N2 in reactant (kJ/molN2*K)
Cpco2P=.050523;         % spec heat of CO2 in reinducted products (kJ/molCO2*K)
Cph20P=.0381;           % spec heat of H2O in reinducted products (kJ/molH2O*K)
Cpn2P=.031091;          % spec heat of N2 in reinducted products (kJ/molN2*K)
Cpo2P=.033376;          % spec heat of O2 in reinducted products (kJ/molO2*K)
Cpn2E=.029075;          % spec heat of N2 in cooled external EGR (kJ/molO2*K)

gamma=1.3;              % spec. heat ratio of fuel

A=5.1e11;               % Arrhenius rate pre-exponential factor (gmol/cm^3)^1-a-b/s
Ea=15098;               % activation energy (K)
a=0.25;                 % Arrhenius rate parameter (unitless)
b=1.5;                  % Arrhenius rate parameter (unitless)
Kth=2.3072e-6;          % Arrhenius threshold value (gmol/cm^3)

Ru1=.008314472;         % universal gas constant (KJ/mol*K)
Ru2=.8314472;           % universal gas constant (Kn-cm/mol*K)

X=0.86;                 % relationship between temperature of re-inducted
                        % products and exhaust temperature of
                        % last cycle where Treinduct=XTex
eps=0.1;                % fraction of LHV representing heat loss due to combustion
```

```
%-----------Assumptions-----------

offset=120.249*(pi/180);    % Offset value that corrects for the Arrhenius
                            % threshold value not being evaluated with
                            % constant temperatures

%-----------Initializations-----------

T6(1,2)=742;            % temp of inducted products and reactants from "zeroth" cycle (K)
thetaSOC(1,3)=354*pi/180;            % angle at which combustion initiates (radians)
Vsoc(1,3)=(Vc*(1+0.5*(rc-1)*(R+1-cos(thetaSOC(1,2))-...
    (R^2-sin(thetaSOC(1,2))^2)^.5)));
dtheta(1,3)=11*pi/180;                % combustion duration
theta23(1,3)=365*pi/180;  % angle at which peak pressure is assumed to occur (radians)
V23(1,3)=(Vc*(1+0.5*(rc-1)*(R+1-cos(theta23(1,2))-...
    (R^2-sin(theta23(1,2))^2)^.5)));    % cylinder vol at peak pressure (cm^3)


PHI(1,1)=.384563;           % initializes the equivalence ratio
PHI(1,2)=.384563;

Nf(1,2)=.000058;            % initializes the moles of fuel inducted
Na(1,2)=.003;               % initializes the moles of air inducted
alphai(1,3)=.0299;          % initializes the internal EGR(valve overlap and
trapped residual)

alphae(1,1)=0;
alphae(1,2)=0;              % initializes the external EGR
alphae(1,3)=0;

C1(1,2)=1.8614;
C2(1,2)=2.0053;
Cegr(1,2)=1.7411;           % initializes the specific heat parameters
C3(1,2)=1770.1;
C4(1,2)=2.0053;


%-----------Begin Looping the Program---------------

for i=3:cycles;

      % Input values for the intake temperature
            Tin(1,i)=463;

                    % Gives gaussian distributed random values for Tin
    %                     Tin(1,i) = normrnd(443,4.43);

      % Input values for the external EGR
            alphae(1,i)=0;

                    % Gives gaussian disributed random values for alphae
    %                     alphae(1,i) = normrnd(0,.0001);

      % Input values for the fueling rate
            gpm(1,i)=9;

                    % Gives gaussian disributed random values for gpm
    %                     gpm(1,i) = normrnd(9,.27);
```

```
%-----------1: Adiabatic Induction, Instant Mixing-----------
    P1(1,i)=Pin;
    V1(1,i)=(Vc*(1+0.5*(rc-1)*(R+1-cos(thetaIVC)-(R^2-sin(thetaIVC)^2)^.5)));

        if i==3;
            T1(1,i)=T6(1,2);
        else
            T1(1,i)=T6(1,i-1);
        end

    %-----------1-2: Isentropic Compression-----------
    P2(1,i)=(P1(1,i)*((V1(1,i)/V23(1,i))^gamma));
    T2(1,i)=(T1(1,i)*((V1(1,i)/V23(1,i))^(gamma-1)));
    Psoc(1,i)=(P1(1,i)*((V1(1,i)/Vsoc(1,i))^gamma));
    Tsoc(1,i)=(T1(1,i)*((V1(1,i)/Vsoc(1,i))^(gamma-1)));


    %-----------Intermediate Calculations-----------------

    N2(1,i)=(PHI(1,i-1)+52.36+(alphai(1,i)*((4*PHI(1,i-2))+52.36))+...
      (alphae(1,i-1)*(PHI(1,i-1)+52.36))); % number of moles before combustion

    N3(1,i)=((4*(PHI(1,i-1)+(PHI(1,i-2)*alphai(1,i))))+52.36*...
      (1+alphai(1,i))+(alphae(1,i-1)*(PHI(1,i-1)+52.36))); % number of moles after
                                                           % combustion

    z(1,i)=N3(1,i)/N2(1,i);  % product to reactant molar ratio for combustion reaction


    %-----------2-3: Isochoric Combustion-----------
    % Assume instantaneous, constant volume combustion
    T3(1,i)=((C3(1,i-1)+((C1(1,i-1)+(C2(1,i-1)*alphai(1,i))+(Cegr(1,i-1)*...
        alphae(1,i-1))-(Ru1*N2(1,i)))*T2(1,i))-((C1(1,i-1)-C4(1,i-1))*...
        Tref))/((C2(1,i-1)*(alphai(1,i)))+(Cegr(1,i-1)*alphae(1,i-1))+...
        C4(1,i-1)-(Ru1*N3(1,i))));

    P3(1,i)=(z(1,i)*((V1(1,i)/V23(1,i))^gamma)*((C1(1,i-1)+(C2(1,i-1)*...
        alphai(1,i))+(Cegr(1,i-1)*alphae(1,i-1))-(Ru1*N2(1,i)))/...
        ((((C2(1,i-1)*(alphai(1,i)))+(Cegr(1,i-1)*alphae(1,i-1))+...
        C4(1,i-1)-(Ru1*N3(1,i)))*T3(1,i))-C3(1,i-1)+((C1(1,i-1)-...
        C4(1,i-1))*Tref)))*Pin*T3(1,i));


      %-------------Pressure Rise Rate---------------
         PRR(1,i)=((P3(1,i)-Psoc(1,i))*2*pi*100)/(dtheta(1,i)*360);   % (bar/CAD)



    %-----------3-4: Isentropic Expansion-----------
    V4(1,i)=(Vc*(1+0.5*(rc-1)*(R+1-cos(thetaEVO)...
        -sqrt(R^2-sin(thetaEVO)^2))));


    T4(1,i)=(T3(1,i)*((V23(1,i)/V4(1,i))^(gamma-1)));
    P4(1,i)=(P3(1,i)*((V23(1,i)/V4(1,i))^gamma));


    %-----------4-5: Isentropic Exhaust-----------
    T5(1,i)=(T4(1,i)*((Pin/P4(1,i))^((gamma-1)/gamma)));
    P5(1,i)=Pin;
```

```
                %%---------This section calculates the residual mass
                % fraction trapped in the cylinder

                    w=30;                    % engine speed (rev/sec)
                    rc=14.5;                 % compression ratio
                    Pi=1.02235;              % intake pressure
                    Pe=1.24596;              % exhaust pressure
                    B=96.999;                % bore diamater (mm)
                    Dv=31;                   % average valve seat diameter (mm)
                    Lv=5.334;                % average valve lift (mm)
                    IVO=704;                 % intake valve opening (CAD)
                    EVC=20;                  % exhaust valve closing (CAD)
                    thetaoverlap=36;         % valve overlap EVC-IVO (CAD)


                   %----------- Calculate the Overlap Factor OF-----------

               OF = (1.45/B)*(107+7.8*thetaoverlap+(thetaoverlap^2))*((Lv*Dv)/B^2);


                   %------------ Calculate the residual mass fraction --------

                      alphai(1,i+1) = ((.401*(OF/w)*(1-exp((-4.78*(1-...
                          ((Pi/Pe)^.7)))-(153.8*(1-((Pi/Pe)^4.5)))))*...
                          (Pe/Pi)*(Tin(1,i)/T5(1,i)))+((Pe*Tin(1,i))/...
                          (rc*Pi*T5(1,i))));


              %-----------Calculate Air Inducted and Equivalence Ratio---------

                   Nf(1,i)=(gpm(1,i)*4*pi)/(MWf*N*60);           % moles of fuel
                   Nt(1,i)=(Pin*(Vd+Vc))/(Ru2*Tin(1,i));
                   Xegr(1,i)=(alphae(1,i)*(PHI(1,i-1)+52.36))/...
                       (((PHI(1,i-1)+52.36)*(1+alphae(1,i)))+(alphai(1,i+1)*...
                       ((15*PHI(1,i-1))+41.36+(11*(1-PHI(1,i-1))))));
                   Negr(1,i)=Xegr(1,i)*Nt(1,i);                   % moles of egr
                   Niegr(1,i)=alphai(1,i+1)*Nt(1,i);

                      if alphae(1,i)~=0
                          Na(1,i)=Nt(1,i)-Negr(1,i)-Niegr(1,i);
                      else
                          Na(1,i)=(Pin*Vd)/(Ru2*Tin(1,i));
                      end

                    Nfs(1,i)=(Na(1,i)*MWa*FAs)/(MWf);     % stoich moles of fuel
                    PHI(1,i)=Nf(1,i)/Nfs(1,i);            % equiv. ratio


C1(1,i)=PHI(1,i)*Cpc7h16R+11*Cpo2R+41.36*Cpn2R;   % "specific heat" of reactants
C2(1,i)=7*PHI(1,i-1)*Cpco2P+8*PHI(1,i-1)*Cph20P+...
      41.36*Cpn2P+11*(1-PHI(1,i-1))*Cpo2P;        % "specific heat" of products
Cegr(1,i)=(PHI(1,i)+52.36)*Cpn2E;                 % "specific heat" of cooled EGR
C3(1,i)=PHI(1,i)*LHV*(1-eps);
C4(1,i)=7*PHI(1,i)*Cpco2P+8*PHI(1,i)*Cph20P+41.36*Cpn2P+11*(1-PHI(1,i))*Cpo2P;
```

```
%-----------State Update Equations-----------


    T1up(1,i+1)=((C1(1,i)*Tin(1,i)+(C2(1,i)*alphai(1,i+1)*X*((((((C2(1,i-1)*...
        (alphai(1,i)))+(Cegr(1,i-1)*alphae(1,i-1))+C4(1,i-1)-(Ru1*N3(1,i)))*...
        T1(1,i))/(z(1,i)*(V1(1,i)/V23(1,i))*(C3(1,i-1)+((C1(1,i-1)+(C2(1,i-1)*...
        alphai(1,i))+(Cegr(1,i-1)*alphae(1,i-1))-(Ru1*N2(1,i)))*(T1(1,i)*...
        ((V1(1,i)/V23(1,i))^(gamma-1))))-((C1(1,i-1)-C4(1,i-1))*Tref))))^...
        ((gamma-1)/gamma))*((C3(1,i-1)+((C1(1,i-1)+(C2(1,i-1)*alphai(1,i))+...
        (Cegr(1,i-1)*alphae(1,i-1))-(Ru1*N2(1,i)))*(T1(1,i)*((V1(1,i)/...
        V23(1,i))^(gamma-1))))-((C1(1,i-1)-C4(1,i-1))*Tref))/((C2(1,i-1)*...
        (alphai(1,i)))+(Cegr(1,i-1)*alphae(1,i-1))+C4(1,i-1)-(Ru1*...
        N3(1,i))))))+(Cegr(1,i)*alphae(1,i)*Tegr))/(C1(1,i)+(C2(1,i)*...
        alphai(1,i+1))+(Cegr(1,i)*alphae(1,i))));      % state update equation


       thetaSOC(1,i+1)=((((Kth*N)/(A*(PHI(1,i)^a)*((11*((alphai(1,i+1)*...
           (1-PHI(1,i-1)))+1))^b)))*((Vc*Ru2/Pin)^(a+b))*(((T1up(1,i+1)*...
           (PHI(1,i)+52.36+(alphai(1,i+1)*((4*PHI(1,i-1))+52.36))+...
           (alphae(1,i)*(PHI(1,i)+52.36))))/(V1(1,i)))^(a+b)))/...
           (exp(-Ea/(T1up(1,i+1)*((V1(1,i)/Vc)^(gamma-1))))))+thetaIVC+offset;


       Vsoc(1,i+1)=(Vc*(1+0.5*(rc-1)*(R+1-cos(thetaSOC(1,i+1))-(R^2-...
           sin(thetaSOC(1,i+1))^2)^.5)));  % predicts volume at SOC for next cycle


             % variable combustion duration for 10-90% MFB
                % predicts the combustion duration using equivalence ratio,
                % thetaSOC and temperature at SOC
                    dtheta(1,i+1)=((2.067699188524e-18)*(.000351554746669643^...
                       PHI(1,i))*(.992961372838845^(((V1(1,i)/Vsoc(1,i+1))^...
                       (gamma-1))*T1up(1,i+1)))*(1.16093520650449^...
                       (thetaSOC(1,i+1)*(180/pi))))*(pi/180);


       theta23(1,i+1)=((((Kth*N)/(A*(PHI(1,i)^a)*((11*((alphai(1,i+1)*...
           (1-PHI(1,i-1)))+1))^b)))*((Vc*Ru2/Pin)^(a+b))*(((T1up(1,i+1)*...
           (PHI(1,i)+52.36+(alphai(1,i+1)*((4*PHI(1,i-1))+52.36))+...
           (alphae(1,i)*(PHI(1,i)+52.36))))/(V1(1,i)))^(a+b)))/(exp(-Ea/...
           (T1up(1,i+1)*((V1(1,i)/Vc)^(gamma-1))))))+dtheta(1,i+1)+...
            thetaIVC+offset;                             % state update equation


      V23(1,i+1)=(Vc*(1+0.5*(rc-1)*(R+1-cos(theta23(1,i+1))-(R^2-...
          sin(theta23(1,i+1))^2)^.5)));  % predicts volume at theta23 for next cycle


      alphaiup(1,i+1) =(.091255843297*Tin(1,i))/((((((C2(1,i-1)*...
          (alphai(1,i)))+(Cegr(1,i-1)*alphae(1,i-1))+C4(1,i-1)-(Ru1*...
          N3(1,i)))*T1(1,i))/(z(1,i)*(V1(1,i)/V23(1,i))*(C3(1,i-1)+...
          ((C1(1,i-1)+(C2(1,i-1)*alphai(1,i))+(Cegr(1,i-1)*alphae(1,i-1))-...
          (Ru1*N2(1,i)))*(T1(1,i)*((V1(1,i)/V23(1,i))^(gamma-1))))-...
          ((C1(1,i-1)-C4(1,i-1))*Tref))))^((gamma-1)/gamma))*((C3(1,i-1)+...
          ((C1(1,i-1)+(C2(1,i-1)*alphai(1,i))+(Cegr(1,i-1)*alphae(1,i-1))-...
          (Ru1*N2(1,i)))*(T1(1,i)*((V1(1,i)/V23(1,i))^(gamma-1))))-...
          ((C1(1,i-1)-C4(1,i-1))*Tref))/((C2(1,i-1)*(alphai(1,i)))+...
          (Cegr(1,i-1)*alphae(1,i-1))+C4(1,i-1)-...
          (Ru1*N3(1,i)))));                               % state update equation
```

```
        %-----------Output Equations-----------


        P3op(1,i)=(z(1,i)*(V1(1,i)/V23(1,i))*Pin*((C3(1,i-1)+((C1(1,i-1)+...
            (C2(1,i-1)*alphai(1,i))+(Cegr(1,i-1)*alphae(1,i-1))-(Ru1*N2(1,i)))*...
            (T1(1,i)*((V1(1,i)/V23(1,i))^(gamma-1))))-((C1(1,i-1)-C4(1,i-1))*...
            Tref))/(((C2(1,i-1)*(alphai(1,i)))+(Cegr(1,i-1)*alphae(1,i-1))+...
            C4(1,i-1)-(Ru1*N3(1,i)))*T1(1,i))));                 % output equation



        theta23op(1,i)=((((Kth*N)/(A*(PHI(1,i-1)^a)*((11*((alphai(1,i)*...
            (1-PHI(1,i-2)))+1))^b)))*((Vc*Ru2/Pin)^(a+b))*(((T1(1,i)*...
            (PHI(1,i-1)+52.36+(alphai(1,i)*((4*PHI(1,i-2))+52.36))+...
            (alphae(1,i-1)*(PHI(1,i-1)+52.36))))/(V1(1,i)))^(a+b)))/...
            (exp(-Ea/(T1(1,i)*((V1(1,i)/Vc)^(gamma-1))))))+dtheta(1,i)+...
            thetaIVC+offset;                                      % output equation


        PRRop(1,i)=((P3(1,i)-Psoc(1,i))*2*pi*100)/(dtheta(1,i)*360);  % ouput equation


        W34op(1,i)=((((V4(1,i)*((V23(1,i)/V4(1,i))^gamma))-V23(1,i))*(z(1,i)*...
            (V1(1,i)/V23(1,i))*Pin*(C3(1,i-1)+((C1(1,i-1)+(C2(1,i-1)*...
            alphai(1,i))+(Cegr(1,i-1)*alphae(1,i-1))-(Ru1*N2(1,i)))*(T1(1,i)*...
            ((V1(1,i)/V23(1,i))^(gamma-1))))-((C1(1,i-1)-C4(1,i-1))*Tref)))+...
            (Pin*((V23(1,i)*((V1(1,i)/V23(1,i))^gamma))-V1(1,i)+((1-gamma)*...
            (V1(1,i)-V4(1,i)))))*((((C2(1,i-1)*(alphai(1,i)))+(Cegr(1,i-1)*...
            alphae(1,i-1))+C4(1,i-1)-(Ru1*N3(1,i)))*T1(1,i)))))/((((C2(1,i-1)*...
            (alphai(1,i)))+(Cegr(1,i-1)*alphae(1,i-1))+C4(1,i-1)-(Ru1*N3(1,i)))*...
            T1(1,i))*(1-gamma)));                                 % output equation


        Wigef(1,i)=((((V4(1,i)*((V23(1,i)/V4(1,i))^gamma))-V23(1,i))*(z(1,i)*...
            (V1(1,i)/V23(1,i))*Pin*(C3(1,i-1)+((C1(1,i-1)+(C2(1,i-1)*...
            alphai(1,i))+(Cegr(1,i-1)*alphae(1,i-1))-(Ru1*N2(1,i)))*(T1(1,i)*...
            ((V1(1,i)/V23(1,i))^(gamma-1))))-((C1(1,i-1)-C4(1,i-1))*Tref)))+...
            (Pin*((V23(1,i)*((V1(1,i)/V23(1,i))^gamma))-V1(1,i)+((1-gamma)*...
            (V1(1,i)-V4(1,i)))))*((((C2(1,i-1)*(alphai(1,i)))+(Cegr(1,i-1)*...
            alphae(1,i-1))+C4(1,i-1)-(Ru1*N3(1,i)))*T1(1,i)))))/((((C2(1,i-1)*...
            (alphai(1,i)))+(Cegr(1,i-1)*alphae(1,i-1))+C4(1,i-1)-(Ru1*N3(1,i)))*...
            T1(1,i))*(1-gamma)))/(Nf(1,i)*100*LHV);               % output equation

end;
```

Volume Pressure and Temperature Traces

```
%------------Plotting Volume trace-------------------

        angle=(1:720);
        V=(1:720);
        theta=(1:720);

        for i=1:720

          angle(1,i)=i*(pi/180);

          V(1,i)=Vc*(1+(0.5*(rc-1)*(R+1-(cos(angle(1,i)))-(((R^2)-...
              (sin(angle(1,i)))^2)^.5)))));
        end
         figure
         plot(theta,V)
         title('Cylinder Volume vs CAD')
         xlabel('CAD'); ylabel('Cylinder Volume (cm^3)')
         axis([0 720 20 600])
         grid on


 %------------Plotting Pressure trace-------------------

 P(1:228)=Pin;                          % atmospheric pressure during induction

      for i=229:round((theta23(1,cycles)-(pi/180))*(180/pi))

        P(1,i)=(Pin*(V1(1,cycles)/V(1,i))^gamma);  % pressure rise during compression

      end

  P(1,round(theta23(1,cycles)*(180/pi)))=(z(1,cycles)*((V1(1,cycles)/...
     V23(1,cycles))^gamma)*((C1+(C2*alphai(1,cycles))+(Cegr*...
     alphae(1,cycles-1))-(Ru1*N2(1,cycles)))/((((C2*(1+...
     alphai(1,cycles)))+(Cegr*alphae(1,cycles-1))-(Ru1*...
     N3(1,cycles)))*T3(1,cycles))-C3+((C1-C2)*Tref)))*...
     Pin*T3(1,cycles));                 % peak pressure after combustion (P3)


       for i=round((theta23(1,cycles)+(pi/180))*(180/pi)):476

         P(1,i)=(P3(1,cycles)*((V23(1,cycles)/V(1,i))^gamma)); % expansion pressure

       end

       for i=477:704

             P(1,i)=Pin;

       end


       P(704:720)=Pin;                  % atmospheric pressure during exhaust

           figure
           plot(theta,P)
           title('Pressure vs CAD')
           xlabel('CAD'); ylabel('Pressure (bar)')
           axis([0 720 0 62])
           grid on
```

```
%------------Plotting Temperature trace-------------------

     T=zeros(1,720);

         for i=1:228

         T(1,i)=((C1*Tin(1,cycles)+(C2*alphai(1,cycles)*X*T5(1,cycles))+...
            (Cegr*alphae(1,cycles)*Tegr))/(C1+(C2*alphai(1,cycles))+(Cegr*...
            alphae(1,cycles))));  % induction temperature dependent on previous cycle

         end


         for i=229:round((theta23(1,cycles))*(180/pi))

            T(1,i)=T1(1,cycles)*(V1(1,cycles)/V(1,i))^(gamma-1); % compression temp.

         end


         T(1,round(theta23(1,cycles)*(180/pi)))=((C3+((C1+(C2*...
             alphai(1,cycles-1))+(Cegr*alphae(1,cycles-1))-(Ru1*...
             N2(1,cycles)))*T2(1,cycles))-((C1-C2)*Tref))/...
             ((C2*(1+alphai(1,cycles-1)))+(Cegr*alphae(1,cycles-1))-...
             (Ru1*N3(1,cycles))));         % peak temperature after combustion (T3)


         for i=round((theta23(1,cycles)+(pi/180))*(180/pi)):476

          T(1,i)=T3(1,cycles)*((V23(1,cycles)/V(1,i))^(gamma-1)); % expansion temp.

         end


         for i=477:720

          T(1,i)=T4(1,cycles)*(Pin/P4(1,cycles))^((gamma-1)/gamma); % exhaust temp.

         end



        figure
        plot(theta,T)
        title('Temperature vs CAD')
        xlabel('CAD'); ylabel('Temperature (K)')
        axis([0 720 400 2300])
        grid on
```

APPENDIX B

HCCI TEST CASES

MODEL OPERATION

This tutorial provides guidance in effectively running the HCCI control model code found in Appendix A. In order to get started, the number of engine cycles must be determined and entered into the variable *cycles*. Once that is complete, the next section of the code which requires attention is that labeled Constants. This section includes a variety of parameters including fuel properties, engine geometry, EGR temperature, atmospheric pressure, specific heat values, Arrhenius Rate parameters, and heat transfer terms (X and eps). In addition to this section, there are also a few other parameters, mostly related to engine geometry, which must be entered, and which are located in lines 255-264 of the code. The current values for all of these parameters are set based on the engine geometry of the Hatz 1D50Z engine running on C_7H_{16}. Once these parameters are defined, it is now possible to begin looping the program. Since the model was developed for control using state space methods, all which is required to run the program is to specify the various input variables within the model. These input variables are intake temperature (T_{in}), external EGR fraction (alphae) and fueling rate (gpm). Random perturbations can also be added to these input variables by un-commenting the commands entitled normrnd under each input. Once these inputs have been defined, the m-file can now be run in order to obtain the various outputs from the control model. These outputs include the start of combustion (SOC), the angle of constant volume combustion (θ_{23}), the pressure rise rate (PRR), the peak pressure (P_3), the gross indicated work (W_{34}), and the efficiency (W_{igef}). The following test cases provide examples which serve to inspire confidence that the control model is indeed operating correctly. These test cases were run using the m-file entitled C7H16_NewestEdition, and consist of the inputs, outputs, state variables and pressure traces for three different engine operating conditions.

TEST CASE 1

Inputs:

- T_{in} = 463 K
- alphae = 0
- gpm = 9 g/min

Outputs:

- P_3 = 0.5731 KN/cm^2
- theta23 = 6.2297 rad
- PRR = 10.7766 bar/CAD
- W_{34} = 19.9583 KN-cm
- W_{igef} = 0.4442

State Variables:

- T_1 = 475.7303 K
- thetaSOC = 6.1795 rad
- theta23 = 6.2297 rad
- alphai = 0.0515

Pressure Trace:

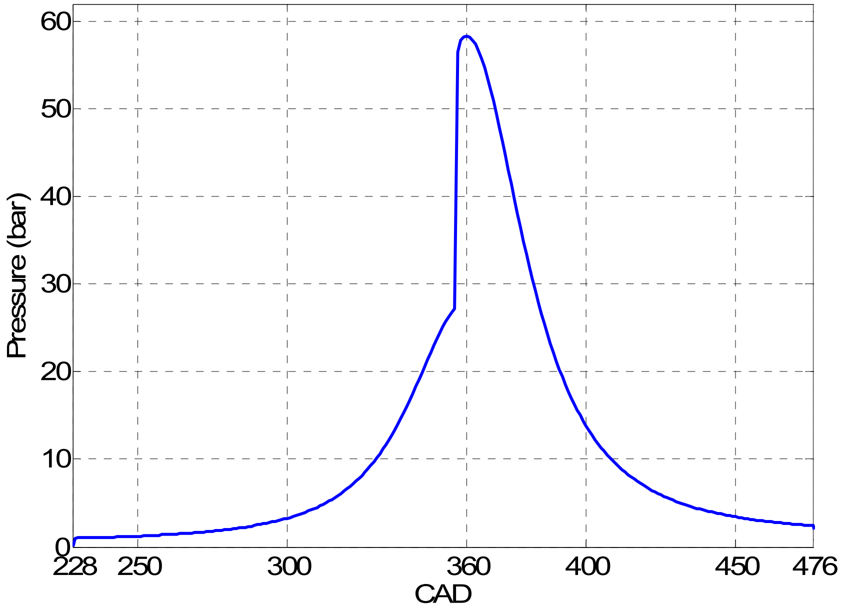

Figure A.1: Pressure trace for test case 1

TEST CASE 2

Inputs:

- T_{in} = 475 K
- alphae = 0.2
- gpm = 7 g/min

Outputs:

- P_3 = 0.3983 KN/cm^2
- theta23 = 6.5412 rad
- PRR = 0.9126 bar/CAD
- W_{34} = 15.7438 KN-cm
- W_{igef} = 0.4506

State Variables:

- T_1 = 457.6105 K
- thetaSOC = 6.3117 rad
- theta23 = 6.5412 rad
- alphai = 0.0567

Pressure Trace:

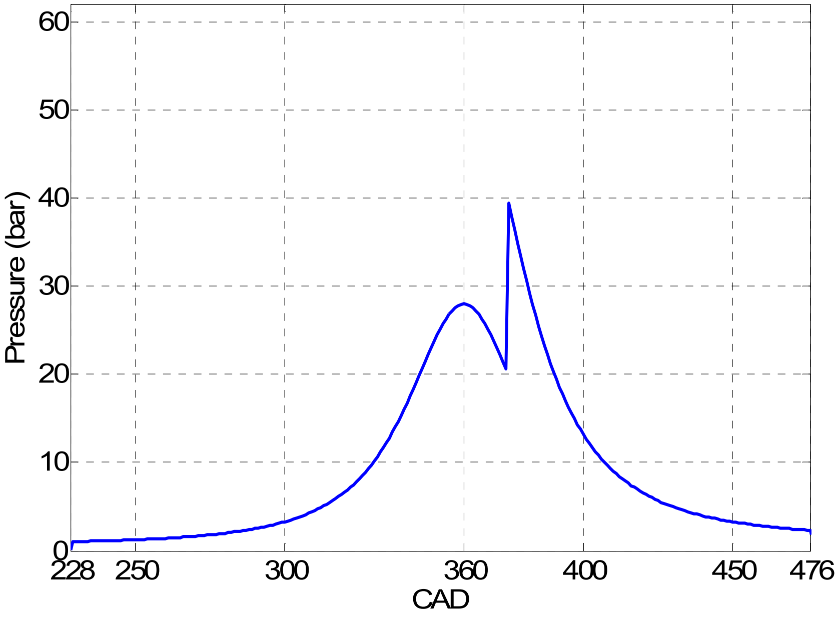

Figure A.2: Pressure trace for test case 2

TEST CASE 3

Inputs:

- T_{in} = 48395 K
- alphae = 0.05
- gpm = 5.8 g/min

Outputs:

- P_3 = 0.4735 KN/cm^2
- theta23 = 6.3179 rad
- PRR = 2.5973 bar/CAD
- W_{34} = 13.0314 KN-cm
- W_{igef} = 0.4501

State Variables:

- T_1 = 483.1816 K
- thetaSOC = 6.1758 rad
- theta23 = 6.3179 rad
- alphai = 0.0613

Pressure Trace:

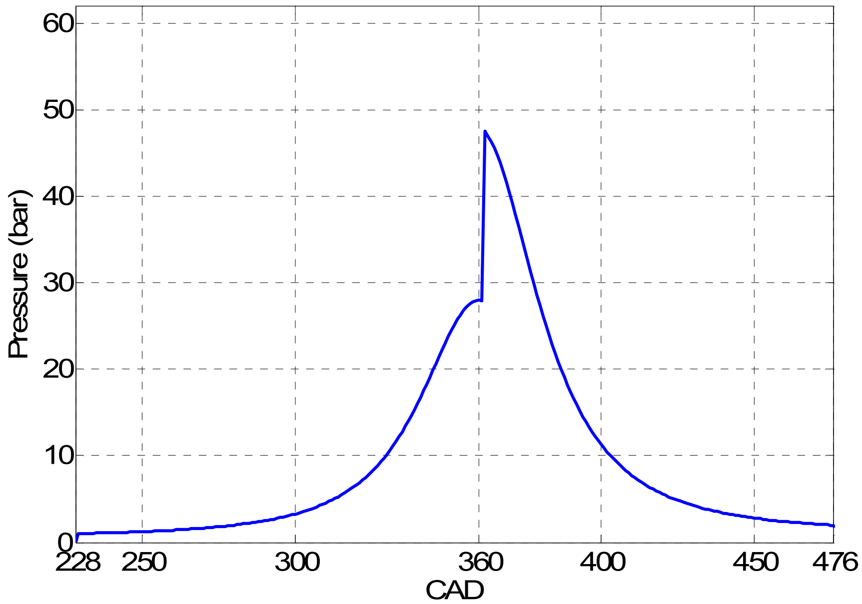

Figure A.3: Pressure trace for test case 3

BIBLIOGRAPHY

[1] Yao, Mingfa, Zhaolei Zheng, and Haifeng Liu. “Progress and recent trends in homogeneous charge compression ignition (HCCI) engines”. *Progress in Energy and Combustion Science* 35 (2009): 398-437.

[2] Stanglmaier, Rudolf, and Charles Roberts. "Homogeneous Charge Compression Ignition (HCCI): Benefits, Compromises, and Future Engine Applications." *SAE paper* 1999-01-3682.

[3] Juttu, S., S. Thipse, N. Marathe, and M. Gajendra Babu. "Homogeneous Charge Compression Ignition (HCCI): A New Concept for Near Zero NOx and Particulate Matter (PM) from Diesel Engine Combustion." *SAE paper* 2007-26-020.

[4] Shaver, Gregory, Matthew Roelle, and J. Gerdes. “Modeling cycle-to-cycle dynamics and mode transition in HCCI engine with variable valve actuation”. *Control Engineering Practice* 14 (2006): 213-222.

[5] Ghazimirsaied, Ahmad, M. Shahbakhti and Charles R. Koch. “HCCI Engine Combustion Phasing Prediction Using a Symbolic-Statistics Approach”. *Journal of Engineering for Gas Turbines and Power* 132 (2010): 1-5.

[6] Kusaka, J, T. Yamamoto, and Y. Daisho. “Simulating the homogeneous charge compression ignition process using a detailed kinetics model for n-heptane mixture”. *Int. Journal Engine Research* (2000): 281-289

[7] Yao, Mingfa, and Zhaolei Zheng. “Numerical study on the chemical reaction kinetics of n-heptane for HCCI combustion process”. *Fuel* 85 (2006): 2605-15

[8] Fiveland, SB, and DN Assanis. “Development of a two-zone HCCI combustion model accounting for boundary layer effects”. *SAE paper* 2001-01-1028

[9] Fiveland, SB, and DN Assanis. “Development and validation of quasi-dimensional model for HCCI engine performance and emissions studies under turbocharged conditions”. *SAE paper* 2001-01-1757

[10] Xu, HM, A Williams, HY Fu, S Wallace, S Richardson, and M Richardson. “Operating characteristics of a homogeneous charge compression ignition engine with cam profile switching-simulation study”. *SAE paper* 2003-01-1859

[11] Ogink, R. “Applications and results of a user-defined, detailed chemistry HCCI combustion model in the AVL BOOST cycle simulation code”. *International AVL User Meeting* (2003): 14-15

[12] Aceves SM, DL Flowers, CK Westbrook, JR Smith, WJ Pitz, RW Dibble et al. “A multi-zone model for prediction of HCCI combustion and emissions”. *SAE paper* 2000-01-0327

[13]Shaver, G, M. Roelle, P. Caton, N. Kaahaaina, N. Ravi, J. Hathout et al. “A physics-based approach to the control of homogeneous charge compression ignition engines with variable valve actuation”. *Int. Journal Engine Research* (2005): 361-375

[14]Waero, Rolf R. "The Effect of Spark Timing on Residual Gas Fraction." Thesis. University of Michigan, Ann Arbor, 1997.

[15]Massey, Jeffrey, James Drallmeier, Scott Eaton, and Robert Wagner. “Influence of the Combustion Energy Release on Surface Accelerations of an HCCI Engine”. *SAE Paper* 2009-01-2741

[16]Vance, J., P. He, B. Kaul, S. Jagannathan, and J. Drallmeier, “Neural network-based output feedback controller for lean operation of spark ignition engines” *Proc. of the Amer. Controls Conf.* (2006): 1898-1905.

[17]Iida, M, M. Hayashi, D.E. Foster, and J.K. Martin. “Characteristics of Homogeneous Charge Compression Ignition (HCCI) Engine Operation for Variations in Compression Ratio, Speed, and Intake Temperature While Using n-Butane as a Fuel”. *Journal of Eng. For Gas Turbines and Power* (2003): 472-478

[18]Heywood, J.B. “Internal Combustion Engine Fundamentals”. McGraw-Hill, 1988.

[19]Fox, Jonathan W., Wai K. Cheng and John B. Heywood. “A Model for Predicting Residual Gas Fraction in Spark-Ignition Engines.” *SAE Paper* 931025

[20] Shahbakhti, Mahdi, and Charles Robert Koch. “Physics Based Control Oriented Model for HCCI Combustion Timing.” *Journal of Dynamic Systems, Measurement and Control* 132 (2010): 1-12

[21] Rausen, DJ, A.G. Stefanopoulou, JM Kang, JA Eng and TW Kuo. “A Mean-Value Model for Control of Homogeneous Charge Compression Ignition (HCCI) Engines”. *Proc. of the 2004 American Control Conference* (2004): 125-131.

[22] Shahbakhti, Mahdi, and Charles Robert Koch. “Control Oriented Modeling of Combustion Phasing for an HCCI Engine”. *Proc. of the 2007 American Control Conference* (2007): 3694-3699.

[23] Ravi, Nikhil, Matthew Roelle, Adam Jungkunz and Christian Gerdes. “A Physically Based Two-State Model for Controlling Exhaust Recompresion HCCI In Gasoline Engines”. *Proc. of International Mechanical Enginering Conference and Exposition* (2006): 1-10.

[24] Chiang, Chia-Jiu, Anna Stefanopoulou and M. Jankovic. “Nonlinear Observer-Based Control of Load Transitions in Homogeneous Charge Compression Ignition Engines”. *IEEE Transactions on Control Systems Technology* 15.3 (2007): 438-448.

[25] Chiang, Chia-Jiu, and Anna Stefanopoulou. "Stability Analysis in Homogeneous Charge Compression Ignition (HCCI) Engines With High Dilution". *IEEE Transactions on Control Systems Technology* 15.2 (2007): 209-218.

[26]Swan, Kevin, Mahdi Shahbakhti, and Charles Koch. "Predicting Start of Combustion Using a Modified Knock Integral Method for an HCCI Engine". *SAE paper* 2006-01-1086.

[27]Ogink, R. "Approximation of Detailed-Chemistry Modeling by a Simplified HCCI Combustion Model". *SAE paper* 2005-24-037.

[28] He, X., M. Donovan, B. Zigler, T. Palmer, S. Walton, M. Wooldridge, and A. Atreya. "An experimental and modeling study of iso-octane ignition delay times under homogeneous charge compresion ignition conditions." *Combustion and Flame* 142 (2005): 266-275.

[29] Babajimopoulos, Aristotelis, George Lavoie and Dennis Assanis. "On the Role of Top Dead Center Conditions in the Combustion Phasing of Homogeneous Charge Compression Ignition Engines". *Combust. Science and Tech.* 179 (2007): 2039-2063.

[30] Livengood, J., and P. Wu. "Correlation of Autoignition Phenomena in Internal Combustion Engines and Rapid Compression Machines". *Fifth Int. Symposium on Combustion* (1955): 347-356

[31]Turns, S.R.. "An Introduction to Combustion: Concepts and Applications." McGraw-Hill, 2nd edition, 2000.

[32]Chiang, C., and A. Stefanopoulou. "Sensitivity Analysis of Combustion Timing and Duration time of homogeneous Charge Compression Ignition (HCCI) Engines." *Proc. of the Amer. Controls Conf.* (2006): 1857-62.

[33]Yang, Q., J. Vance, and S. Jagannathan, "Neural network control of non-affine nonlinear discrete-time systems", *IEEE Transactions on Systems, Man and Cybernetics: Part B* 38 (2008): 994-1001.

[34]Risberg, Per, Guatam Kalghatgi, and Hans-Erik Angstrom. "Auto-ignition Quality of Gasoline-Like Fuels in HCCI Engines." *SAE paper* 2003-01-3215.

[35]Kalghatgi, Guatam. "Auto-Ignition Quality of Practical Fuels and Implications for Fuel Requirements of Future SI and HCCI Engines." *SAE paper* 2005-01-0239.

[36]Kalghatgi, Guatam, Per Risberg, and Hans-Erik Angstrom. "A Method of Defining Ignition Quality of Fuels in HCCI Engines." *SAE paper* 2003-01-1816.

[37]Kalghatgi, Guatam, and R.A. Head. "The Available and Required Autoignition Quality of Gasoline-Like Fuels in HCCI Engines at High Temperatures." *SAE paper* 2004-01-1969.

VITA

Joshua Bradley Bettis was born in St. Louis, Missouri on May 13, 1985. He graduated from Hillsboro High School in May of 2003. He did a summer internship with the 3M Corporation during the summer of 2006 in Nevada, MO. In the spring of 2007, he worked for Hunter Engineering Company in Bridgeton, MO as an engineering co-op. In May 2008, he received his B.S. with Honors in Mechanical Engineering from the University of Missouri-Rolla. During the summer of 2008, he worked for Caterpillar in Aurora, IL as a summer intern. In December 2010, he received his M.S. degree in Mechanical Engineering from the Missouri University of Science and Technology (formerly known as University of Missouri-Rolla).